NORTHWESTERN UNIVERSITY

Bulk and Interfacial Fatigue Behavior of Polymer Networks

A DISSERTATION

SUBMITTED TO THE GRADUATE SCHOOL

IN PARTIAL FULFILLMENT OF THE REQUIREMENTS

for the degree

Doctor of Philosophy

Field of Materials Science and Engineering

By

Qihua Chen

Evanston, IL

September 2023

Bulk and Interfacial Fatigue Behavior of Polymer Networks

Qihua Chen

Polymers occupied nearly every facet of our daily lives, and enhancing their mechanical and fracture properties has long been an important topic in the field of polymer science. Based on the various need in applications, polymers are designed to have a range of characteristics such as tackiness, optical properties, mechanical strength, rheological properties, chemical resistance and thermal conductivities. To achieve the diverse properties, they are modified by methods such as the addition of fillers, blending and varying the crosslinking conditions.

While there are a lot of strategies to physically or chemically modify the matrix structures of the polymers, not so many systematic fatigue characterization methods can be easily applied onto different polymer products designed for different industrial purposes. To address this problem, this thesis focuses on developing straightforward and cost-effective methodologies to tackle the challenges in understanding the long-term fatigue failure mechanisms of polymer networks, providing insights to both bulk and interfacial contributions during fatigue fracture process. These insights and interpretations are critical for industrial products, which are always expected to be durable and contribute to sustainability. Given the varieties in polymer matrix, three representative polymer model systems are chosen to cover the extensive scale of mechanical stiffness: lightly crosslinked pressure sensitive adhesives (PSA), filled rubber elastomers and filler-reinforced epoxy matrices. The fatigue characterization of each polymer matrix requires unique methods that consider both the bulk and interfacial contributions, which involves utilizing various testing geometries, such as indentation, flexural, and pure shear tensile geometries.

This thesis initiates with an investigation into the fatigue resistance of silicone and natural rubbers under elevated temperature conditions, employing a pure shear tensile geometry. Subsequently, the morphologies of the crack surfaces are analyzed and discussed in relation to the conditions of energy dissipation during the fatigue tests. The fatigue characterization method involves subjecting the sample to cyclic oscillation for stress-strain hysteresis loops, which allows for the extraction of mechanical response information and the calculation of energy dissipation across different length scales. Part of the energy is dissipated in the bulk material and the remaining stored elastic energy, recovered from the unloading curve, serves as the driving force for crack propagation. Similar to rubber elastomers, the softer PSA were examined with pure shear cyclic tests and probe tack tests utilizing an indentation setup. In this scenario, the stored elastic energy is the driving force for the detachment between the indenter and the adhesive surface. For the investigation of the rigid epoxy matrix, a flexural fatigue crack propagation test was designed to study a triblock copolymer-filled dynamic epoxy matrix. This approach also demonstrated a good correlation with the Dugdale model, particularly in the context of a standard flexural three-point bending fracture toughness test.

Acknowledgments

When I first stepped onto the campus of Northwestern University in summer 2018, I was alone and knew nobody. Five years later, I am graduating as I (and my I-20) anticipated, but it was unforeseen and pleasantly surprising to receive so much assistance, guidance, and support from so many people. I would like to express my appreciation and acknowledge these people, as I would not have been able to complete this thesis without them.

To my advisor, **Dr. Ken Shull**, thank you for your guidance, kindness and patience which constantly leads me along the way. It is very lucky of me to meet an advisor like you, who will sit down and spend an afternoon to look through the basic coding problems, who will always be at my back and support me when I encounter obstacles during my graduate school study, and who cultivates a dynamic, warm and supportive group environment, building a sense of cooperation and shared support among us. You always encourage me to venture out and try new ideas that come to my mind and to explore industrial career choices. Your guidance will continue to influence me for the rest of my life. I would also like to thank your family for arranging heartwarming holiday parties and preparing gifts for each of us.

To my committee members, **Dr. Wesley Burghardt**, **Dr. Wei Chen**, and **Dr. Jeffrey Richards**, thank you all for being my thesis committee members. Your expertise, insights, comments and suggestions are instrumental and invaluable to me. Prof. Burghardt, your rheology class is one of the most helpful classes that I have taken, setting a solid foundation for me in polymer physics. Prof. Chen, I had a great time collaborating with your research group. Prof. Richards, thank you for being a committee member and provide thoughtful discussions for both my qualifying exam and thesis defense.

To my Shull group friends, I am grateful to meet you all. **Dr. Qifeng Wang**, our lab cannot operate without you. You are one of the most knowledgeable people I know and it is always enlightening to discuss research ideas with you. To **Gwen dePolo** and **Anthony Silvaroli**, thank you for always being there throughout the PhD journey. I will miss the homework nights and the joyful time we spent together in the office. Thanks for clarifying the difference between a savory pie and a pizza for me. Gwen, thanks for taking care of Nina when I am away, and I hope you and Sam enjoy your time in DC. Anthony, it was such a coincidence that I met you on the first day of Wildcard registration, long before we chose the Shull group. I hope you and Gretchen have a great time in Midland. To **YuLing Chen**, we used to do morning workouts and restaurant hunting trips, and I wish we can do more of that in the future. You are always energetic and best of luck as you near the completion of your degree. To **Broderick Lewis**, you are diligent and intelligent, and I can always learn a lot when working with you. Good luck with the rest of your PhD program. To **Ben Hafner**, I am always impressed by how quick you learn. I hope you enjoy doing research in the Shull group and wish you a bright future. To **Chenyuan Dong**, **Sheng Wang** and **Jazmyn Lu**, I wish you all the best in your future endeavors.

To former Shull group members, **Dr. Joshua Yeh**, **Dr. Yaoyao Chen**, **Dr. Kazi Sadman**, **Dr. Shawn Chen**, **Dr. Matthew Eaton**, **Dr. David Delgado** and **Dr. Thomas Schmitt**, it has been an absolute delight to learn from you and occasionally catch up with you at conferences. Special thanks to Yaoyao, who has taught me a great deal, not only about academics, but also in terms of career advice.

Thank you to my mentors and everyone I worked with during my internship at 3M. To **Dr. Chris Campbell**, thank you for offering me this great opportunity to work as an intern at 3M. To **Dr. Evan Breedlove**, I appreciate your advice and your help during my internship. Looking forward to work with you in the near future. To my manager, **Dr. Thomas Clausen**, thank you for trusting in my competence at work and for accepting me into this position. I'm deeply thankful for the opportunity to work with everyone at the **AMX lab**, and I appreciate all the help you've provided.

To my collaborators at Northwestern: **Tyler Hyel**, **Dr. Umar Ghumman**, **Ziwei Wang**, and **Dr. Jie Chen**, I am grateful for your scientific insights, without which this thesis would not have been possible.

I would like to acknowledge my friends I have made in the SPIE NU Chapter: **Yuanwei Li**, **Wenjie Zhou**, **Daniel Timbie**, **Nia Burrell**, **John Misiaszek**, **Julian Gamboa**, **Emma-rose Newmeyer**, **Samaneh Ansari**, and **Whitney Tso**, I have had a great time arranging events with you. To my friend in my cohort, **Chia-Pao Lee**, thank you for always being friendly and helpful, and I wish you the best of luck in your pursuit of the PhD degree.

To all the dearest friends I have met during my PhD, we have created precious memories over the past five years. I would like to acknowledge my friends, including but not limited to: **Shuang Liang**, **Yining Liu**, **Yuqin Wang**, **Jiahong Shen**, **Jianan Shen**, **Huanbo Jiang**, **Dingwen Qian**, **Yao Tong**, **Chier Zhang** (and you, YuLing). I cherish every moment when we hang out as a group. We've shared unforgettable experiences, from camping and skiing trips to a memorable summer at a lakeside house in Minnesota in 2021. We have explored remarkable and not-so-remarkable restaurants. We have played Mahjong till midnight. We always had so much fun playing board games and video games together. In addition, thanks to the friends that I knew through my partner: **Guo Ye**, **Qiankai Cao**, **Zihao Wang**, **Mingfu Liang**, **Zhihan Zhou**, **Liqian Ma**, **Jian Wei**. Thanks for all the dinner nights and hot pot nights you've arranged. Spending time with you is always a blast. To all my friends, may you have all the luck and success in your future lives.

To my friends in China, I always treasure our enduring friendships, even though you are on the other end of the world. To **Jie Yu**, It is hard to believe that we have known each other for almost 15 years, and we still contact each other every day. Thank you for the jokes, interesting memes and sharing the bits and pieces of your life with me all the time. I have witnessed your journey of growth from a school girl into an artist and designer. I am very proud of you and I hope our friendship lasts forever. To **Zhanghui Qian**, you were my best friend in high school. Thanks for taking time to hang out with me every time I am back to China, even when you are busy with work.

I take great joy in celebrating your life's advancements, but all I want is you to be happy. Good luck with your bar exam!

To my amazing partner, **Qinjie Lin**, meeting you has been the luckiest thing that has ever happened to me. Thank you for all the patience, love and support over the past several years. When I feel down, you always find different ways to cheer me up, including cooking delicious meals for me. We've shared numerous experiences, and you've been there for every big decision in my life. Thank you for keeping my life on track, and I can't wait to see what future this track leads to. To my beloved furry friend, **Nina**, you are a great cat. It is a great honor to be your most trusted human and I appreciate your constant companionship.

To my parents, **Qin Zhang** and **Dong Chen**, thank you for your unconditional love and support to raise me up and send me abroad for advanced education. I know it was a difficult decision to send me, your only daughter, to a distant land far away from home, but I will do my best not to let you down. I hope to come back to China to see you more often in the future. To my late cat **Mimi**, I think of you every day and miss you deeply.

To my Grandpa **Shuliang Zhang**, I wish you could see me graduate.

Contents

List of Tables

List of Figures

Chapter 1

Introduction

1.1 Overview

Gaining insights into the long-term failure mechanism of polymer networks is essential for a wide array of applications, as polymers display a broad range of properties. At one end of the spectrum, we have soft, gel-like pressure sensitive adhesives with an elastic modulus of less than a hundred kPa, and at the other end, we utilize epoxies with stiff crosslinkers that yield a modulus of several GPa. The diverse applications for polymer materials covers nearly all aspects of our life, including tires, seals, bonding agents, coatings, body implants and electronic devices. Almost all of these applications necessitate materials that exhibit longevity, thereby increasing the service life and promoting sustainability by reducing plastic production.

To evaluate the mechanical durability of these materials, researchers utilize various mechanical tests to resemble real-life application, such as tensile, compression, flexural, compact tension, indentation, double cantilever beam, and peel tests [1–5]. However, accurately quantifying polymer fatigue behaviors remains challenging. Degradation in materials takes year to manifest and may occur under complex environmental conditions, such as fluctuations in temperature, humidity and UV exposure [6, 7]. As a result, researchers must adopt various methods and adjust the strategies when studying fatigue mechanisms in a limited timeframe. Moreover, the geometries of materials in practical applications can influence their performances. For instance, ultra-soft PSAs used in foldable devices undergo internal cavitation and interfacial debonding, which are phenomena that cannot be effectively studied using conventional fatigue measurement techniques [8–10]. In light of these complexities, it is crucial to design tailored methodologies that meet the diverse requirements of mechanical properties evaluations of polymers. This thesis concentrates on examining the nonlinear viscoelastic fracture mechanics and fatigue failure mechanisms of polymer materials across various stiffness scales.

1.2 Research Objectives

The goal of this research is to develop suitable methodologies for quantitatively understanding the material fracture and fatigue mechanisms across a extended spectrum of materials, ranging from lightly crosslinked, gel-like adhesives to rigid, glass-like epoxies. Fatigue behavior characterization can be carried out using different testing schemes tailored to different materials, including pure shear tensile tests, axisymmetric probe tack tests, and flexural 3-point bending tests. The design of fatigue tests focus on the comparison between linear viscoelastic regime and large strain behavior since most applications require materials to withstand under a large strain condition. The analysis of material fatigue behavior concentrate on energy dissipation discussions based on linear elastic fracture mechanics (LEFM) and cohesive zone model.

This thesis is structured into four main chapters corresponding to four projects investigated. Chapter 2 offers a brief background introduction of the fundamental fracture mechanics theories, including the classic LEFM theory, Griffith's energy dissipation criteria, and an overview of mechanical tests utilized in this thesis. These theoretical concepts serve as the physical foundation for discussions on solid mechanics and rheology within the context of the model systems explored in later chapters.

Chapter 3 presents a thorough study of fatigue crack propagation behavior of silicone rubber under elevated temperatures. Nature rubber is used for comparing large strain crack growth behavior with silicone rubber. Energy dissipation is quantified using an effective viscoelastic phase angle representation, and is observed to decrease with the increase of temperature in silicone rubber. This change in energy dissipation also leads to a change in crack interfacial surface patterns, as observed under a 3D microscope.

Chapter 4 closely follows the microscopic observation from Chapter 3 and explores possible approaches to comprehend the fracture surfaces. In this chapter, several image processing techniques are applied, including surface area integration, power spectral density function analysis and machine learning through transfer learning.

Chapter 5 investigates the fatigue response of pressure-sensitive adhesive (PSAs) in both bulk and at the interface. Due to the low modulus and high extensibility of PSAs, traditional fatigue crack propagation test in pure shear geometry cannot be applied as severe crack tip blunting prevents further propagation. Consequently, unnotched fatigue damage test and probe tack test were employed to evaluate the decline in fatigue properties of PSAs.

Chapter 6 studies the fatigue and fracture properties of a triblock copolymer-filled dynamic epoxy-amine network. This project presents the use of flexural 3-point bending geometry to investigate both fracture toughness and flexural fatigue, demonstrating that the triblock copolymers significantly improve both the fracture toughness and fatigue resistance of the epoxy matrix.

Chapter 7 provides a summary of the key findings and developed techniques and highlights potential future research directions.

Chapter 8 serves as the appendix, which includes the supplementary informations for the chapters above.

Chapter 2

Background

2.1 Linear Elastic Fracture Mechanics (LEFM)

The fracture behavior of highly stiff and brittle materials is typically characterized by Linear Elastic Fracture Mechanics (LEFM), a fundamental fracture mechanics theory that assumes the bulk material exhibits linear elasticity everywhere, except in the region near the crack tip. In 1921, A. A. Griffith [11] established the crack propagation theory, arguing that the creation of a new crack surfaces is driven by the strain energy density $\mathscr{G} = \Gamma$, which is equal to the mechanical energy required to create new fracture surface per unit area. Based on this argument, a length scale of the crack tip radius at propagation ρ^* can be defined, which directly relates to an important length scale ℓ:

$$\rho^* \sim \frac{\Gamma}{E} = \ell \tag{2.1}$$

At this length scale ℓ, the energetic cost of creating new surfaces is comparable to the elastic modulus of the material [1, 12]. Based on Griffith's work, G. R. Irwin suggested a plastic zone ahead of the crack tip in ductile materials and introduced the concept of stress intensity factor[13] in 1950. In a linear elastic solid, the critical energy required for fracture is characterized by the critical stress intensity factor, also known as fracture toughness. However, due to the limitation of LEFM in dealing only with brittle materials exhibiting small-scale yielding, modified LEFM theories, such as the J-integral or the cohesive zone theory, are needed for nonlinear fracture mechanics for more ductile materials.

2.2 Cohesive Zone Model

The arguments of LEFM do not readily extend to soft materials, as soft materials do not fracture in the same way brittle materials do when the far-field stress surpasses the elastic modulus. Contrary to brittle materials where the crack tip remains sharp during propagation, soft materials tend to form a rounded crack tip and an extended plastic deformation zone. This observation led to the introduction of cohesive zone model to accommodate this situation and to quantify the rate-dependent effect in the materials[12, 14]. The theory of LEFM was consequently modified to include length scale ℓ, a blunted zone at the crack tip that is highly strained, where the cost of creating new surfaces is comparable to the elastic modulus of the material [1, 12, 15]. For example, the Dugdale model proposes a plastic zone, denoted as r_p, which is subjected to a uniform cohesive stress. Within this zone, the material at the crack tip experiences plastic deformation and eventually leads to fracture when the stress reaches to the yield stress.

Since LEFM is not applicable near the crack tip at a length scale ℓ, the region below which is considered as existing in a nonlinear regime. This highly stretched crack tip region has been studied by many groups of researchers, such as Hui *et al.* who first proposed the cohesive zone model and qualitatively considered the possible mechanisms during crack growth [15]. Many subsequent have expanded on this foundation and further considered additional fracture mechanisms and the influence of strain hardening. For instance, Seitz *et al.* studied the fracture of acrylic triblock copolymer gels and captured the strain hardening effect along with its surrounding field through compression tests and finite element modeling (FEM) [16]. Mzabi *et al.* worked on the fatigue response of styrene-butadiene rubber and observed the deformation field near the crack tip using Digital Image Correlation (DIC) [17]. While those approaches to understand the cohesive zone beyond LEFM advances our understanding of fracture mechanics in soft materials, the whole picture is still hard to account for the complex, non-linear viscoelastic behavior of all polymer materials. Due to their inherent molecular-level property variations, polymer exhibit unique thermodynamic behaviors and could show distinct large strain viscoelastic properties which cannot be explained easily. In the presence of large strains applied to the soft matter, the fracture mechanics usually require to be analyzed separately at different length scales.

Consideration of fracture mechanics across varying length scales naturally prompts us to question the condition of energy dissipation during the fracturing process. Although the comprehensive mechanism of damage and viscoelastic dissipation remain not yet fully understood, certain hypotheses have been made by Creton and Ciccotti [1] to separate energy dissipation scales spatially. Three different scales of dissipation are defined, which are the load-related zone (energy dissipation in bulk material due to the far-field loading condition), crack related dissipation zone (energy dissipation related to the crack propagation, with a radius R) and local damage zone (a small zone close to the crack tip related to the molecular bond breakage, radius R_0). Under this conceptual framework, considerations need to be made regarding the length scale of the strain and dissipation. When strain and energy dissipation occur at a larger scale ($R \sim \rho^*$), the energy transfer cannot be satisfactorily explained by LEFM alone, and alternative methods of analysis should be involved.

2.3 Bulk and Interfacial Test

In industry, the long-term durability of polymers for many applications needs to be addressed, which facilitates improvements and modifications during the product development process. As such, studying fracture mechanics through different mechanical analysis becomes an effective and economical approach to achieve this goal. This section provides the background introduction to the bulk and interfacial tests employed throughout this thesis.

2.3.1 Unnotched Fatigue Damage Test

Typically, fatigue tests are conducted on samples that are either notched or unnotched. The unnotched fatigue damage test, also called the crack nucleation approach, emphasizes on the number of cycles needed to generate a certain-sized crack, thereby allowing for the determination of the fatigue crack nucleation life. This method is widely used in situations where the initial flaws are significantly smaller than the component features, but will finally determine the component's lifespan [18]. For glassy polymers and metal alloys, similar ideas are adopted as the stress-life (S-N) approach where the maximum cyclic stress (S) is plotted as a function of the cycles needed for fracture (N) to predict the fatigue life. Such characterization method can also be applied to softer materials such as elastomers and gels. In these cases, the tests mainly focus on tracking the degradation of various properties, including modulus, toughness, hysteresis loop, etc[2, 19].

2.3.2 Fatigue Crack Propagation Test

The crack propagation approach focuses on the existing cracks and is the major method of investigation in this work. Based on the crack theory of Griffith [11], Thomas and coworkers [20–23] extended the discussion of energy balance in fracture to analyze rubber fatigue under cyclic loads. The stored mechanical energy per unit creation of the new crack surface area, which reflects the loading condition of the sample, is called the energy release rate $\mathscr{G}$ and depends on the strain history of a sample in a pure-shear geometry:

$$\mathscr{G} = h_0 \int_0^{\varepsilon_1} \sigma_N d\varepsilon_N \tag{2.2}$$

Here, σ_N and ε_N are the stress and strain, respectively and h_0 represents the sample height. The crack length is determined from the mechanical stiffness of the sample, as described in more detail

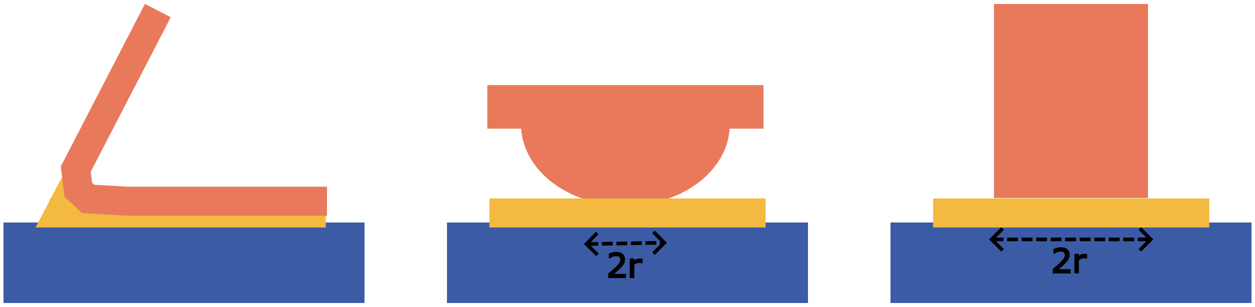

Figure 2.1: Geometries of common adhesive test. Left: Peel test; Middle: Spherical probe test; Right: Flat punch probe test.

in later chapters. The relation of fatigue crack growth rate and the energy release rate was mainly identified by Lake and Lindley [24] and was categorized into four regimes, from which the third regime described a logarithmic relation between the two variables:

$$\frac{da}{dN} \propto \mathscr{G}^{\alpha} \tag{2.3}$$

This logarithmic relation is also an adjusted model of the Paris law. In this equation, da/dN is the crack growth rate per cycle and α is the power-law index, which varies between different materials.

2.3.3 Adhesion Test

For softer materials such as adhesives or gels, different research approaches can be adopted to study both the bulk and the interfacial properties. In addition to the characterization of bulk properties through fatigue tests, repeated adhesion tests can also be used as tools to probe contact mechanics of adhesive materials. Common adhesive tests include peel test [25, 26] and indentation using spherical or flat punch indenter[8, 27–31]. The schematics of the adhesive tests are shown in Figure 2.1.

By indenting a tip into the material and controlling the load/displacement condition, the stress and strain responses can be obtained so that information such as elastic moduli, hardness, and stress relaxation profile can be extracted. The compliance C of the sample is the ratio of the displacement δ to the load response P. For a rigid, frictionless indenter (radius r) [30, 32]:

$$C = C_0 = \frac{\delta}{P} = \frac{1}{2rE^*} \tag{2.4}$$

Assuming incompressible samples, the Poisson's ratio $v = 0.5$. Therefore the effective elastic modulus E^* can be modified by the Poisson's ratio assuming plane strain condition:

$$E^* = \frac{E}{1 - v^2} \tag{2.5}$$

Oscillatory indentation provides a way to characterize the oscillatory response of the material using an indenter. An indentation experiment holds the advantage in that it allows more flexible and abundant modifications to the sample environment, such as mechanical tests in a solvent, which can hardly be accomplished by using mode I tests in pure shear geometry. In this work, oscillatory indentation has been applied to PSA samples to analyze their bulk and interfacial viscoelastic properties.

Chapter 3

Temperature-Dependent Viscoelastic Energy Dissipation and Fatigue Crack Growth in Filled Silicone Elastomers

There has always been a need to investigate the mechanical properties and fracture behaviors of materials that are widely used commercially, such as filled silicone rubbers. In this work, a thorough study was performed to evaluate the temperature dependencies of viscoelastic energy dissipation and fatigue crack propagation. Small strain viscoelastic behavior was examined by using dynamic mechanical analysis (DMA) and larger strain viscoelastic dissipation was quantified by defining an effective viscoelastic phase angle from large amplitude cyclic deformation. Pure shear mode I fatigue tests were performed for quantification of material toughness and crack propagation resistance. In addition, natural rubber with different filler levels was tested to provide a direct comparison between two important classes of filled rubber elastomers. Major differences were identified for the two elastomers. However, for both types of elastomers, a common power law relationship with an exponent of 1.5 describes the dependence of the fatigue crack growth per cycle on a normalized driving force obtained from the stored elastic energy. We found that the silicone rubber deviated from the 1.5 exponent power law relation at elevated temperature, and its prefactor in this power law was correlated to the crack morphology, with rough cracks providing a higher fatigue resistance than smooth cracks.

Material in this chapter is reproduced and published in “Temperature-Dependent Viscoelastic Energy Dissipation and Fatigue Crack Growth in Filled Silicone Elastomers” authored by Qihua Chen, Shixian Xu, Ming Lu, Jia Liu, and Kenneth R. Shull, ACS Applied Polymer Materials 3.12 (2021): 6207-6217[33]. This research utilized equipment in the Materials Characterization and Imaging Facility (MatCI) at Northwestern University, which is partially supported by the NSF MRSEC program (NSF DMR-1720139). DMA data, TGA data and additional fracture surface images are included in the Appendix A.

3.1 Introduction and Background

Elastomeric materials are commonly used in applications where the use life is determined by the fatigue crack growth under cyclic loading conditions[7]. Understanding the effects of the composition of elastomers and their fatigue response at elevated temperatures are particularly important, as investigated, by Lake *et al.*[23], Young *et al.*[34], Mars *et al.*[35] and Demassieux *et al.*[36]. Silicone rubber has major benefits arising from the Si-O bonds in the backbone of the polymer, which are partially attributed to the higher bond energy for Si-O bonds ($\approx$ 440 kJ/mol) [6] in comparison to a value of C-C bonds ($\approx$350 kJ/mol). Silicone products are used in many fields, such as aerospace, cookware, molding, and medical devices. For such applications, elastomers will experience higher temperature under repetitive usage, and these applications require steady and predictable mechanical properties of silicone rubber, especially when related to food and medical safety. An ability to understand the role of energy dissipation in those elastomers and predict their fatigue performance is critically essential in these situations.

Characterization of the fracture strength of filled silicone elastomers is not so extensive. Yeh *et al.* quantitatively considered fracture and thermal aging of resin-filled silicone elastomers [37]. Other research teams investigated fatigue fracture and viscoelasticity of silicone rubber [38–40], but the fatigue endurance data remains limited. Moreover, there is a restricted number of studies[17, 41, 42] about the contribution of energy dissipation to crack propagation in silicone elastomers. Given the fact that fatigue experiments are time consuming, it is highly desirable to develop a more quantitative understanding of the material properties that correlate with fatigue crack growth in silicone elastomers. The focus of the work described here is on the development of these types of property correlations.

In this work, silicone rubber with a specific composition wass tested under a range of temperatures, and 8 additional samples varying filler and crosslinker levels were tested at room temperature to illustrate the effects of composition on the fatigue response. This study aims to characterize the energy dissipation within silicone rubber during fatigue crack propagation under cyclic loading conditions, and to develop a meaningful criterion for quantifying the rate of crack propagation. This criterion is based on a separation of total energy input into dissipated and elastically stored components. We compare the results of silicone rubber with those from 6 natural rubber samples with varying filler levels. The fracture behavior of natural rubber has been more thoroughly described in the literature than the fracture behavior of silicone rubber. For example, the early work by Rivlin and Thomas on the tear strength of natural rubber is now more than 65 years old [20]. A theme in much of the subsequent work has been to relate fracture properties of natural rubber to composition and structural changes in the material[21–24, 36, 43–51]. In the current study we illustrate the properties of silicone rubber by providing a direct comparison between these two classes of materials.

3.2 Methods and Materials

3.2.1 Materials

Silicone rubber and natural rubber were tested as received from Beijing Institute of Aeronautical Materials (BIAM). Additional components were added to both materials. For silicone rubber, the components include Aerosil 380 silica (Degussa, Germany), 120-1 Phenyl silicone rubber (Shanghai resin factory, China), Cr_2O_3 (Tianjin Fengchuan Chemical Reagent Technologies, China), GY-209 hydroxyl-ended polysiloxane (Zhonghao Chenguang Research Institute of Chemical Industry, China) and Bis(*tert*-butyldioxyisopropyl)benzene (BIPB) (Shanghai Farida Chemical Co., China). The components of the natural rubber samples include natural rubber (China Hainan Rubber Industry Group Co., China), Zinc Oxide (Cangzhou Jiewei Zinc Industry Co., China), stearic acid (Hebei Richangsheng Chemical Co., China), carbon black (N330, Longxing Chemical Stock Co., China), *N-tert*-Butyl-2-benzothiazolesulfenamide (Willing New Materials Technology Co., China) and sulfur (Zibo Heye Chemical Co., China). Detailed compositions are shown in Table 3.1.

A range of crosslinking densities and filler contents were utilized for the silicone rubber samples. For natural rubber, different filler contents were considered yet the crosslinking density was not varied. The naming of the samples follows the rule that 'SR' represents silicone rubber, 'NR' represents natural rubber, 'Fxx' stands for the amount of filler added (Silica for SR and Carbon Black for NR), and 'Cxx' stands for the different amount of crosslinker added (Peroxide for SR, not shown for NR). The unit is parts per hundred rubber (phr). The components were mixed on a two-roll miller at room temperature. The compounds were press-molded into a 1 mm-thick plate at 170°C for 10 minutes, and post-cured in an air-circulated oven at 100°C for 2 hours. Among the different silicone rubber and natural rubber samples with different filler and crosslinker levels, only SR-F37-C0.8 and NR-F30 were selected for temperature-dependent fatigue tests.

3.2.2 Mechanical tests

3.2.2.1 Thermogravimetric Analysis (TGA)

TGA was used to investigate the degradation behavior of the elastomers at very high temperatures. Using the method in supporting information, the activation energy of degradation was obtained by defining a point of equivalent weight loss (15%) at different heating rates. The respective activation energies for SR and NR in air are $E_{a,TGA}^{SR} = 114$ kJ/mol and $E_{a,TGA}^{NR} = 396$ kJ/mol.

Table 3.1: Compositions of the silicone and natural rubber formulations. All components are given in parts per hundred rubber (phr). SR, Cr_2O_3 and PSiO-OH are silicone rubber, Chromium (III) oxide, and hydroxyl-ended polysiloxane, respectively. NR, SA, CB, Accelerator M, TBBS stand for natural rubber, stearic acid, carbon black, 2-Mercaptobenzothiazole and N-tert-Butyl-2-benzothiazolesulfenamide, respectively. The samples in bold were used for the temperature-dependent studies.

Silicone Rubber Formulation

	SR	Silica	Cr_2O_3	PSiO-OH	Peroxide
SR-F33-C0.4	100	33	0.5	6	0.4
SR-F33-C0.8	100	33	0.5	6	0.8
SR-F33-C1.2	100	33	0.5	6	1.2
SR-F37-C0.4	100	37	0.5	6	0.4
SR-F37-C0.8	**100**	**37**	**0.5**	**6**	**0.8**
SR-F37-C1.2	100	37	0.5	6	1.2
SR-F43-C0.4	100	43	0.5	6	0.4
SR-F43-C0.8	100	43	0.5	6	0.8
SR-F43-C1.2	100	43	0.5	6	1.2

Natural Rubber Formulation

	NR	SA	ZnO	CB (N330)	Sulfur	TBBS	Accelerator M
NR-F00	100	0.5	5	0	3.5	0	0.5
NR-F10	100	2	5	10	2.25	0.7	0
NR-F20	100	2	5	20	2.25	0.7	0
NR-F30	**100**	**2**	**5**	**30**	**2.25**	**0.7**	**0**
NR-F40	100	2	5	40	2.25	0.7	0
NR-F50	100	2	5	50	2.25	0.7	0

3.2.2.2 Dynamic Mechanical Analysis (DMA)

The elastomers used for the temperature-dependent studies were characterized using DMA (TA instruments RSA III Dynamic Mechanical Analyzer, New Castle, DE). Samples were cut into $\sim$1 mm $\times$1 mm $\times$25.4 mm thin pieces as test samples for oscillatory tensile test on DMA. For each test sample, a logarithmic frequency sweep ranged from 10 Hz to 0.1 Hz was performed between -120°C to 110°C for silicone rubber and -60°C to 70°C for natural rubber, with a strain amplitude of 0.1%. The temperatures were increased every 5°C. The samples were soaked for 60 seconds before the measurement, and 21 data points were collected at each temperature during the frequency sweep. Representative DMA data are included in the supporting information.

3.2.2.3 Temperature Dependent Fatigue Tests

Mode I crack propagation tests were performed to examine the crack growth behavior under sinusoidal loading conditions. Figure 3.1 shows the experimental setup for the fatigue test. An ElectroForce linear motor from TA instruments was utilized to perform fatigue test using samples with dimensions of 25.4 mm × 25.4 mm × $\sim$ 1 mm loaded in a mode I pure shear geometry. The initial distance between the clamps, h_0 was $\sim$ 5 mm. The samples were run through cyclic sinusoidal displacement control with a displacement amplitude of δ_0. A pre-cycle stage of 2000 cycles was first applied at a frequency of 2 Hz without introducing a crack, such that the Mullins effect on the properties of the bulk material[17, 35, 52–56] during subsequent deformation of the material was minimized. The dependence of the modulus on the cycle number has been included in the supporting information. Because of the effect of strain softening and creep, a compression force was generated in the later rounds of cycles during the pre-cycle step. The maximum compressive stress was always low enough so that sample buckling did not occur, thus avoiding potential complications arising from this effect[57]. A schematic of the displacement and force signals are shown in Figure 3.4(a) and (b). After the pre-cycles, a razor blade was used to introduce a crack with a length of $\sim$2 mm into the sample, before another round of cyclic displacement using the same displacement amplitude of δ_0 at a frequency of 2 Hz. The fatigue tests continued until substantial crack propagation was observed, with the total time of an experiment varying from 2 hours to 5 days. The temperatures varied from 22 °C (room temperature) to 100 °C for SR and from 22 °C to 70 °C for NR.

The input energy and the crack propagation rate (increase in crack length per cycle), *da/dn*, were calculated through the stress-strain relation from the tests. The input energy, Γ, was obtained from the following equation[18]:

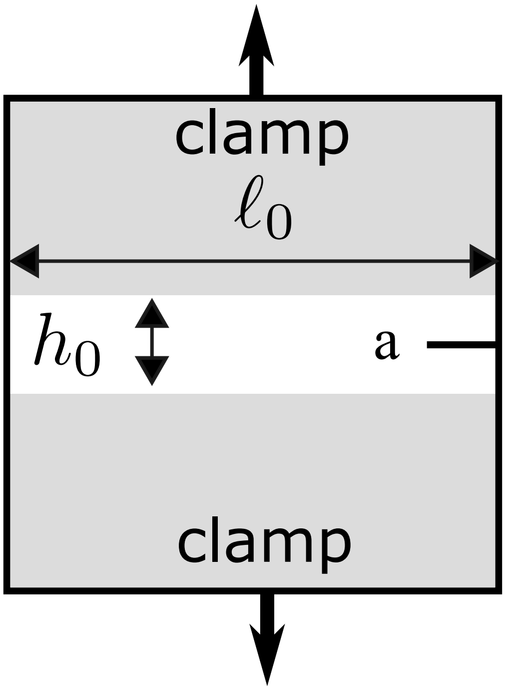

Figure 3.1: Pure shear test geometry used for the fatigue crack growth experiments.

$$\Gamma = h_0 \int_0^{\varepsilon_{\max}} \sigma_N d\varepsilon_N \tag{3.1}$$

Here, σ_N and ε_N are the stress and strain, respectively, obtained from the loading portion of the cyclic oscillation, and $\varepsilon_{\max}$ is the maximum tensile strain applied during a loading cycle. The crack length is determined from the mechanical stiffness of the sample as described in more detail in section 4.4. Note that the input energy that we define here is a measure of the total energy input from the external loading of the sample.

3.2.3 Crack Surface Visualization

The fatigue crack surfaces were visualized with an Olympus 3D Laser Confocal Microscope with a 10x objective lens.

3.3 Results and Discussion

3.3.1 Viscoelastic Behavior at Large Strains

3.3.1.1 Stress-Strain Relationships and Strain softening

Figure 3.2 shows the loading behavior of SR-F37-C0.8 and NR-F30 samples at different strain amplitudes for low (22 °C) and high (70 °C) temperatures. Here, the strain directly correlates to the input energy Γ (Equation 3.1), which quantifies the driving force for the crack propagation. All cycles are recorded from elastomer samples without a crack after the 2000 pre-cycles in order to account for the Mullins effect (illustrated in Figure 3.4(a)) in our calculation of the input energy. The Mullins effect is responsible for the decrease in the modulus from the value obtained from DMA at a strain of 0.1%, to the value obtained after 2000 cycles of deformation at a higher strain, as illustrated in Figure 3.3(a) for SR(-F37-C0.7) and in Figure 3.3(b) for NR. This modulus, obtained from the slope of the loading curve in the low strain regime, changes as a function of strain applied to the samples but is nearly independent of the temperature.

Parts (c) and (d) of Figure 3.3 illustrate the effect of composition on the moduli for a series of samples that have been strained to different levels for 2000 cycles at 22 °C. For the silicone rubber samples (Figure 3.3(c)) both crosslinking density and filler level were modified, with the filler effect having a much stronger effect on the modulus than the crosslinking density. This result is consistent with other recent results with a series of SBR (styrene-butadiene rubber) samples [58]. In natural rubber (Figure 3.3(d)), the stiffness does not increase and almost no strain softening is observed when the filler content is below 20 phr. When more than 20 phr of carbon black filler is added, the stiffening effect and strain softening effect become more obvious. The phenomenon that the elastic moduli remain high at low strain values and decrease rapidly when higher strains are applied is a manifestation of the Payne effect, which is mainly due to the continuous disruption of the filler network at increasing strains [59]. In both types of rubber, a higher filler content leads to more interactions between the filler particles, which agrees with the conclusion of the work of Merckel *et al.* [60] that adding fillers increases rubber softening.

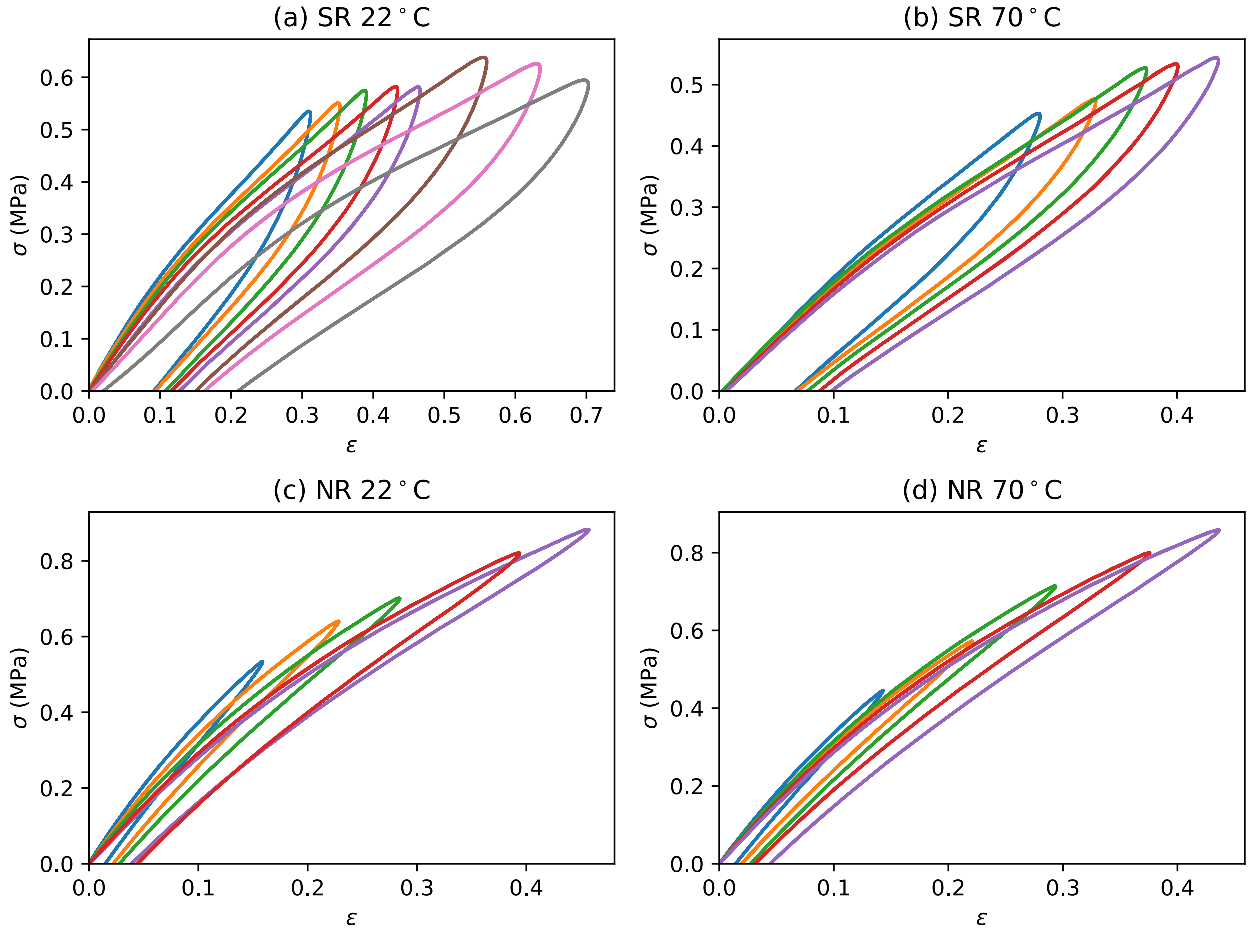

Figure 3.2: Stress-strain curves of SR-F37-C0.7 (a,b) and NR-F30 (c,d) for increasing strains after the 2000 pre-cycle step at room temperature (a,c) and 70 °C (b,d).

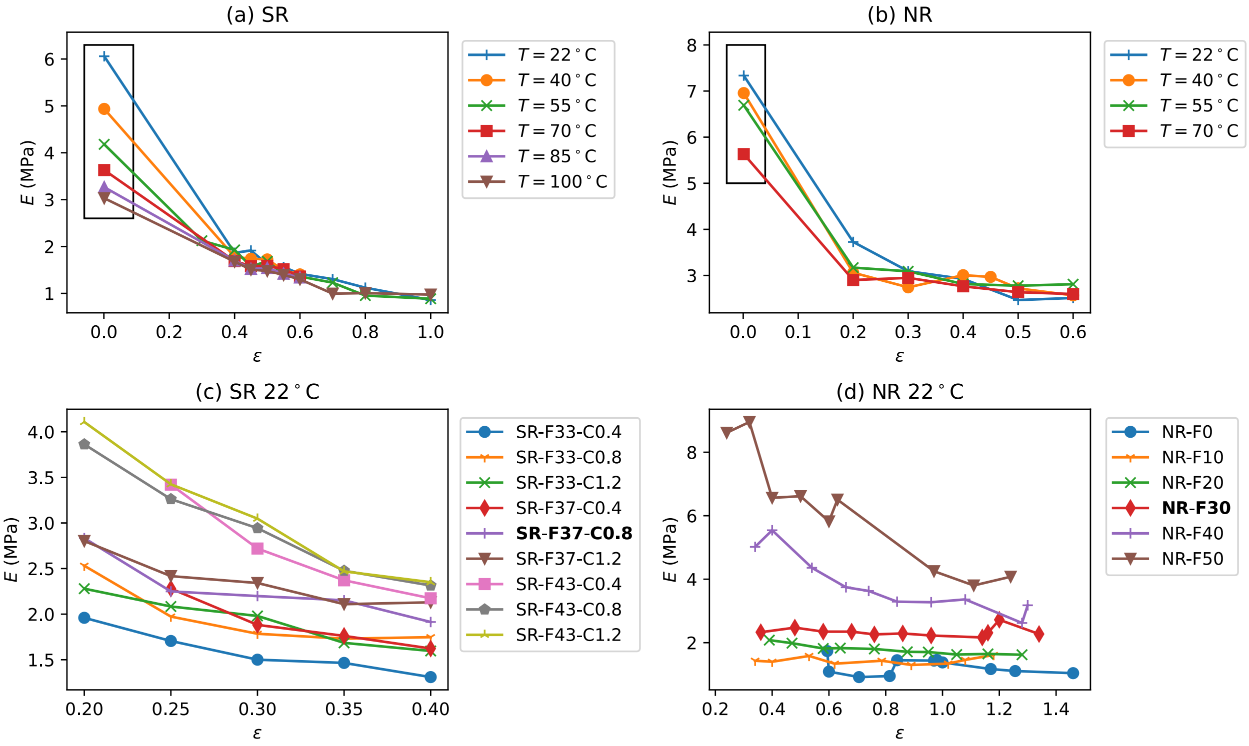

Figure 3.3: Elastic modulus as a function of strain at different temperatures for SR-F37-C0.8 (a) and NR-F30 (b), with the DMA data shown in the box; Elastic modulus as a function of strain for silicone rubber (c) and natural rubber (d) with different compositions of filler and crosslinking density at room temperature. The names of SR and NR samples, which are used for temperature dependent tests, are shown as bold in the legends.

3.3.1.2 Viscoelastic Dissipation

As stated in the previous section, the fatigue test requires a pre-cycle step for about 2000 cycles of oscillation with no crack introduced. This step is to remove the Mullins effect so that different tests can be compared to one another more easily. Examples of the evolution of the material response for SR-F37-C0.8 and NR-F30 during these first 2000 cycles is shown in Figure 3.4(a) and (b). The orange dashed curve shows the large hysteresis in the early cycles, and the solid blue curve shows the final, stable hysteresis loop after 1900 cycles. The hysteresis curves for $n = 1000$ are very nearly identical to those observed for $n = 1900$, indicating that our protocol of using ≈ 2000 cycles to condition the samples is sufficient. With the Mullins effect removed, the hysteresis loop was then used as a measure of the energy dissipation within the material during cyclic loading. For SR, more viscoelastic energy dissipation is observed than NR, which shows a more elastic behavior with a smaller amount of energy dissipation.

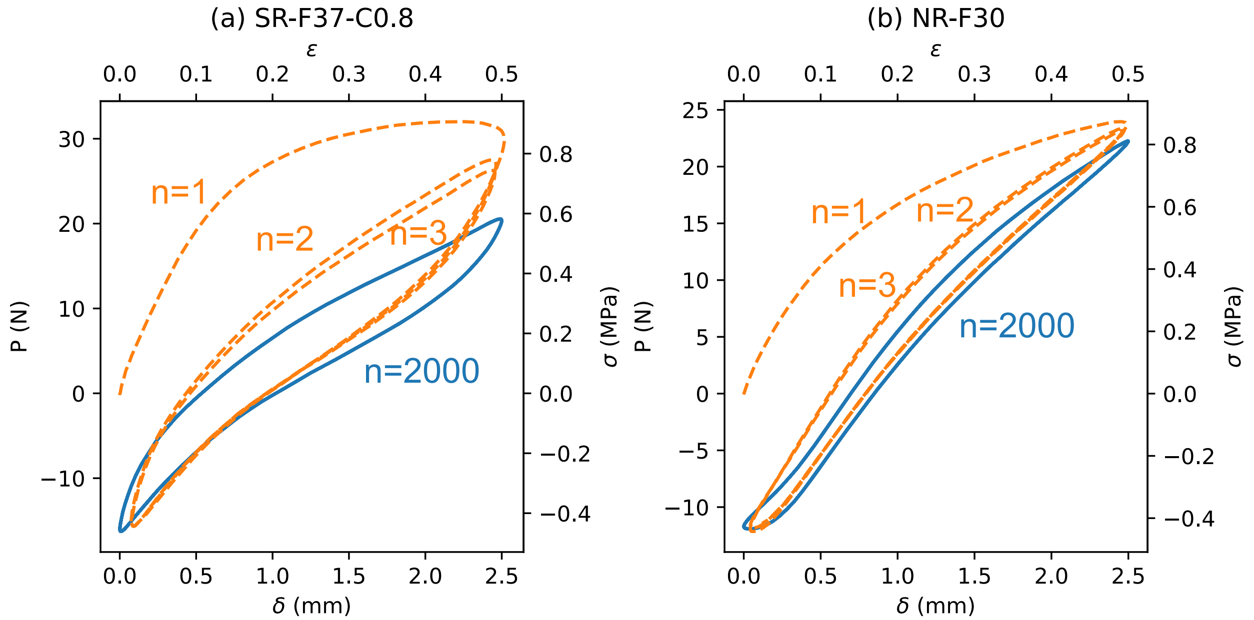
(a) SR-F37-C0.8

(b) NR-F30

Figure 3.4: Hysteresis loops showing the energy dissipation in the first 2000 cycles for an SR-F37-C0.8 sample (a) and NR-F30 sample (b) at 40°C (both strain = 0.5). Cycle n=2 and n=3 overlapped with each other in (b); Hysteresis curve after 2000 cycles for SR-F37-C0.8 at 40°C.

In order to quantify the viscoelastic relaxation of the elastomers, effective phase angles, ϕ_{eff}, were obtained from the mechanical responses of the oscillatory tests. With the measured values of load P, displacement δ and their peak-to-peak amplitudes (P_0 and δ_0), the value of effective phase angle ϕ_{eff} is based on energy dissipated from each cycle[61]:

$$\sin\phi_{eff} = \frac{4\int P d\delta}{\pi P_0 \delta_0} \tag{3.2}$$

Other measures of viscoelastic dissipation can certainly be employed as well. We utilize ϕ_{eff} as defined in Eq. 5.4 because it reduces to the viscoelastic phase angle for sufficiently small values of P_0 and δ_0.

Figure 3.5 shows the effective phase angles at different temperatures at low strain (0.1% from DMA) and high strain (from fatigue tests). Here we notice very different behaviors for the natural rubber sample and the silicone rubber sample. For SR, there is a small increase in ϕ_{eff} with strain amplitude, with the room temperature value of ϕ_{eff} increasing from $\approx 12.5^\circ$ to $\approx 15^\circ$ as the strain amplitude is increased from 0.001 to 1. Temperature strongly affects the SR behavior, with higher temperatures leading to lower values of ϕ_{eff}. NR is nearly perfectly elastic at very small strains, with $\phi_{eff} \approx 0$. At the larger strains relevant for the fatigue experiments, $\phi_{eff} \approx 5^\circ$ and is nearly independent of both strain and temperature over the range investigated here ($0.2 < \varepsilon < 0.6$ and $22^\circ\mathrm{C} < T < 70^\circ\mathrm{C}$). The same trend holds for other NR samples with different filler contents at room temperature.

At 22°C, values of ϕ_{eff} for SR are not strongly affected by changing the filler content or crosslinking density, and all ϕ_{eff} values fall into the same range between 12.5° to 15° (Figure 3.5(c)). For NR the effective phase angles are more strongly affected by the filler content, with substantial increases in ϕ_{eff} for carbon black amounts exceeding 20 phr. As silicone rubber is a non-crystallizing material, its properties are consistent with the general behavior of a viscoelastic material, with a value of ϕ_{eff} that increases slightly with increased strain amplitude. This increase in ϕ_{eff} is likely due to disruptions in the filler network at larger strains. These disruptions in the filler network affect the measured values of ϕ_{eff} in the natural rubber samples as well. In natural rubber, this filler effect is the dominant dissipation energy dissipation mechanism. For the strains accessed by DMA, which are low enough so that the filler network is not perturbed, very little viscoelastic character is observed, with a very low measured phase angle.

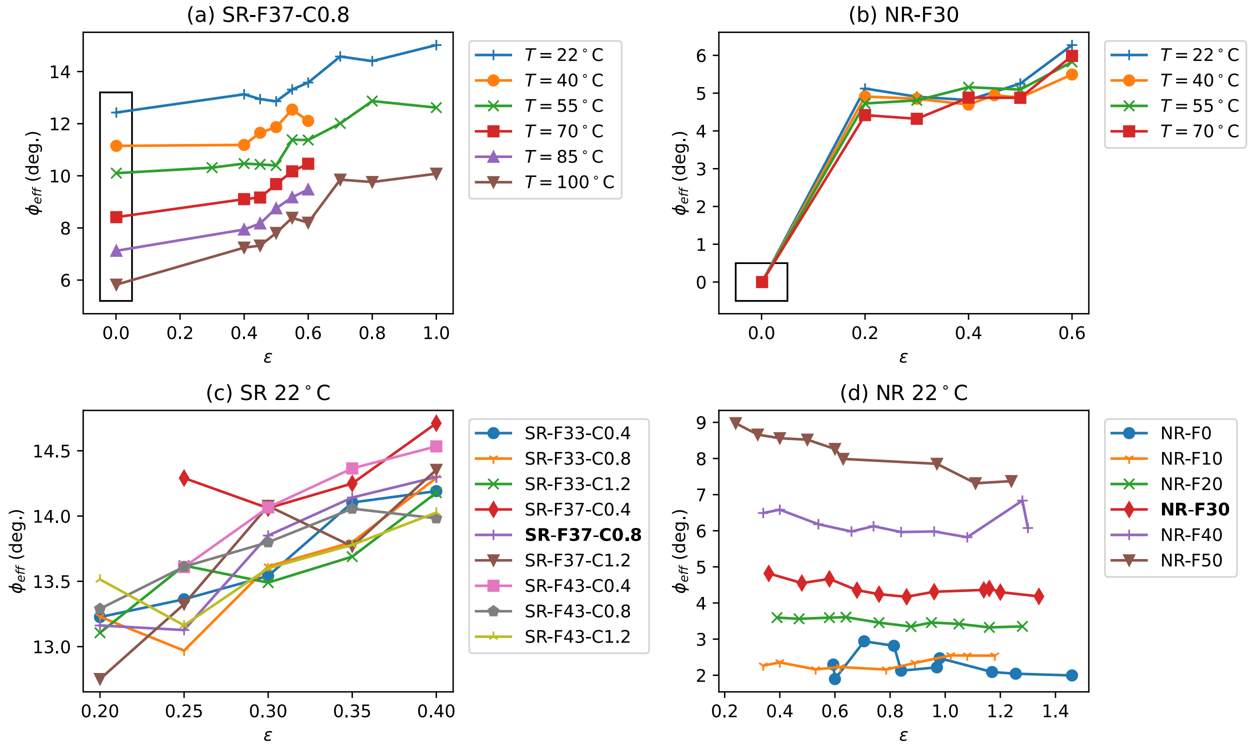

Figure 3.5: Effective phase angles ϕ_{eff} at different strain amplitudes at variable temperatures for SR-F37-C0.8 (a) and NR-F30 (b), with the DMA data shown in the box; Effective phase angles at different strain amplitude for silicone rubber (c) and natural rubber (d) with different filler and crosslinker level at room temperature. The names of SR and NR samples, which are used for temperature dependent tests, are shown in bold in the legends.

3.3.2 Fatigue Behavior

After the 2000 pre-cycles, a crack was introduced into the sample, which then propagated during the subsequent loading cycles. The method adopted to analyze the fatigue behavior is illustrated in Figure 3.6. The loading portions of the hysteresis loops from the fatigue cycles are extracted to analyze the stress-strain relation (shown in representative cycles in Figure 3.6 (a), (b) and (c), where n is the cycle number). As the crack grows, the load decreases as the strain remains the same. Figure 3.6 (d) shows the full 83524-cycle dataset of crack propagation during the fatigue process for one particular sample. Here, the elastic modulus is unchanged, and the load reduction is due to crack propagation. As a result, the fatigue curves collapse onto one another when normalized by a factor K, as illustrated in Figure 3.6(e). This factor K can be used to extract the crack length, a, from the following expression:

$$K = \frac{\ell_0 - a}{\ell_0} = 1 - a/\ell_0 = \frac{\sigma}{\sigma_0} \tag{3.3}$$

Rearrangement gives the following for a:

$$a = (1 - K)\,\ell_0 \tag{3.4}$$

Here, ℓ_0 is the original length of the sample and σ_0 is the nominal stress value prior to the introduction of the crack. Because the elastic modulus, E, is unchanged throughout the fatigue test, its value is given by the following expression:

$$E = \frac{\sigma_0}{\varepsilon} = \frac{\sigma}{K} \cdot \frac{1}{\varepsilon} \tag{3.5}$$

These expressions enable us to obtain the crack length directly from the measured load amplitude. Figure 3.6 (f) shows the crack length change over the fatigue process, where the crack growth rate *da/dn* is from the linear fitting of the curve. We directly measured the crack length by video observation of the crack during some of our room-temperature fatigue tests in order to confirm that this procedure provides accurate values for the crack lengths. Direct visualization of the crack length is difficult to accomplish in the oven used for our temperature-controlled experiments, and the procedure outlined in this section was used for that reason.

3.3.2.1 Stored and Dissipated Energy

Enhanced viscoelastic energy dissipation correlates with increased fatigue resistance because energy dissipated viscoelastically is no longer available to break covalent bonds in the material. One

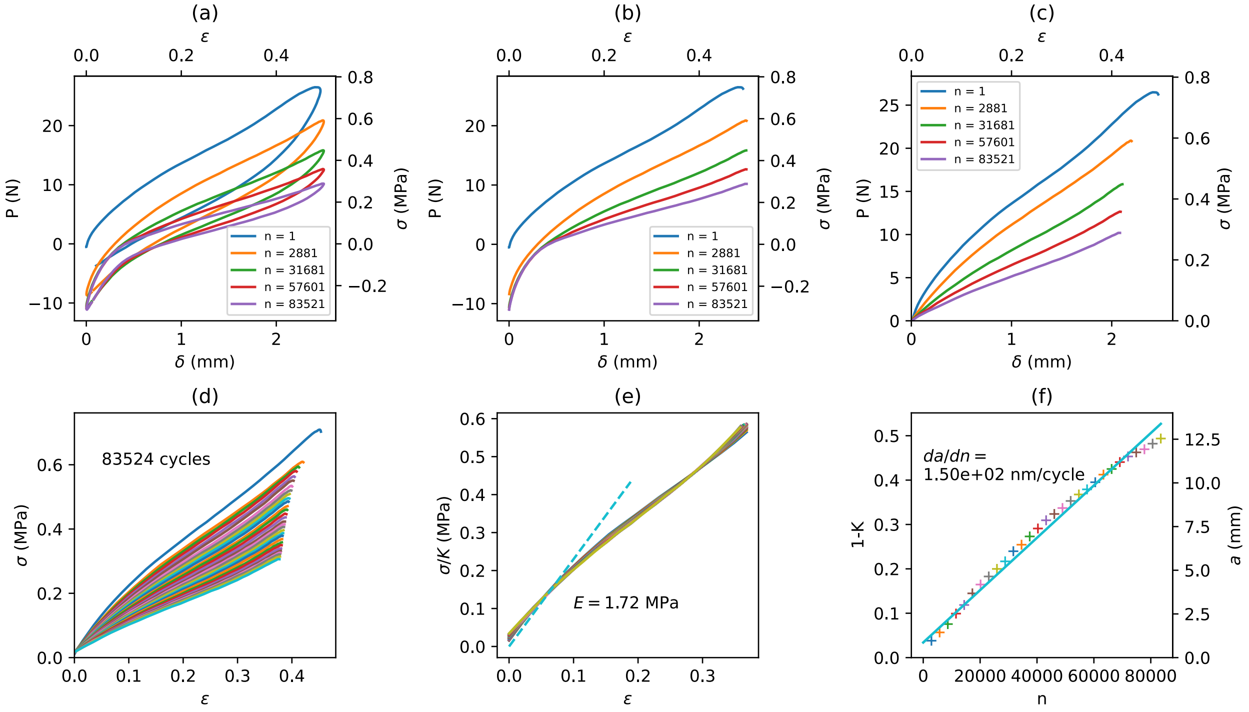

Figure 3.6: Illustration of the method for determining the crack length: Full hysteresis loops (a); Loading portion of the hysteresis loops (b); Loading curves after horizontal shifting to account for the creep response, so that $\delta = 0$ corresponds to the beginning of the tensile loading portion of the curve (c); Loading curves for all samples converted to stress vs. strain (d); Normalized loading curves illustrating the determination of the normalization factor, *K* (e); Plot of 1-K vs *n* to determine *da/dn* (f). Data are from a natural rubber sample at 40°C.

way to account for this is to divide the total external energy input expressed in Γ into a dissipative component, which we refer to as W_{diss} and a component that is available as stored elastic energy, $\mathscr{G}$. The concept is illustrated in Figure 3.7(a), where Γ is obtained from the integral under the loading curve and $\mathscr{G}$ is obtained from the integral under the unloading curve. For a perfectly elastic system with ϕ_{eff} =0, Γ= $\mathscr{G}$ and there is no ambiguity. Indeed, in most investigations of fatigue the input energy is taken as the integral under the loading curve (Γ in our notation) and is referred to as the energy release rate, $\mathscr{G}$. In systems where energy dissipation is quite large, as in the case of toughened hydrogels, for example, it is conventional to define Γ as the integral under the loading curve[62], and this is the convention we use here.

The fraction of the total input energy that is elastically available is given by the ratio $\mathscr{G}/\Gamma$, which in turn depends on the value of ϕ_{eff}. This point is illustrated Figure 3.7(b), where we plot this ratio as a function of ϕ_{eff} for the two samples for which temperature-dependent data were obtained. The solid line in this figure is an idealized calculation obtained for the case where the load oscillation is centered at $\sigma = 0$, with half the cycle in tension and half the cycle in compression. In this case we have $\delta = \delta_0 \sin(\omega t)$ and $\sigma_t = \sigma_0 \sin\left(\omega t + \phi_{eff}\right)$. The load/displacement curve shown in Figure 3.7(a) is for $\phi_{eff} = 10^\circ$, and gives $\mathscr{G}/\Gamma$ = 0.58. The idealized relationship obtained by repeating this procedure for all values of ϕ_{eff} gives a reasonable approximation to $\mathscr{G}/\Gamma$, although the details differ because the load curves in the actual experiments are not perfectly sinusoidal. Our point here in this section is that part of the increased fatigue resistance observed for samples with enhanced dissipation depends on the energy available to advance the crack is reduced from Γ to $\mathscr{G}$, and that this reduction increases with increasing ϕ_{eff}.

3.3.2.2 Relevant Length Scale for the Stored Elastic Energy

While the effective phase angle provides a useful measure of the available elastic energy, it does not give a complete picture of the actual energy that is available to promote crack propagation.

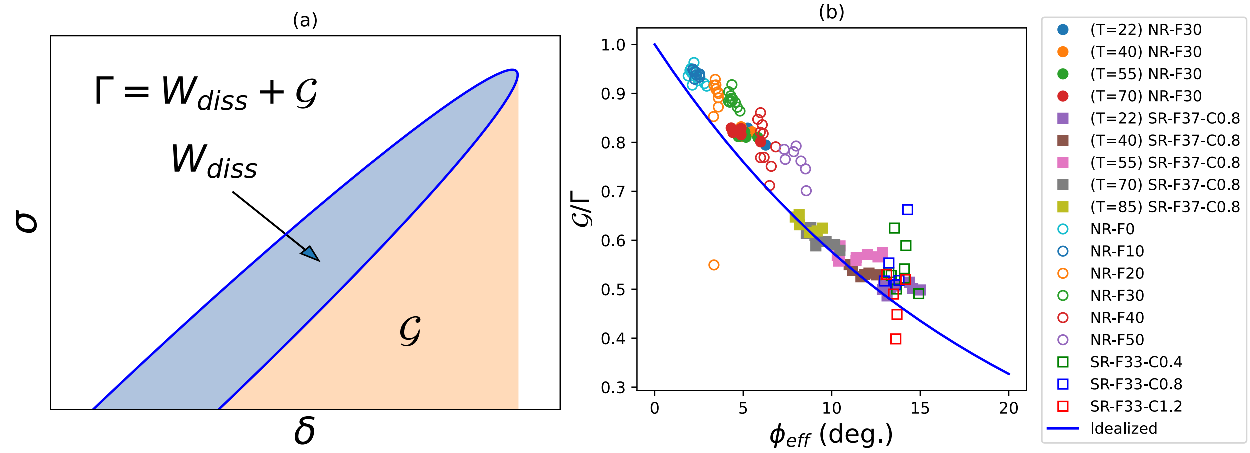

Figure 3.7: Schematic representation of the determination of W_{diss}, $\mathscr{G}$ and Γ from the load-displacement curve (a), and the values of $\mathscr{G}/\Gamma$ for the two samples for which temperature-dependent data were obtained (b). The solid line in (b) is the calculated relationship between $\mathscr{G}/\Gamma$ and ϕ_{eff} for the case where the load and displacement are both sinusoidal, as described in the text.

Conceptually this makes sense since one would not expect all of the elastic energy throughout a very thick sample to be available to flow and to be immediately released when individual bonds are broken. Mzabi *et al.* dealt with this issue by defining a 'local' energy release rate within a highly strained region. This energy release rate is defined as the area under the unloading curve, just as the 'global' value of $\mathscr{G}$ determined from the integral under the unloading curve. However, the relevant energy corresponds to the energy in a relatively narrow region in the vicinity of the crack tip with an undeformed height of H_0, which is much lower than the gauge length of the sample, h_0. This local energy release rate, $\mathscr{G}_{local}$, is then given by the following expression:

$$\mathscr{G}_{local} = H_0 \int_0^{\varepsilon_{local}} \sigma_N^{unl} \, d\varepsilon_N \tag{3.6}$$

Here, ε_{local} is a characteristic strain in the strain-hardened region in the vicinity of the crack tip, which is substantially larger than the far-field strain, ε. Even with this increased strain, $\mathscr{G}_{local}$ is about 10 times lower than the global value of $\mathscr{G}$ because H_0 is so much smaller than h_0. In the work of Mzabi *et al.*, $H_0 \approx 160$ μm, and we expect a similar value in our materials.

The development of a local strain energy criterion for fracture provides a useful framework for interpreting results related to fatigue and fracture of elastomeric systems. Note that because the strains in the crack tip region are much larger than the far-field strains, the value of ϕ_{eff} describing the relationship between stored and elastic energy in this region should also correspond to these much larger strains. In general the length scale, H_0, will be determined by a range of factors including the filler level, filler interactions, *etc.*, and can be obtained from local probes of the strain field using, for example, digital image correlation as in the original paper by Mzabi *et al* [17]. More detailed investigations of the deformation within the crack, obtained either during crack propagation [57, 63]or by imaging the morphology of the sample surfaces after crack propagation as describe below, may also provide some information related to this length scale.

A common way to describe the fatigue fracture behavior of elastomers is to plot the crack propagation rate, da/dn, against the input energy, Γ, in a double logarithmic plot. At relatively large values of Γ, a power law relation can be observed [17, 18, 24]: $da/dn = A\Gamma^{\alpha} + B$, where A, B and α are fitting parameters that can be used to characterize the material fatigue resistance and Γ is given by Eq. 3.1. However, as mentioned above, $\mathcal{G}$ serves as a more accurate expression for the stored elastic energy at the crack tip than Γ, and so we expect $\mathcal{G}$ to be a better measure of the actual available energy to propagate the crack. The term $\mathcal{G}/E$ is a general physical length scale used to describe a state where the material elasticity and fracture energy can couple to create new surfaces[1, 16, 64]. The elastic modulus, E, taken as the low strain modulus accounting for the strain softening due to the Mullins effect can sensibly be assumed to correlate with the concentration of bonds or matrix/filler interactions that need to be disrupted in order for fatigue cracks to propagate. Because the length scale of the highly deformed region, H_0, is difficult to determine unambiguously, it is useful to develop an empirical criterion involving quantities that are measured directly in a fatigue experiment. Here we normalize $\mathcal{G}/E$ by h_0, the total gauge length of the sample, as an independent variable that characterizes the far-field strain in the material, far from the crack tip. Figure 3.8 shows double-logarithmic plots of da/dn as a function of both $\mathcal{G}$ and $(\mathcal{G}/(Eh_0))$ for both types of rubber samples. It can be observed in Figure 3.8 (d) that the data of NR samples with different composition at different temperatures overlap with each other and show a uniform trend. For these samples da/dn can be approximated from the following simple expression:

$$\frac{da}{dn} = a_0 \left(\frac{\mathscr{G}}{Eh_0} \right)^{1.5} \tag{3.7}$$

where $a_0 \approx 2\mu$m for the NR samples. Eq. 3.7 can also be used to describe the fatigue data of the SR samples at room temperature, with $a_0 \approx 8\mu$m. Deviations from this power law behavior are observed for the SR samples at higher temperatures. We attribute these deviations to changes in the crack propagation behavior, similar to the transition between 'smooth' and 'rough' cracks observed in the gel fracture behavior of Seitz *et al.*[16] We observe a similar morphological transitions in our experiments, as described in more detail in the following section.

3.3.3 Fatigue Crack Surface

From Eq. 3.7 we can define a value of a_0 for each experiment, using measured values of da/dn, $\mathscr{G}$, E and h_0. For each of the NR samples a value of close to 2 μm is obtained for a_0. Images of the fracture surfaces for the NR samples are all similar to one another for these samples (shown in supplemental information), indicating that there is no mechanistic transition as $\mathscr{G}$ is changed. The situation is different for the SR samples. Figure 3.9 shows the fatigue crack surfaces on the SR-F37-C0.8 samples at $\varepsilon = 0.4$, which are the samples collected along the black dashed line in Figure 3.7(b). The temperature for each fatigue experiment, the corresponding measured values of ϕ_{eff} and the calculated values of a_0, are indicated on each figure. Different crack morphologies are observed in SR samples depending on the temperature of the experiment. At all temperatures tested, the morphologies show a step-like pattern, and the local-scale roughness is higher at low temperature while it becomes locally smoother at higher temperature. At 100°C, most patterns

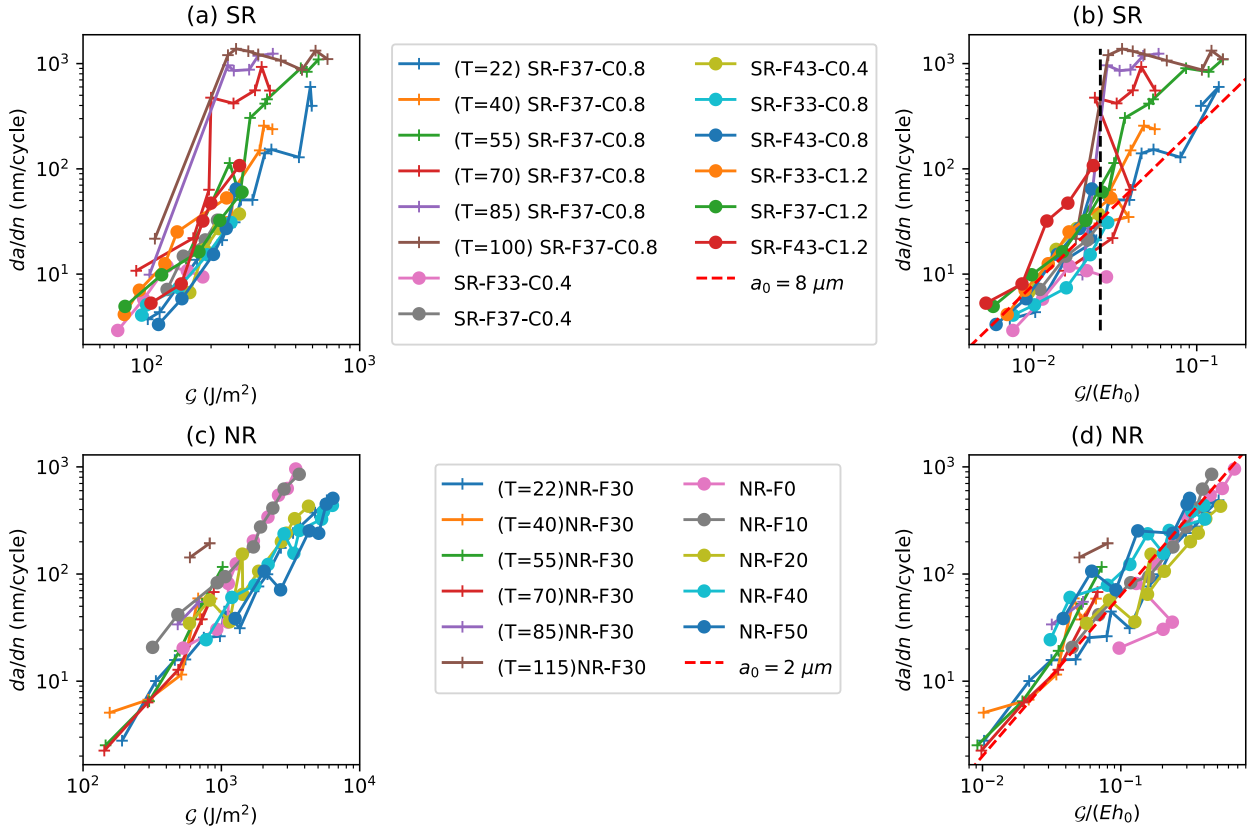

Figure 3.8: Logarithmic plots of crack propagation rate as a function of stored elastic energy $\mathscr{G}$ (a, c) and normalized stored elastic energy $\mathscr{G}/(Eh_0)$ (b, d). The dashed black line in (b) shows the locations of the data points of sample SR-F37-C0.8 at different temperatures that provides the fracture surfaces in Figure 3.9. The dashed red lines in (b) and (d) show the power law relation in Eq. 3.7.

disappear and form a smooth surface. This behavior differs from that of the NR samples, which show uniform roughness at all temperatures tested. This type of cross-hatched pattern has been observed previously in fractured surfaces of elastomers[65–70], with its appearance thought to be correlated to the speed of crack growth[69–71]. Gent *et al.* [65]and Krishnan *et al.* [72] proposed that the crosshatched pattern is created by non-colinear secondary cracks ahead of the crack tip that eventually reconnect with one another. The morphology transitions in the gel fracture experiments of Seitz *et al.* [16]were attributed to a certain threshold value of $\mathscr{G}/(Eh_0)$, that causes elastic instability and stress anisotropy at crack front. We see similar transitions in the fatigue crack propagation data for the SR samples, with increasing values of a_0 corresponding to smoother fracture surfaces.

Energy dissipation during crack propagation is controlled by processes occurring over different length scales, with much of the energy dissipated in a 'crack-related dissipation zone' [1]. The size of this zone is usually given by $\approx \mathscr{G}/E$, or $\approx 250\,\mu$m for the SR samples shown in Figure 3.9. This length scale and the height of the concentrated strain energy near the crack tip, H_0, are within the same order of magnitude. Persson *et al.* stated in their work that excess elastic energy in rubbery materials can be dissipated by increased surface roughness, increasing the surface energy stored on the crack surfaces [41]. Our hypothesis is that the power law behavior of Eq. 3.7 is representative of a set of tests where the roughness is relatively constant, with deviations in the roughness leading to different values of a_0. The situation is more complicated in a highly viscoelastic material like the ones investigated here. Figure 3.10 shows the fracture surface change at the same temperature (55°C) but different values of $\mathscr{G}/(Eh_0)$. For higher $\mathscr{G}/(Eh_0)$, we observe a gradually decreasing local roughness. This roughness decrease is analogous to the transition from 'rough' to 'smooth' cracks observed in the gel fracture experiments of Seitz *et al.*[16]. The more gradual nature of the transition in the experiments described here is likely due to the much stronger viscoelastic character of these materials.

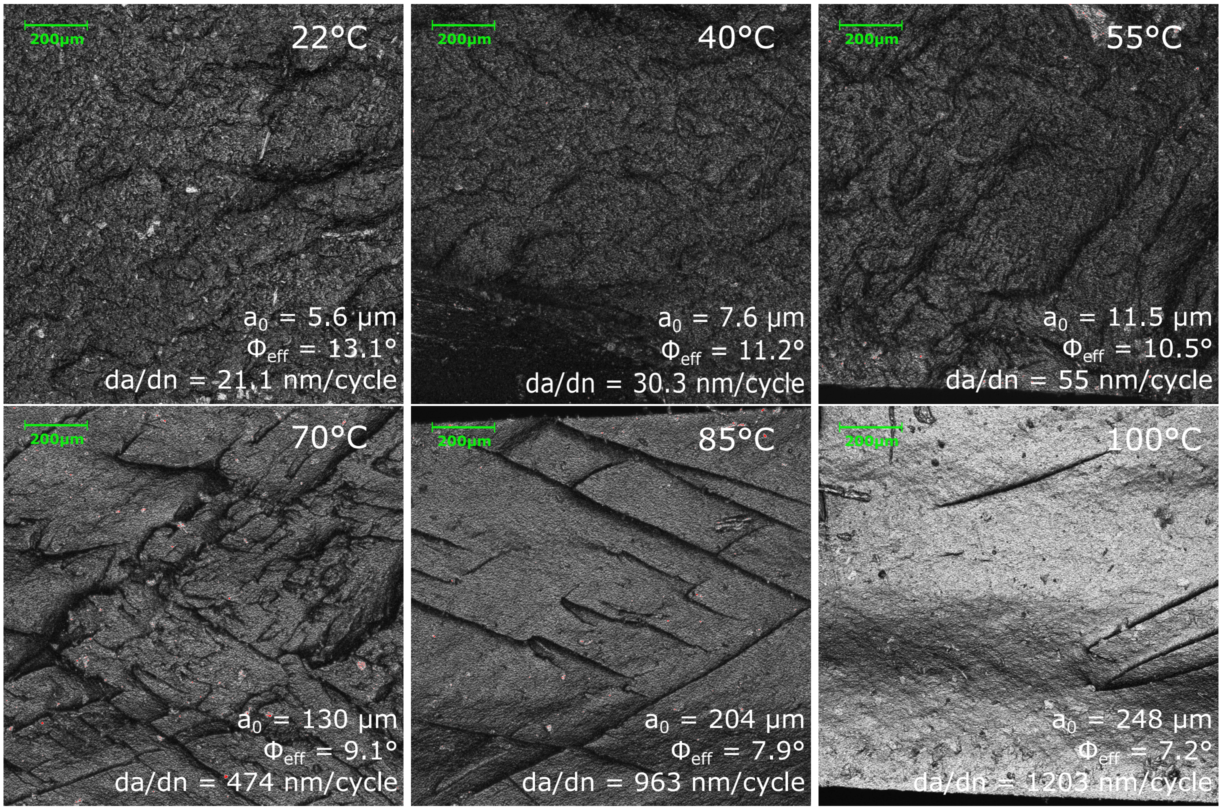

Figure 3.9: Fracture surfaces for a silicone rubber sample SR-F37-C0.8 after fatigue crack growth propagation at different temperatures, with $\varepsilon = 0.4$. The crack growth direction is from right to left in each case.

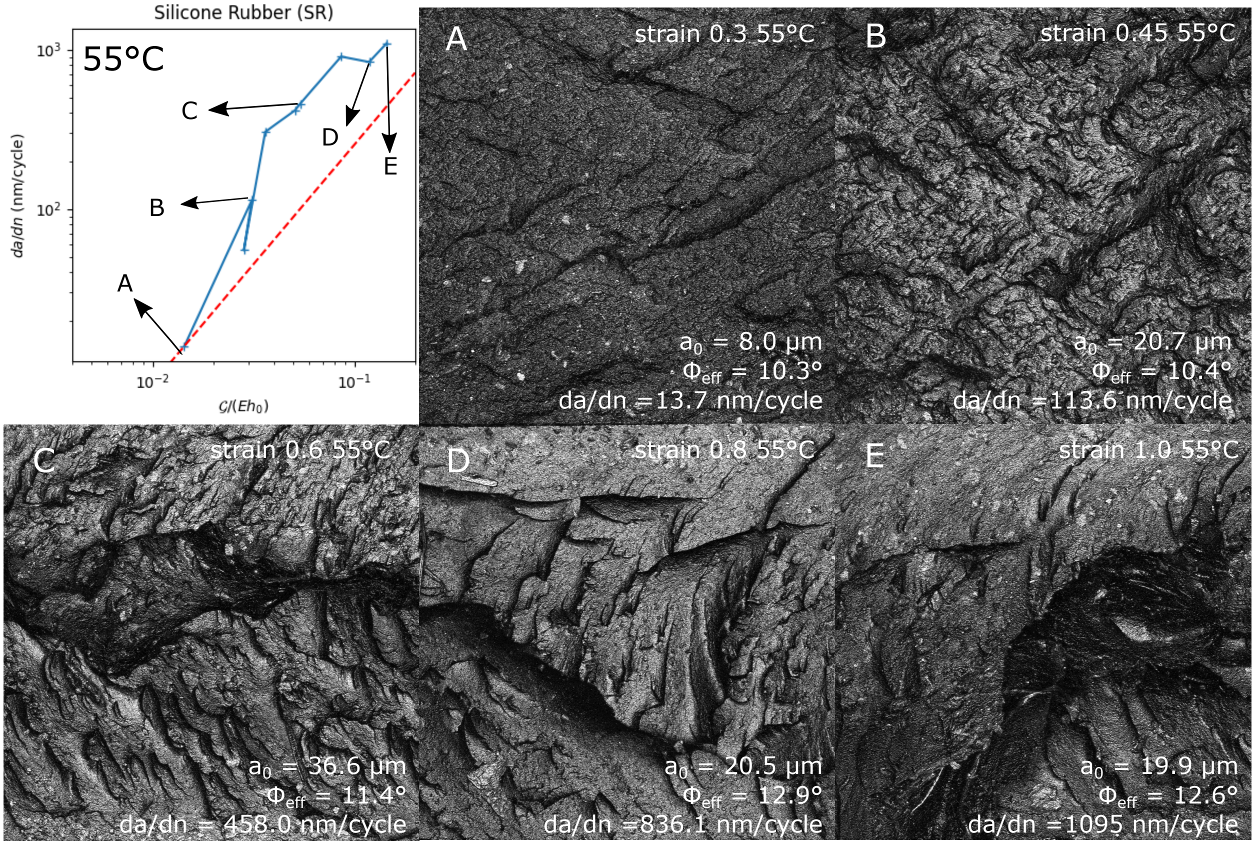

Figure 3.10: Fracture surfaces of silicone rubber sample SR-F37-C0.8 at the same temperature (55°C) at different strain amplitudes. The crack growth direction is from right to left in each case.

3.4 Conclusion

We have performed temperature and composition-dependent fatigue experiments on silicone rubber and used natural rubber as a comparison. We have determined the correlations between stored elastic energy ($\mathscr{G}$) and the input energy (Γ) during large-strain deformation. A strain-dependent effective phase angle, ϕ_{eff}, was introduced to characterize energy dissipation in the materials during cyclic loading, and this correlates well with the relationship between $\mathscr{G}$ and Γ. In the linear viscoelastic regime, ϕ_{eff} reduces to the phase angle determined from traditional dynamic mechanical analysis (DMA). For the silicone rubber samples ϕ_{eff} is only weakly dependent on the strain amplitude, and the change of filler or crosslinker level does not change ϕ_{eff} . The strain dependence of ϕ_{eff} for the natural rubber samples is much more substantial, increasing from ≈ 0 in the linear elastic regime to $\approx 5^\circ$ for strain amplitudes of 20% or larger for natural rubber filled with carbon black. Higher filler contents strongly increase the energy dissipation in natural rubber, though still lower than the silicone rubber samples, increasing ϕ_{eff} from $\approx 2^\circ$ to $\approx 9^\circ$.

Different responses to fatigue tests were observed for both elastomers. For natural rubber, both da/dn and ϕ_{eff} are nearly independent of temperature in the temperature range (22°C - 70°C) that we investigated, and its fatigue data overlaid well onto a power law relation with an power law index of 1.5 relating the fatigue growth rate, *da/dn*, to the normalized stored elastic energy, $\mathscr{G}/(Eh_0)$. For SR the same relation and power law index can be observed at low values of $\mathscr{G}/(Eh_0)$, with higher fatigue growth rates observed at higher temperatures. This deviation was attributed to changes in the crack propagation behavior, with smoother surfaces giving a larger fatigue crack growth rate at a fixed value of $\mathscr{G}/(Eh_0)$. Future work in this area should focus on the development of a more quantitative mechanistic understanding of the relationship between $\mathscr{G}/(Eh_0)$ and *da/dn*. The concept of a local energy release rate, $\mathscr{G}_{local}$, as introduced by Mzabi *et al.* [17] is likely to be particularly helpful in this respect. We also suggest here that the length scale a_0, the prefactor relating da/dn to $\mathscr{G}/(Eh_0)$ might be connected with length scales directly observable in the fracture surface morphology.

Chapter 4

Fatigue Crack Surface Morphology Analysis of Elastomers

During a fracture event, the crack tip develop fracture surfaces with distinct surface morphologies. The intricate patterns of the fracture surfaces as the crack tip traverses through the bulk material could contain intrinsic information of the crack propagation, and similar to the grooves of vinyl records, a more detailed overview can be given by studying the fracture surface patterns. We have observed varied fatigue fracture responses in both types of rubber samples due to the change of temperature environments and input strains, and have correlated the responses to the change of energy dissipation and the stored elastic energy during the unloading cycles. In this chapter, the fatigue fracture surface morphology of the rubber samples from Chapter 3 is investigated through different image processing techniques. The sample surface morphologies of both silicone rubber and natural rubber samples tested were captured with an Olympus 3D laser confocal microscope and reproduced in grey scale for further study. Methods of quantifying the overall roughness and local roughness are introduced and power spectral density function was utilized to analyze the step-like patterns for angle detections.

Parts of this chapter were adapted from “Crack Surface Analysis of Elastomers Using Transfer Learning” by Umar Ghumman, Qihua Chen, Vincent D’Angelo, Michael Clark, Jie Chen, Kenneth R. Shull and Wei Chen; ACS Applied Materials & Interfaces, 2023[73]. The database and the source code are available at: https://github.com/mail4umar/Crack-surface-analysis-using-Transfer-Learning.git. This project was funded under the Ford-Northwestern University-Alliance-Partnership. We would like to thank Alemayehu Admasu, Patrick Blanchard and Devesh Upadhyay from Ford Research for their support and collaboration. The contents of this work are also included in the thesis by Dr. Umar Farooq Ghumman, Microstructure Characterization for Analysis and Design of Microstructural Material System, August 2022. In addition, the authors acknowledge Zihao

Wang for useful discussions.

4.1 Introduction

Silicone rubbers are extensively used due to their durability under different conditions and applications including cookware, sound damping materials and medical devices. In such applications, silicone elastomers are often used under dynamic loading conditions, and they often fail due to fatigue. During a fatigue process, the factor that determines the lifetime of usage is the gradual growth of minor cracks over long periods of time. The goal of this study is to use image samples of such surface cracks to build and quantify their relationship with mechanical properties and environmental factors. There have already been extensive studies on elastomer viscoelastic properties, elastomeric fracture and fatigue in order to determine the factors and underlying mechanisms that influence the process of crack propagation[1, 11, 65, 66, 74]. One such theory of analysis is Linear elastic fracture mechanics (LEFM) which describes the fracture behavior of brittle materials and assumes linear elasticity in the bulk material except for the crack tip region where the crack tip propagation is characterized by the Griffith energetic criterion[11]. The Griffith crack propagation theory argues that fracture energy Γ is equilibrated by the strain energy G such that Γ = G at the point of failure. This theory can be extended for soft materials that form blunt crack tips with large strains and non-linear behaviors at the crack tips. Accordingly, energy dissipation is determined by different length scales near the highly stretched region of the blunt crack, as described by Creton and Ciccotti[1]. In the far-field loading zone, bulk energy dissipation occurs, and can be described by the viscoelastic properties of the material. Details of the crack propagation process dominate the behavior close to the crack tip. In a small region very close to the crack tip, material damage takes place at the molecular level. The related ridge-like material damage includes cavitation, fibrillation and the formation of secondary cracks[1, 65], resulting in distinct fracture surface morphologies. For this reason, we hypothesize that images of the fracture surface morphology contain information about the fracture process that be mined by subsequent analysis of the fracture surface.

In this study, we focus on previously reported crack surfaces of silicone rubber samples that were collected from fatigue experiments under different temperatures in Chapter 3. In the previous work, a change in crack surface morphology under different temperature and loading conditions was found, that when temperature increases, fatigue samples under the same strain show the transition from rough, cross-hatched surfaces to smoother surfaces. Here, we aim to identify the correlation between the collected mechanical properties and the observed patterns and to find the most important determining factors relevant to the formation of the surface morphologies.

4.2 Background

4.2.1 Surface Pattern Analysis

Fracture surfaces are historical imprints of a crack front that has traversed through the bulk material. Many studies described their observations and tried to explain the underlying mechanisms. In the 1950s, Thomas and Greensmith[74] reported the transition from a rough, irregular torn surface to a smooth surface along with the increase of crack speed in natural rubber and styrene-butadiene rubber. In addition to the irregular roughness, step-like, faceted surfaces were also found to commonly exist in amorphous materials, forming so-called crosshatch patterns[16, 66, 71], and they usually come with specific angles[67, 69]. There have been many attempts by researchers to establish correlations between the patterns on the surfaces of cracks in materials and their mechanical properties. Seitz et al. [16] and Baumberger et al.[67] attributed to the strong anisotropy generated with certain angles in the stress field[16, 67, 68]. Gent et al., Tanaka et al., and many other researchers elucidated by discussing the mode mixites and the intersection of secondary cracks ahead of the tip [65, 66, 68–70]. Wang et al. and Kolvin et al. focused on the energy equilibrium relation $G = \Gamma$ to elucidate the effects of energy flow at the crack tip and explained the cause of the morphology of crack surfaces and successfully explained the formation of microscopic branching in the crack dynamics[69, 75, 76].

Despite extensive discussions on fracture surfaces, the scope of the discussions is largely confined to the fast fracture of gels or crosslinked elastomers, with only limited attention given to fatigue experiments. Additionally, the time-consuming nature of fatigue experiments makes it challenging to generate a substantial amount of standardized and systematic data for a thorough study of the fatigue behavior of materials. Learning the fatigue fractography will not only help build a better correlation between the measured mechanical responses of the material and the created surface pattern, but also offers the possibility to predict fatigue properties from a fracture surface in future applications, potentially reducing the repetition of similar fatigue studies. In light of this, the characterization of surface roughness is a crucial step in quantifying the texture of a surface. By obtaining accurate information about the surface roughness, valuable insights can be gleaned for a deeper understanding of the underlying physics. Several concepts are employed to define the roughness of a surface in a quantitative manner, taking into account the diverse height differences present on rough surfaces. These parameters include Maximum Profile Height (R_p), Maximum Profile Valley Depth (R_v), Maximum Peak-to-Valley Height (R_z), Skewness (Rsk), Arithmetic Mean Height (R_a), and Root Mean Square Average of Profile Height (R_q). Among all the calculation methods, the R_a, and R_q are most commonly used. While each of the roughness characterization parameter has its own physical significance, the usage of power spectral density offers a more source of information for further analysis.

4.2.2 Power Spectral Density Function (PSD)

The Power Spectral Density (PSD) function is a widely used signal processing technique for characterizing the distribution and extracting important information from a series of signals, such as sound or surface roughness. This technique employs the Fourier transform to decompose the signal or time-series data into various wavevectors, s, allowing the energy distribution across different frequencies to be determined. By generating a series of sinusoidal waves that hold information at various scales, PSD provides a comprehensive analysis of the signal. For example, PSD can be used for human voice detection and noise filtering [77, 78]. Moreover, PSD has been employed in image analysis techniques. The PSD of a surface produces a 2-dimensional surface in frequency space, with each point in the space assigned the coordinate (u,v) that represents a sine wave of frequency $\sqrt{u^2+v^2}$ from the DC-value of the frequency space (0 frequency). As a frequency datapoint is where the frequency intensity changes the most, the 2D PSD frequency distribution displays the direction of the patterns in the image in orthogonal directions. The more regular and stronger the pattern, the more distinguishable it is as a "line" in the frequency space. When a pattern occurs to be higher frequency, it generally contains smaller scale information. On the other hand, the low frequency regime focuses on the larger contour of the image.

Many researchers have successfully used power spectral density to describe and analyze a surface captured from high-resolution microscope[79–81] by radially averaging the isotropic surface. The PSD approach offers distinct advantages beyond merely calculating roughness parameters of the surface, because it reveals statistical information in both lateral and longitudinal directions on the surface, while other roughness characteristic parameters only consider vertical information. This causes surfaces with the same roughness to exhibit very different topography, leading to inaccuracies[79, 82]. Assuming real-world situation that a rough surface scan is composed of discrete height information in each pixels, the forward and reverse discrete Fourier transforms (DFT) is more generally used in analysis, and a surface height profile can be expressed as:

$$\tilde{h}_{qx,qy} = l_x l_y \sum_{x,y} h_{x,y} e^{i(q_x x + q_y y)} \tag{4.1}$$

here $h_{x,y}$ is the height profile of the surface, q_x, q_yrepresents the frequency space axis, l_x, l_y are the pixel size, also expressed as the ratio between the number of grid points over the image edge length

$l_x = N_x/L_x, l_y = N_y/L_y$. The 2-dimensional PSD can be defined as:

$$C^{2D}_{qx,qy} = A^{-1}|\tilde{h}_{qx,qy}|^2 \tag{4.2}$$

where $A = L_x L_y$ is the surface area.

4.3 Materials and Methods

4.3.1 Materials

The materials used in these investigations, and the methods for conducting the fatigue experiments have been described in Chapter 3. The samples used for this study are filled silicone elastomers with a range of filler contents, investigated at different temperatures and different fatigue loading conditions. (Samples SR-F37-C0.8).

4.3.2 Data Acquisition

The fatigue crack surfaces were visualized with an Olympus 3D laser confocal microscope with a 10× objective lens. Figure 4.1shows the schematic of the setup. For each rubber specimen, multiple square-shaped crack surface images can be collected depending on the crack length after the fatigue experiment. Each image has a dimension of 1024 × 1024 pixels (~ 1.2 mm length). Figure 4.2 shows a set of representative sample images of one intensity image and one height image. Intensity image captures the brightness and luminance change of the figure, therefore recording details based on light source quality. Here, only height images are used for the machine learning process because the height images are presented in color gradients based on the height variations in 3-dimension. In addition, a datafile of the height data can also be exported so that

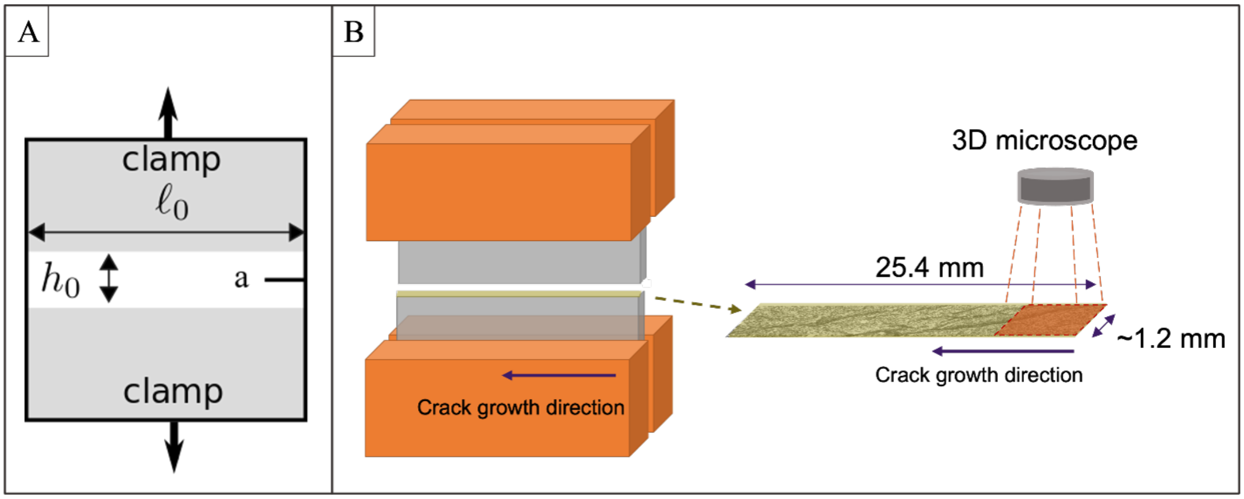

Figure 4.1: The experimental setup. (A) Model I fatigue test in pure shear geometry. The middle white area is the test area. An initial pre-crack 'a' was introduced before the fatigue test. (B) Schematic of the fatigue crack surface observation process using a 3D microscope.

the height image can be reconstructed using coding tools. Figure 4.2 shows a sample sets of an intensity image and a height image captured from a surface.

4.3.3 Data Processing

A complete mechanical property analysis of the same dataset can be found in Chapter 3. Its mechanical behavior is summarized in short in this section. The cyclic displacement will generate hysteresis loop on a stress-strain plot, with the area between the loading and unloading curve showing the amount of energy dissipation. From the small strain regime of the loading curve during the cyclic displacement, the effective elastic modulus E can be obtained from the slope of the stress-strain curve. The modulus E decreases with the increase of strain amplitude due to the Mullins effect and can be thought to be related to the concentration of bonds/matrix-filler interactions required to be damaged for fatigue crack propagation. The fatigue fracture behavior is described by plotting the crack propagation speed da/dn (nm/cycle, n is cycle number) as a function of the input energy Γ. In Chapter 3 we further proposed to plot the crack speed da/dn as a function

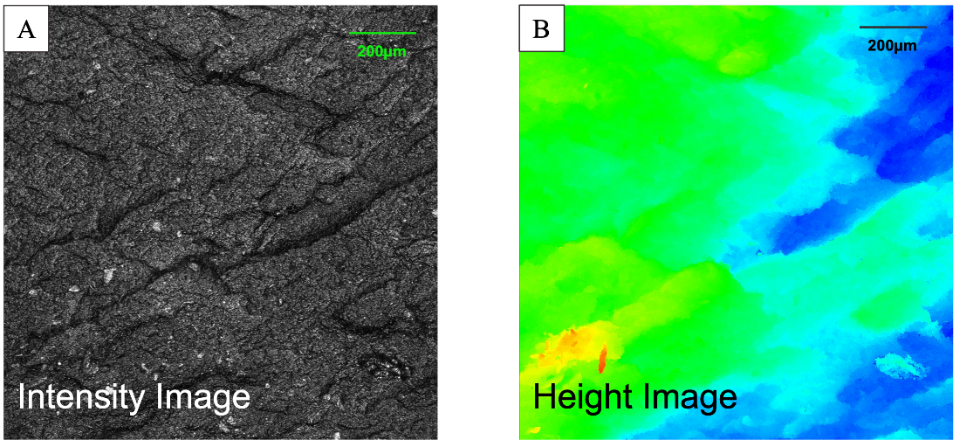

Figure 4.2: Sample sets of one intensity image (A) and one height image (B) from a 3D scan.

of G as the stored elastic energy at the crack tip. The silicone rubber fatigue data points overlaid onto a power law relation at room temperature (22° C) with a power law index of 1.5, while the high temperature data points deviated from the power law relation:

$$\frac{da}{dn} = a_0 \left(\frac{\mathscr{G}}{Eh_0} \right)^{1.5}$$

The fracture surfaces have different features as illustrated in Figure 4.3. These include the pattern formed by ridges that are formed by the intersection of multiple crack surfaces during the fracture process [5–7] . These patterns are most clearly observed in Figure 4.3(B). These ridges have a characteristic height, and the regions between the ridges also have a characteristic roughness, shown most clearly in Figure 4.3(C).

4.3.3.1 Surface Area Calculation

In order to study the relation between the energy dissipation conditions and the fracture surface roughness of the silicone rubber, surface area are calculated based on the height profiles. Each figure is cropped according to its actual cross-sectional area so as to exclude the height values that the microscope recorded off the sample. In addition, the absolute height values are not all the same

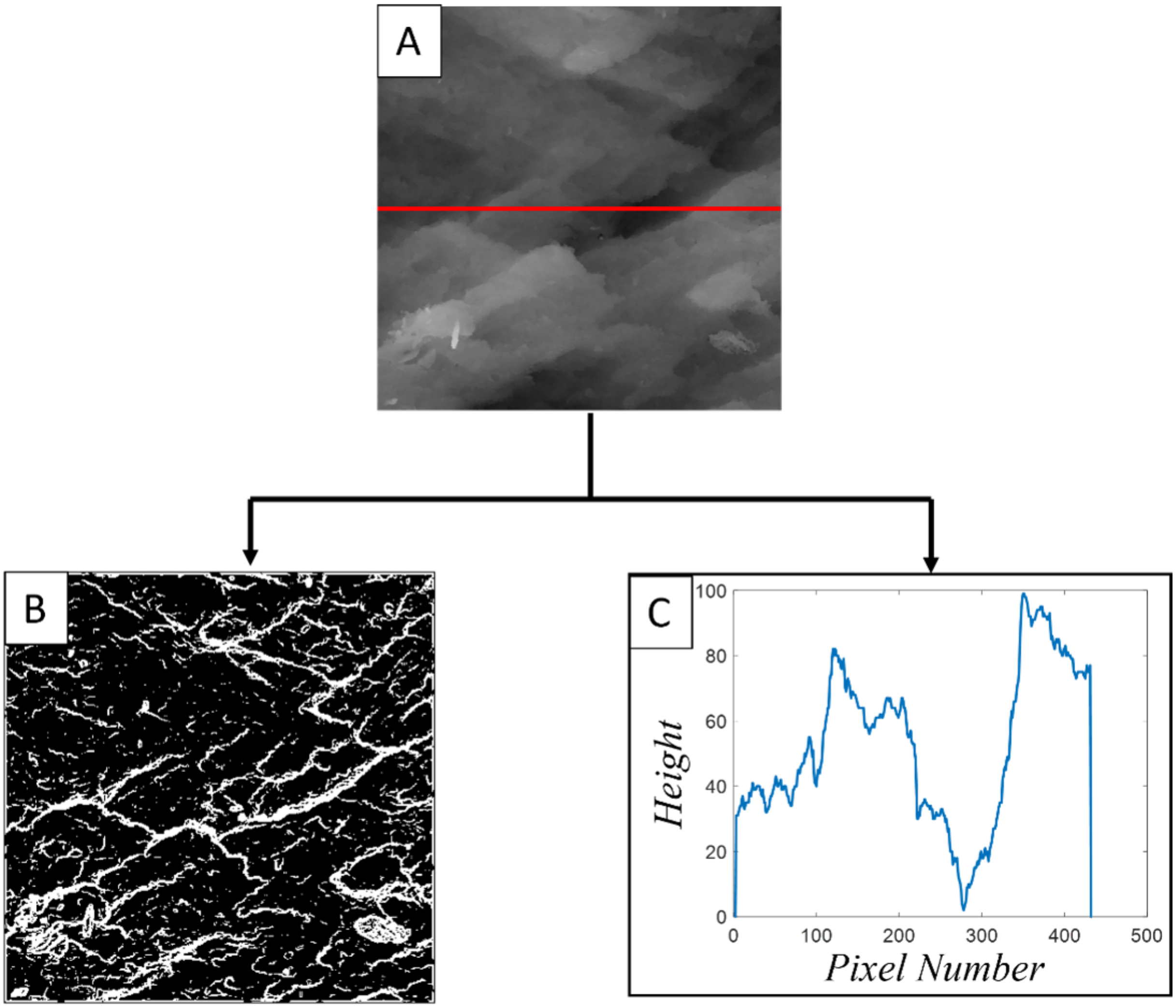

Figure 4.3: Characteristic features of a fractured surface of filled silicone rubber. (A): Grey scale height image of a silicone rubber sample. The red line is a line scan that provides 1D height information(C). (B): Binarized image highlighting the step-like patterns formed by the intersection of competing crack fronts during the fracture process. (C): Local roughness computed by scanning the red line over the original image in (A).

for all samples, as the baseline value of the height measurement is varied for each scan. To avoid the effects of the inconsistency, the surface area is calculated as the summation of the pixel-to-pixel height difference plus the surface dimension (length × width). After the summation, the surface area is normalized by the surface dimension. For each silicone rubber sample tested in a fatigue experiment, 2-9 figures are captured based on the crack length, providing an error range for the calculation.

4.3.3.2 Power Spectral Density Function

The PSD of each image was calculated by performing a Fast Fourier Transform (FFT) on the post-processed data. To dampen spectral leakage caused by the fact that height data cannot be represented by a periodic function, a Hann window was applied after the FFT. This involved multiplying a periodic windowing function to the non-periodic data, resulting in the removal of boundary discontinuity on the edge of the images. The squared FFT was then normalized by the size of the image to obtain a 2-dimensional PSD as shown in Eq. 4.2.

4.3.3.3 Step Pattern Angle Measurement

The computed 2D PSD is suitable to detect larger scale pattern shown on the fracture surface images. Figure 4.4 (A) demonstrates an example of a fracture surface with distinctive step-like pattern (shown as grayscale image reproduced from a height profile document) and its corresponding 2D PSD that was processed as described above in Figure 4.4(B). The pattern in the center of the 2D PSD plot indicates the presence of distinctive, larger scale patterns. Due to the parallel nature of the step-like patterns, the 2D PSD signals are strong enough for an angle measurement to suggest that there is a preferred direction for the pattern[67]. Angle-dependent power spectral density function *APSD* is calculated using the following equation:

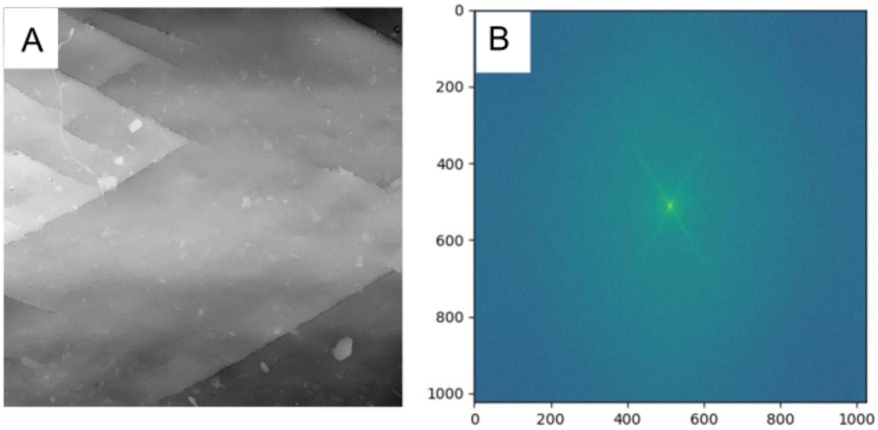

Figure 4.4: (A): A sample surface height profile in greyscale with distinctive step-like pattern and (B) the corresponding 2D power spectral density figure with the "X" pattern capturing the step-like pattern.

$$APSD = \int_{88^\circ+\theta}^{92^\circ+\theta} \int_{R_{min}}^{R_{max}} |\tilde{h}(q)|^2 r dr d\phi \tag{4.3}$$

where $-90^\circ < \theta < 90^\circ$, $\tilde{h}(q)$ is the 2D PSD in q space. Eq. 4.3 is integrating the 2D PSD about angle $\theta + \pi/2$ over an angular sector of 4°within the wavelength range $r \in [R_{min}, R_{max}]$, which is also the the radius from the center of 2D PSD[67]. Figure 4.5 shows the illustration of the APSD calculation on a 2D PSD plot.

4.4 Results and Discussion

4.4.1 Surface Area and Energy Dissipations

The surface area of each rubber fatigue surface sample is compared with the effective phase angle, which quantifies the energy dissipated from each cycle of oscillation. Figure 4.6 shows the normalized surface area calculated following the principle in section 4.3.3.1 as a function of the effective

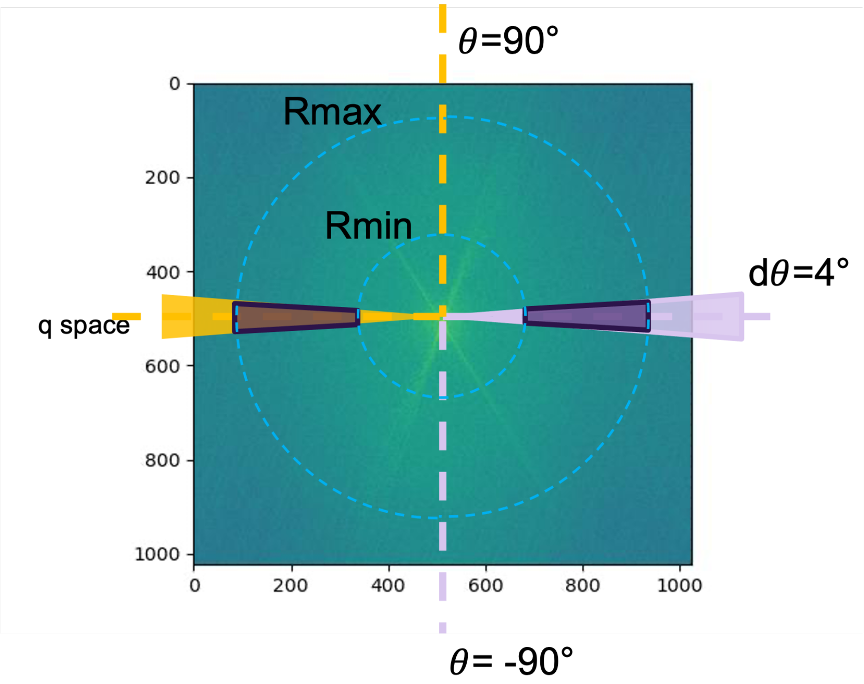

Figure 4.5: Illustration of the calculation of angular power spectral density function APSD. The pink and yellow dashed line indicates the boundary of the range of $\theta : -90^\circ < \theta < 90^\circ$, and the corresponding colored sector indicates the actual integrated area of the 2D PSD plot for APSD.

phase angle, which is obtained from the mechanical responses of the cyclic fatigue measurements using the equation $sin\phi_{eff} = \frac{4\int Pd\delta}{\pi P_0\delta_0}$, where P and δ are the measured load and displacement values and P_0 and δ_0 being the peak-to-peak amplitudes. A temperature dependence of ϕ_{eff} is found that the bulk energy dissipation decreased when energy increases, with the room temperature ϕ_{eff} ranges $12.8^\circ < \phi_{eff} < 14.4^\circ$ at $22^\circ C$ and higher temperature ϕ_{eff} ranges $6.4^\circ < \phi_{eff} < 10.1^\circ$ at $100^\circ C$. We have observed a correlation between the normalized surface area and ϕ_{eff}, indicating that higher viscoelastic dissipation in the material results in a greater surface area. According to existing literature, when extra energy is expended beyond what is required for Griffith's criterion for a planar crack, it is dissipated through the creation of a rougher surface. In figure 4.6, as the SR rubber becomes more dissipative at lower temperature, the fatigue fracture surface increases to dissipate extra energy during a crack propagation[83]. To quantify the relationship between the normalized surface area and ϕ_{eff}, a linear regression analysis was performed, shown as the extrapolating line in Figure 4.6. The slope of this linear fit line is 0.26, and the intercept is 1.73. If the material is perfectly elastic, $\phi_{eff} = 0$, and the normalized surface area is expected to be close to 1.73. The stored elastic energy available from the total energy input can be expressed as $\mathscr{G}/\Gamma$, and when we compare this quantity with the calculated surface area, it is better illustrated in Figure 4.7 that a larger portion of the stored elastic energy compared to the total energy release rate will result in lower surface area, and smoother surface. As higher temperature decreases the toughness of the material and makes the material less energy dissipative, it changes how the excessive energy dissipated at the crack tip, wither by creating rougher fracture surface or emission of elastic waves from the crack tip, increasing the crack velocity[83].

The symmetric angles of the step patterns are examined throughout the whole dataset by using Eq. 4.3 to calculate the APSD when a step pattern is obvious to observe. Baumberger et al. [67] showed the anisotropic features of mode I crack morphologies of gelatin slabs to have two symmetry-preserving maxima for $\theta = \pm\theta_m$. Here our sample present consistent behavior as reported in literature. Figure 4.8(B) shows the calculated APSD value normalized by the total APSD

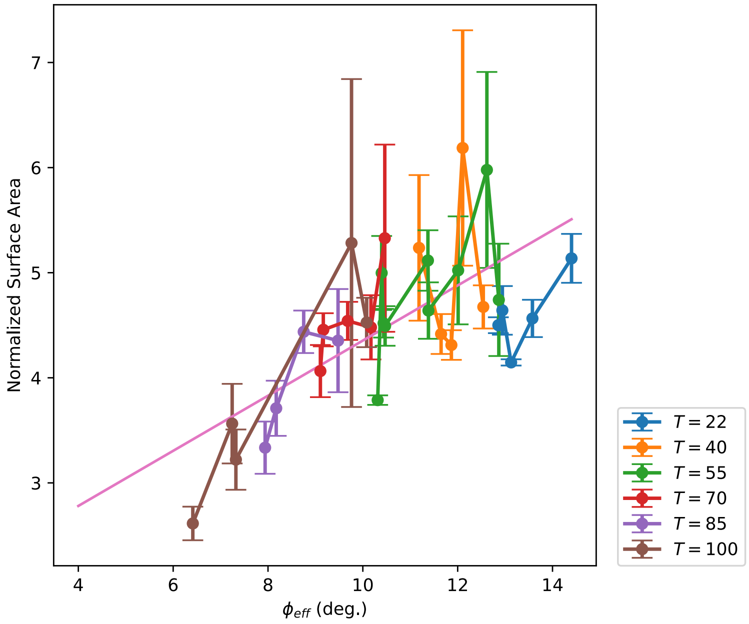

Figure 4.6: Normalized surface area as a function of the effective phase angle.

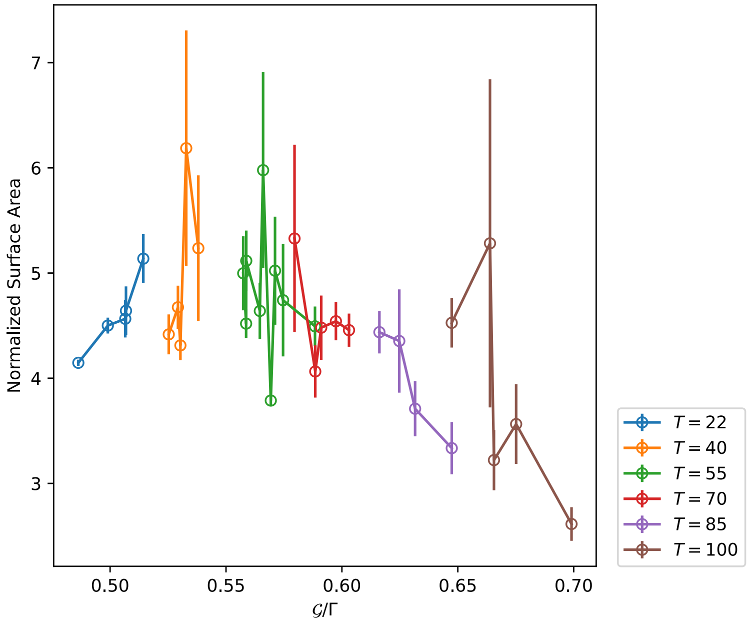

Figure 4.7: Dependence of stored elastic energy compared to the energy release rate of the normalized surface area.

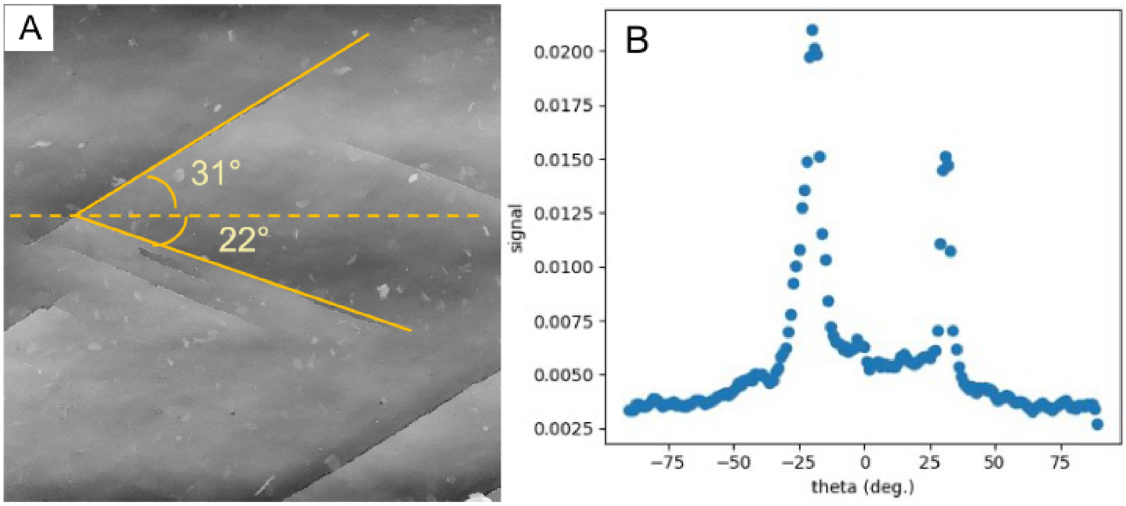

Figure 4.8: (A): Visualization of the angle detection of the surface morphologies using 2D PSD. (B): Normalized APSD (shown as 'signal' on y axis) as a function of the angle θ. The strong signal peaks represent the angles at which the step pattern varies the most.

of all angles and is presented as y axis signal. The APSD exhibits two prominent peaks at -22° and 31°, which are also observed in the representative cross-hatch in Figure 4.8 with the horizontal line serving as the reference for 0 degrees. With the same analytical criteria, Table 4.1 collects all the examined angle values from figures with distinctive cross-hatch/ step-like patterns. The results reveal that for silicone rubber samples tested under different conditions during a fatigue test, the symmetry-preserving maxima angles are independent of both strain amplitude and temperature. The mean angle between the corners of the step patterns was found to be approximately 50°, with a low standard deviation of 4.52 across all samples. In comparison, another more brittle silicone hybrid material was found to have a larger mean angle between step corners of 65.8°, with a standard deviation of 6.4. The natural rubber samples are not discussed here, as all the samples do not show a distinguishable step-like pattern. The observation of different angles between cross-hatch/step-like patterns in various materials suggests that this may be a material-specific mechanism for dissipating energy by forming secondary cracks ahead of the primary crack tip, as proposed in previous studies [66, 71].

In addition, the formation of step-like pattern has been reported to be velocity dependent[16, 69].

Strain	T ($^{\circ}C$)	Angles (°)	Total Angle (°)	Mean	Standard Deviation
0.3	100	-20, 31	53	50.4	4.52
		-20, 30	50		
0.4	85	-20, 33	53		
	100	-30, 23	53		
0.8	100	-37, 3	40		
0.45	22	-23, 22	45		
		-35, 18	53		
	70	-14, 35	49		
		0, 55	55		
	85	-18,30	48		
		-12,38	50		
	100	-24,32	56		

Table 4.1: Step pattern angle detection from crack interfaces which show distinctive step-like patterns.

Figure 4.9 shows a qualitative illustration of the observed surface patterns, which are categorized as one of three types: smooth with stepped patterns, rough with no steps and a mixed pattern with features of the other two. The bottom three figures show representative surfaces for the three categories. It is observed that the formation of the first type of sample (smooth with stepped patterns) is correlated with the crack advance per cycle, being observed for da/dn above about 400 nm/cycle. This is consistent with the reported observation of Seitz et al.[16] that cracks transform from rough to smooth with increasing speed.

4.5 Crack Surface Analysis of Elastomers Using Transfer Learning

In addition to the discussion above, machine learning techniques such as transfer learning is adopted to analyze the fractography of the fatigue crack surfaces. More detail can be found in [73]. In this study, a Transfer Learning (TL) based approach is developed to augment crack-surface analysis of complex microstructures with limited image data, where the surface morphology can-

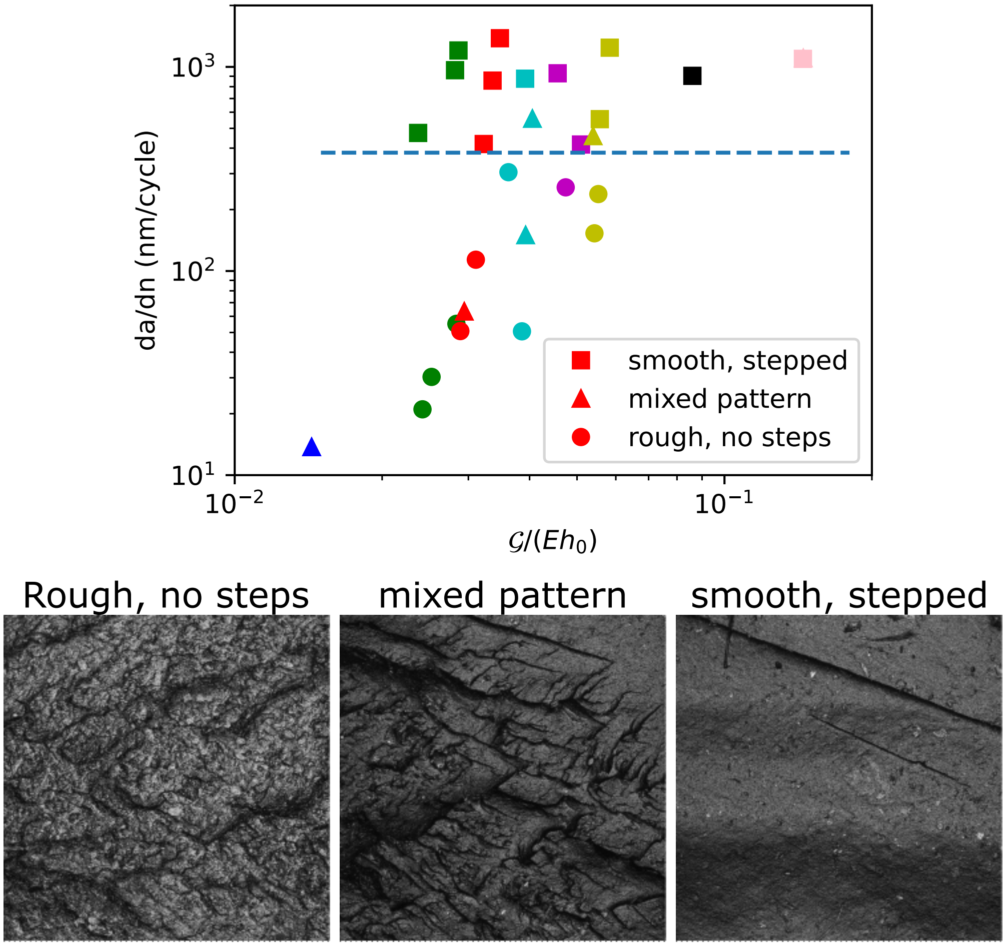

Figure 4.9: Qualitative visualization of the surface pattern distribution of the samples. Top plot: Relationship between the crack advance per cycle and the normalized crack driving force. The symbol shapes indicate the type of surface pattern observed and symbols with the same color were performed with the same strain amplitude. Bottom figures: representative images illustrating the three types of surface patterns, obtained for a strain of 0.45 and a temperature of 22°C (left), 70°C (middle), or 100°C (right).

not be characterized in a straightforward way. To use TL for surface feature-property mapping, a pre-trained model is pruned to retain the pre-trained weights of the convolution layers so that only a few weights of our custom layers are needed to extract relevant underlying microstructural features with limited data. The extracted features are determined based on how strongly they are correlated with the properties of interest. This technique is first applied to a test dataset for which the microstructures are created using the spectral density function (SDF), and the optical properties are calculated by physics-based simulations. Even on a small dataset of 224, a 90% test R2 value is able to be achieved, demonstrating the effectiveness of the approach. Next, the framework is applied on the crack surface of silicone rubber to achieve two goals: (i) to analyze the surface and calculate correlations of crack surface with different properties, and (ii) to build a predictive model that can estimate the input conditions responsible for the crack surface. For (i), we were able to quantify the relationships between the two patterns (ridge-like patterns and smaller-scale roughness) with properties of interest associated with fatigue fracture behavior. For (ii), we built predictive models by adding strain, and temperature data to the height images, giving a test R2 accuracy of 0.85, which indicates that the surface pattern change is most relevant to da/dn, which is the crack propagation speed. This accuracy is achieved with only 194 images of which only 70% are used as training, which shows the efficacy of the approach. With more data, we anticipate building an more accurate model.

4.6 Conclusion

In this chapter, we analyzed the crack surface morphologies of silicone rubber fatigue test samples from Chapter 3 using various approaches. It is shown that as temperature increases, the energy dissipation of the silicone rubber decreases, and the fatigue crack surface area decreases, indicating that less energy has been distributed to create more surface roughness. We have also used power spectral density function to quantitatively calculate the symmetry maxima angles along the crack propagation direction in the fatigue tested samples. We believe that the angles are generated by secondary cracks ahead of the crack tip and their magnitudes are material-dependent. Additionally, we also manually characterize the surface patterns and present the qualitative visualization on the crack propagation rate as a function of the far-field strain $\mathscr{G}/Eh_0$ and we found that the step-like patterns are most likely to appear when da/dn is above 400 nm/cycle. We then utilized machine learning technique and validated that the surface pattern of silicone rubber fatigue samples are most relevant to the crack speed with a 0.85 prediction accuracy of the model.

Chapter 5

Interpretation of Bulk and Adhesive Fatigue Damage in Pressure-Sensitive Adhesives

This project is supported by 3M company. We would like to thank Evan Breedlove, Joel Abrahamson and the AMX Lab at 3M for their support and collaboration. Additional adhesive fatigue tests are included in the Appendix B.

5.1 Introduction

Pressure-sensitive adhesives (PSAs) are ubiquitous bonding agents that rely primarily on van der Waals interactions to adhere to a wide range of surfaces. PSAs find diverse applications in daily life, including packaging, building construction, automotive and electrical appliances. These adhesives are typically composed of lightly crosslinked acrylic copolymers with a low glass transition temperature (T_g), and are often formulated with small molecule tackifiers to enhance their bonding capability to various surfaces[3, 84]. Like other elastomeric materials, PSAs are expected to withstand repeated shear loading over an extended periods of time. For example, PSAs used for adhesive hooks experience steady-state creep over long periods of time when holding heavy objects, and may also experience vibrations or other variations in load during use. Therefore, developing a reliable way to characterize the fatigue behavior of the PSAs becomes crucial during the design and manufacturing processes of the adhesive products.

In spite of its importance, methods for characterizing the fatigue behavior of soft adhesives are limited. Many measures have been adopted to quantify the mechanical properties of PSAs via adhesion tests including peeling tests[9, 85–87], dynamic overlap shear tests[88–90], and probe tack tests[1, 3, 26–28, 31, 91, 92]. Very few of these methods have focused on quantifying the fatigue behavior of PSAs. Other studies have focused on the fatigue and crack behavior of structural adhesives on adhesively bonded joints[93, 94], which usually exhibit high bond strength, creating permanent bonds that requires different comprehensive curing process, such as heat, UV light or other chemical reactions. These test methods are designed for rigid materials and are difficult to apply to a soft adhesives, however. To cope with this challenge, industry professionals often rely on folding machines to evaluate fatigue life and material property changes for lightly crosslinked, soft PSAs[10]. These folding machines subject the adhesives to repeated folding events to simulate the bending conditions experienced in real-world applications. These measurements do not capture the full stress/strain response of the material and cannot readily be interpreted in a way that can guide adhesive design. This lack of detailed data highlights the need for a more reliable, affordable and achievable testing method to better address the fatigue behavior of PSAs.

The present discussion examines two distinct failure modes of PSAs: cohesive failure and adhesive failure. Cohesive failure refers to the rupture of internal bonds within the bulk material of the PSA, while adhesive failure takes place at the interface between the two joined surfaces[9]. Since both cohesive and adhesive failure modes can occur during the extended use of PSAs, it becomes essential to thoroughly investigate their fatigue behavior in both scenarios. This work aims to examine both the bulk and interfacial properties on PSAs under large strain cyclic loading, providing a comprehensive picture of their fatigue behavior. Our approach presents a more cost-effective and alternative solution for obtaining preliminary fatigue data in the industry, offering a reliable baseline to assist with product selection and formulation optimization.

5.2 Materials and Methods

5.2.1 Materials

The PSAs used in this work are commercial 3M$^{\text{TM}}$Contrast Enhancement Films (CEF35 and CEF05) which were used as received. Both samples are acrylic-based, unfilled, lightly crosslinked PSAs with an adhesive layer thickness of 50 μm.

5.2.2 Dynamic Mechanical Analysis (DMA)

To gain insight into the mechanical behavior of the sample within the linear viscoelastic regime, dynamic mechanical analysis (DMA) was conducted. The analysis included a temperature sweep test, a frequency sweep test, and a strain sweep. For the temperature sweep, the samples were oscillated at 1 Hz between $-44\,^{\circ}$C and $120\,^{\circ}$C for CEF35 and $-50\,^{\circ}$C to $50\,^{\circ}$C for CEF05. For the logarithmic frequency sweep, both samples were tested between 0.01 Hz to 15 Hz at room temperature. Both the tests were carried out utilizing a torsional geometry on samples of 1 mm thickness with an 8 mm diameter. The applied strain amplitude was kept at a 0.01%. During the strain sweep, the samples were cut into dimensions of 3 mm × 1 mm × 30 mm and characterized using DMA (TA Instruments RSA G2). The test were performed at 2 Hz under room temperature ($23\,^{\circ}$C) with the strain amplitude ranging from 0.01% to 10%. All samples were soaked for 60 seconds before the measurement.

5.2.3 Bulk Fatigue

Pure shear geometry is commonly used to investigate fracture and fatigue behavior of materials[33, 73, 95]. In this study, uncut pure shear PSA samples were utilized for the sinusoidal cyclic fatigue damage in the bulk of the material [2, 19]. To achieve detectable load values for the 200N load cell, the samples were laminated with 16 layers, resulting in a total thickness of 0.8 mm. Samples with a length ℓ_0 of 25 mm and a gauge height (h_0) of 5 mm were loaded into an ElectroForce Linear motor from TA instruments (Figure 5.1(a)). During each round of testing, the samples were subjected to a displacement-controlled sinusoidal strain amplitude of 150% for 3600 cycles at a frequency of 2 Hz, shown in figure 5.1(b). Then, the samples were set to rest at 0 displacement for 30 minutes. The samples recovered their original shape during this recovery phase. sEach step of testing and resting counted as one round, and this process was repeated six times to assess the material's fatigue response under repeated elongation. After the sixth round, the samples were allowed to recover at 0 displacement for another 48 hours before undergoing another three rounds of testing with the same procedure. Figure 5.1(c) shows a graphical illustration of the described testing procedure. The 48-hour recovery time was introduced to reduce the strain-softening effect to the greatest extent feasible. The subsequent three rounds of testing were conducted to determine whether the observed fatigue behavior was permanent or not.

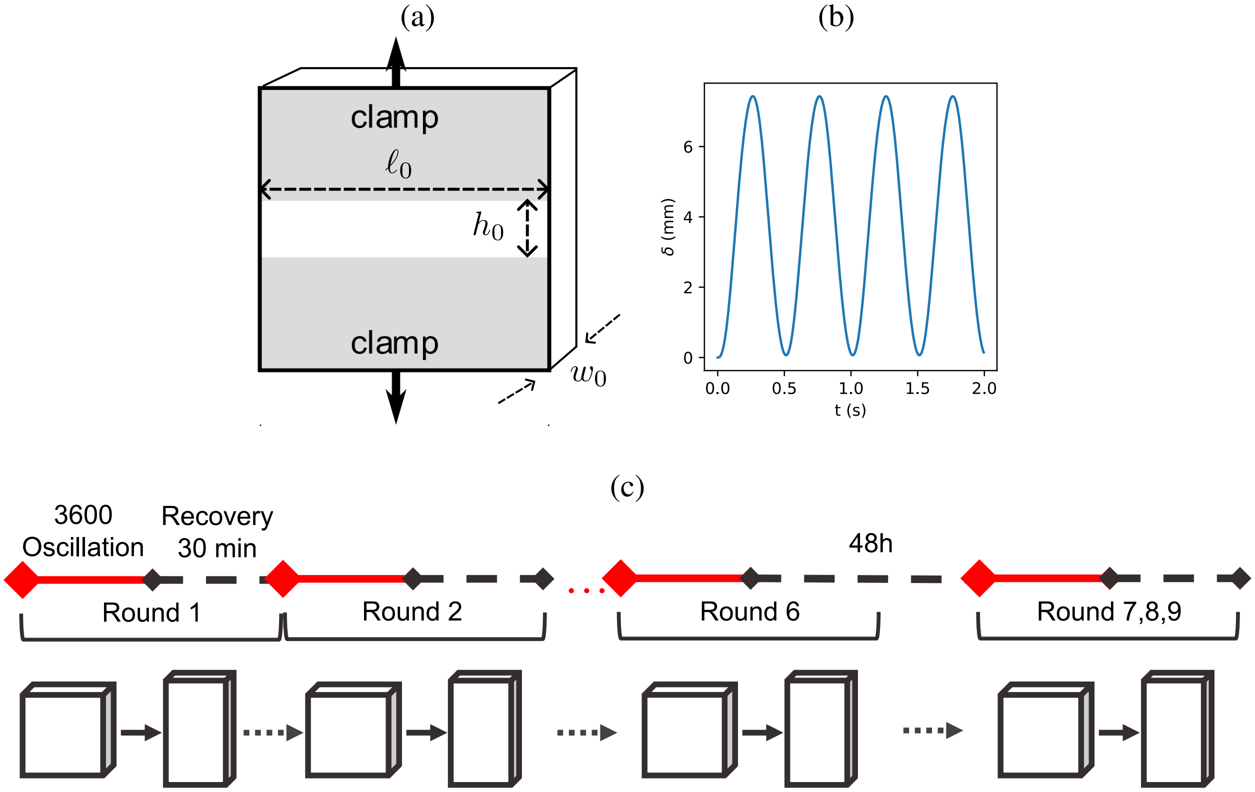

Figure 5.1: Experimental setup for the pure shear fatigue damage tests (a), displacement-controlled loading profile (b) and the total 9 rounds of oscillation-rest testing procedure with the corresponding shape change due to creep behavior (c)

5.2.4 Adhesive Fatigue

Axisymmetric adhesion tests were performed with a hemispherical glass indenter with a radius of 3 mm. The glass indenter was connected to a load transducer (Honeywell, 1 kg) and a piezoelectric stepping motor (Burleigh) capable of velocities ranging from 4.0 nm/s to 2.0 mm/s. Displacement was monitored using an optical sensor (Philtec) with submicrometer sensitivity. To perform each test, the pressure-sensitive adhesives (PSAs) were applied to a thick glass slide and then placed under the indenter. A microscope (Zeiss, Axiovert 100A) was placed beneath the setup to provide optical imaging of the adhesion process. The precise control of motor movement and the acquisition of data were achieved through a computer program written in MATLAB[31].

5.2.4.1 Probe-Tack Test

In a probe-tack test, the hemispherical indenter was brought into contact to the PSA at 1 μm/s moving speed in compression at ~ 25mN to ensure a consistent contact area. After a fixed dwell time, the indenter was lifted up at different strain rates to measure the detaching behavior from the PSA surface. Throughout the experiment, the force, displacement, contact area and debonding morphologies are captured in real-time. Figure 5.2shows the schematic and the corresponding force-displacement behavior at each step during the probe tack test. Different strain rates were applied ($\dot{\varepsilon} = 0.01$, 0.05 0.1, 0.5, 1.0 s^{-1}) to observe the strain-rate dependencies of the two PSAs, where the strain rate $\dot{\varepsilon} = v/h$, the quotient of the probe rate v and the film thickness h.

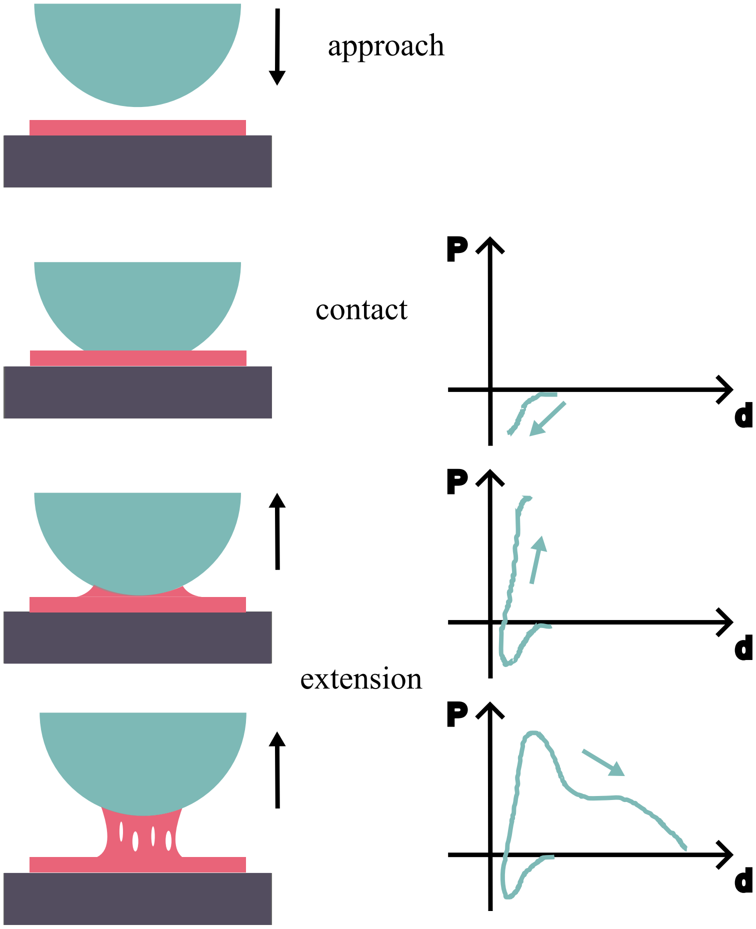

Figure 5.2: Experimental setup, procedure and the corresponding load-displacement profile for the probe tests.

5.2.4.2 Large-Strain Cyclic Adhesion Test

To investigate the stability and reliability of the PSAs under large cyclic strains, two types of cyclic adhesion tests were performed: the repeated probe test and the triangular wave test. During a repeated probe test, the same probe-tack test described above was performed 10 times at the same location on the adhesive surface. In each repetition, the strain rate was kept constant at 0.5 s^{-1} and the indenter was lifted up until fully detached from the surface. The purpose of the repeated probe test was to simulate potential debonding process of PSA during practical usage, and the change in total work of adhesive was tracked over multiple repetitions. For the triangular wave test, the indenter was first indented on the PSA surface to a maximum compressive force of ~ 25 mN, then oscillated at a slower strain rate (0.5 s^{-1}) with increasing strain amplitude. The oscillation was stopped until the debonding process was fully complete.

5.3 Results and Discussion

5.3.1 Dynamic Mechanical Analysis (DMA)

The dynamic mechanical analysis (DMA) data for both PSAs were obtained over a range of temperatures at frequencies from 0.01 Hz to 15 Hz . Master curves for the magnitude of the complex modulus (part a) and phase angle (part b) are shown in Figure 5.3, using 25 °C as the reference temperature. T_{ref}. No vertical shifts of the data were applied and the frequency shift factors used to shift the data are plotted in Figure 5.3(c). The glass transition temperature T_g is operationally defined as the temperature where ϕ is maximized at a frequency of 1 Hz. In this way we obtain T_g=-45°C for CEF35 and $T_g = -10$°C for CEF05. As depicted in Figure 5.3(c), the shift factors along with their corresponding temperatures can be adapted to fit the Vogel-Fulcher-Tammann (VFT) relation, which is expressed by Equation 8.2.

$$\ln(a_T) = -\frac{B}{T_{ref} - T_\infty} + \frac{B}{T - T_\infty} \tag{5.1}$$

Table 8.1 lists the values of T_∞ and B for each PSA under consideration.

Table 5.1: VFT parameters for the PSA samples.

	B (K)	T_∞ (°C)	T_g (°C)
CEF35	2282	-123	-45
CEF05	4597	-130	-10

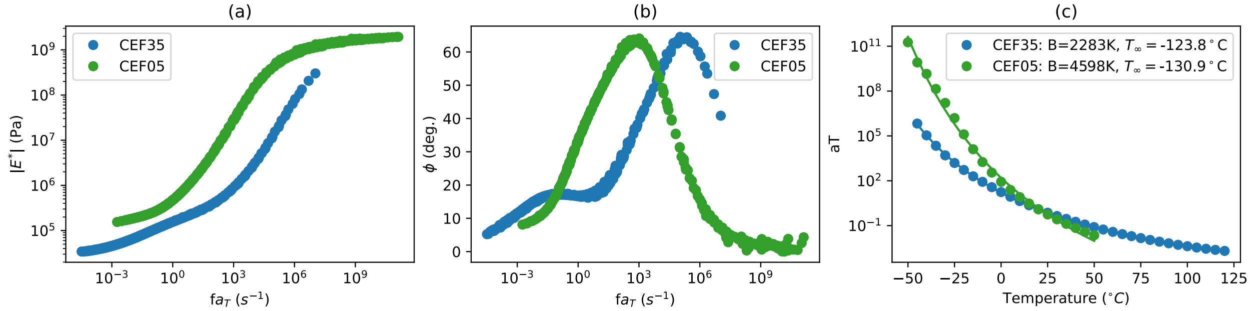

Figure 5.3: DMA master curves at 25 °C showing the complex modulus $|E^*|$ (a) and phase angle (ϕ) as a function of reduced frequency.

5.3.2 Bulk Fatigue

5.3.2.1 Stress-Strain Curves and Creep

The stress-strain relationships can be analyzed by subjecting the two PSA samples to strain-controlled cyclic loading. Figure 5.4 shows the the evolution of the full hysteresis loop for both samples over a single round of 3600 cycles, where the maximum nominal strain for each cycle is 1.5. The CEF35 samples are relatively soft, reaching a maximum stress of ≈0.1MPa. the CEF05 samples are stiffer, with a peak stress of ≈0.25 MPa. Notably, both samples show significant strain softening and creep behavior throughout the 3600 cycles in a single round of cyclic testing. As the PSAs are unfilled, there are no filler-matrix interactions, and the creep originates solely from the chain extension and molecular rearrangement of the lightly crosslinked PSAs. This leads to the deformation and elongation of the test specimens.

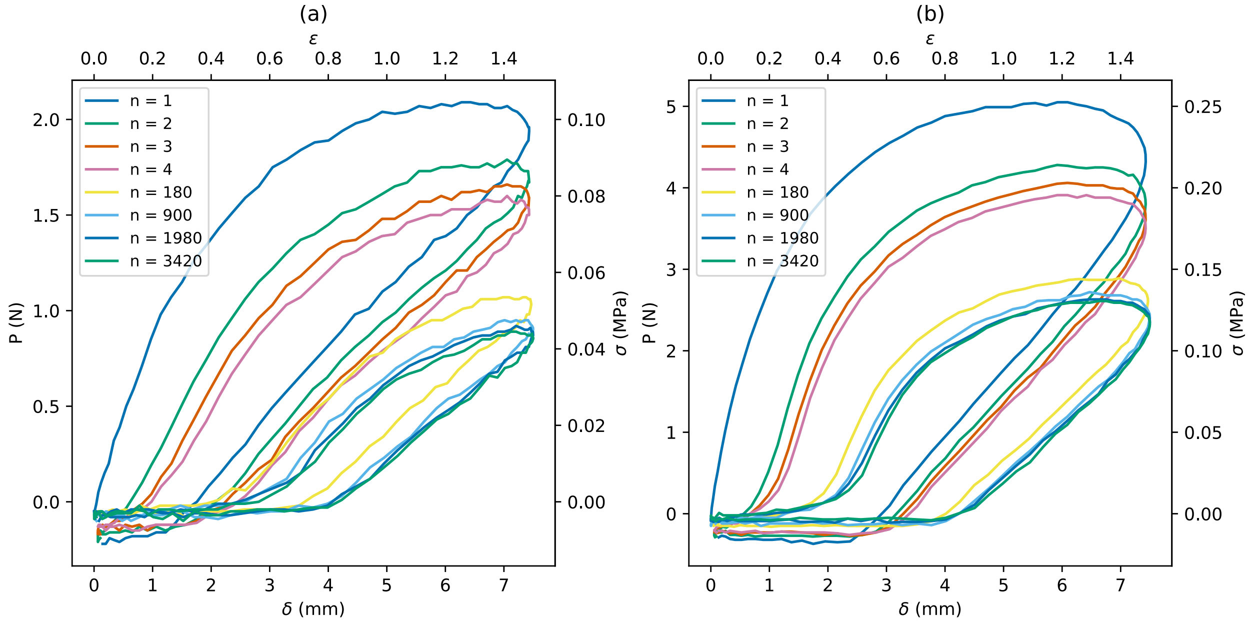

Figure 5.4: Full hysteresis loop depicting the stress-strain relationship change during one round (3600 cycles) for CEF35 (a) and CEF05 (b).

We define a creep strain, ε_0, as the strain that must be subtracted from the actual applied strain in order to superpose the loading portions of the stress/strain curves obtained during successive oscillations. This creep strain is plotted as a function of cycle number for a given round of oscillations in Figure 5.5. The creep saturates after about 200 cycles, with about half of this creep occurring in the first four cycles. Also, note that the stresses in Figure 5.4 are nominal stresses, defined by dividing the measured load by the undeformed cross sectional area, A_0:

$$\sigma = \frac{P}{A_0} = \frac{P}{\ell_0 w_0} \tag{5.2}$$

The stress/strain curves for subsequent oscillations are obtained by shifting the origin of the strain axis by the creep strain as described above, while also accounting for the change in the cross-sectional area of the sample (which is assumed to be incompressible) as a result of the creep:

$$\sigma = \frac{P}{h_0 \cdot l_0}\left(1 + \varepsilon_{\text{creep}}\right) \tag{5.3}$$

Figure 5.6 shows that the stress/strain curves obtained in this way are relatively consistent throughout one round of testing, with little change in the calculated modulus.

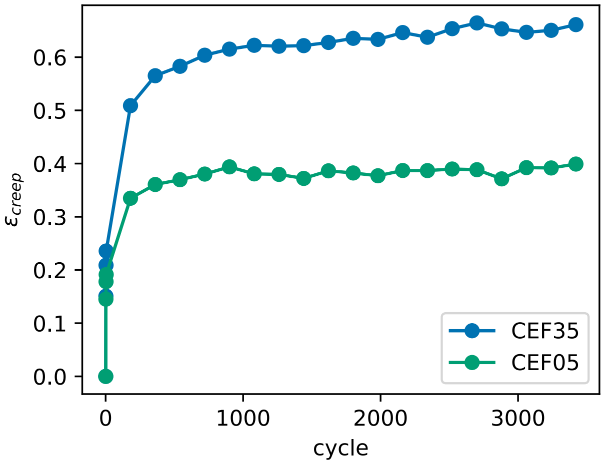

Figure 5.5: Creep strain as a function of cycle number during a given round of oscillations at 2 Hz.

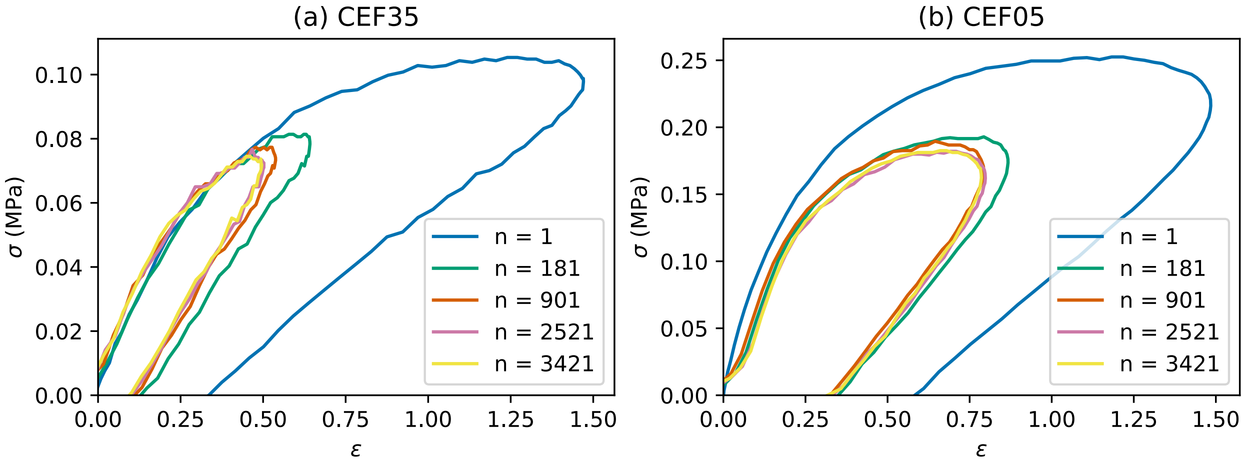

Figure 5.6: The stress-strain curves after removing the creep effect for CEF35 (a) and CEF05 (b) during a single round of oscillations.

The creep that takes place during one round of oscillations at 2 Hz is completely recovered during the 30 minute relaxation time between subsequent rounds of testing. As a result, no creep strain is needed in order to superpose the curves obtained for the first oscillation in each round. We use complex modulus $|E^*|$ to characterize the sample viscoelasticity instead of simply using the traditional stress-strain slope at small strain regime, due to the fact that the viscous dissipation (or the loss modulus, E''), is more significant and is non-negligible in lightly crosslinked PSAs. The complex modulus is defined using $|E^*| = \sigma_{max}/\varepsilon_{max}$, where σ_{max} and ε_{max} corresponds to the maximum stress and strain response from the first oscillation in each round. The change of complex moduli is illustrated in Figure 5.8. We observe that the complex moduli remains relatively stable during different rounds. For the both samples, the complex moduli decrease by a minimal amount after six rounds of testing, both with in 5% range. Although the samples were able to return to their original shape within 30 minutes, the softening effect persisted for longer times. After 48 hours of relaxation (between rounds 6-7) the complex moduli of CEF35 samples reached higher moduli, showing a permanent stiffening effect. Meanwhile, CEF05 continued to decrease after round 7, suggesting a small degree of damage. Both PSA samples demonstrated favorable properties maintaining the material shape and mechanical response. The strain sweep data for both samples are presented in Figure 5.9, where the small strain complex moduli obtained from DMA are combined with the large strain moduli acquired through pure shear oscillation tests. The results demonstrate a good agreement between the small and large strain data, with the large strain data aligning well with the extrapolated line of the small strain linear regime. This confirms the reliability of the pure shear geometry oscillation test.

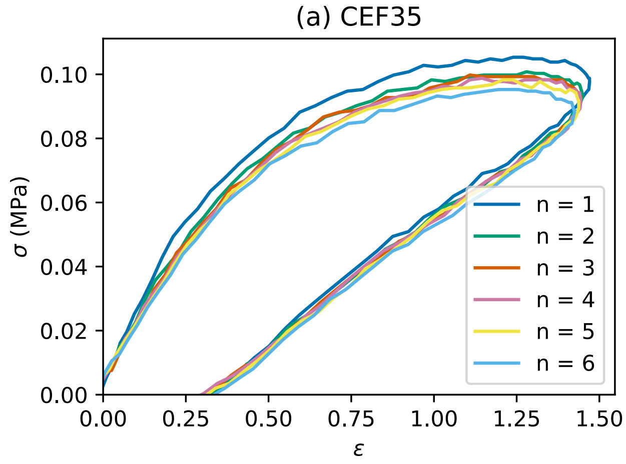

Figure 5.7: The hysteresis loops of CEF35 (a) and CEF05 (b) of the first cycle in the first 6 rounds of tests.

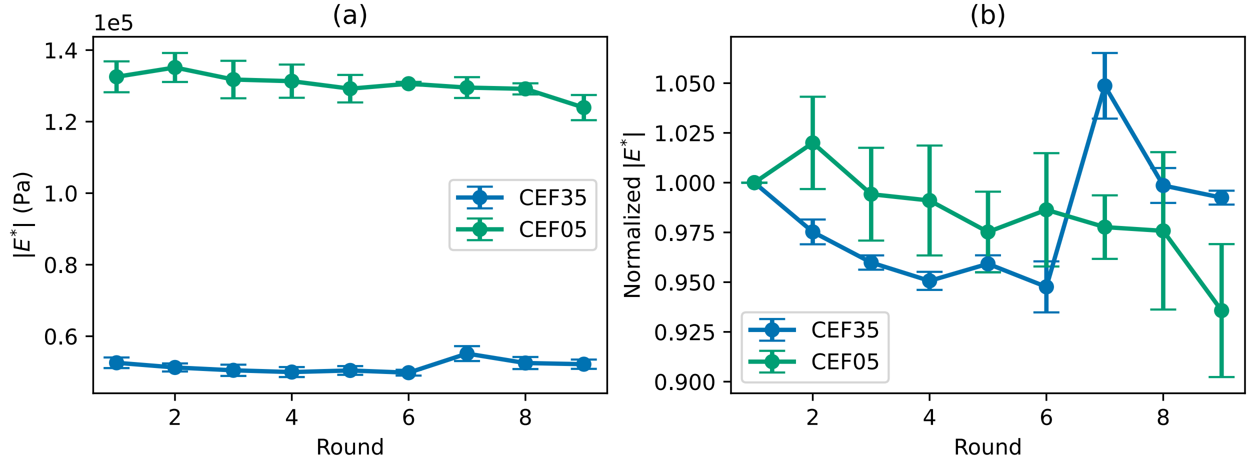

Figure 5.8: Changes in complex modulus over different rounds for CEF35 and CEF05 (a). A 48-hour relaxation period is applied between rounds 6 and 7, as shown in Figure 5.1(c).

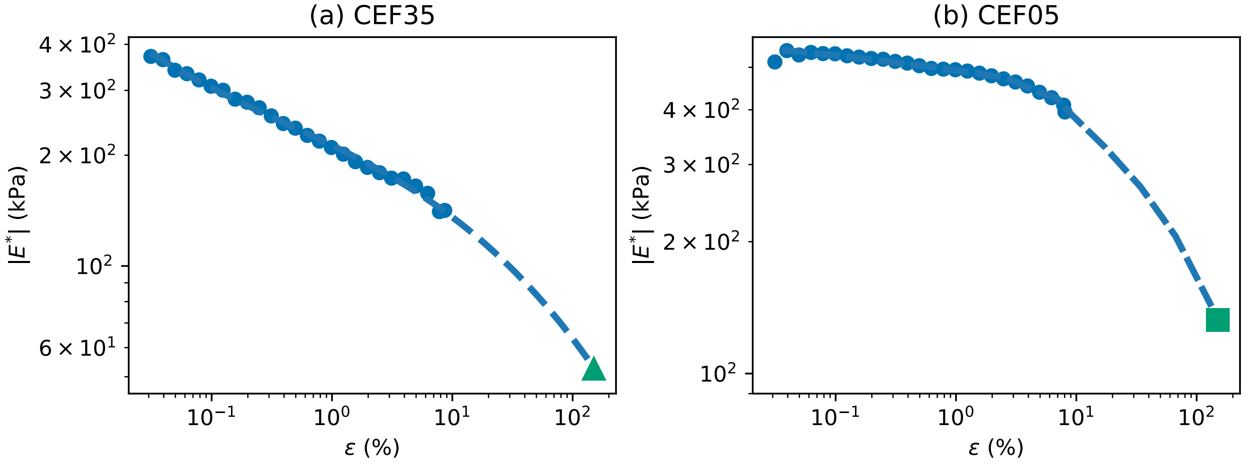

Figure 5.9: Strain sweep data for CEF35 (a) and CEF05 (b). The complex modulus obtained from the large-strain pure shear geometry is shown as green triangle ▲ for CEF35 and square ■ for CEF05.

5.3.2.2 Viscoelastic Dissipation

The viscoelastic dissipation can be quantified using the calculation of an effective phase angle, ϕ_{eff}, from the load-displacement response. The value of ϕ_{eff} can be obtained by using the following equation[33, 61] applied to the first cycle in each round, where the minimum values of the stress and strain are zero and the maximum values are σ_{max} and ε_{max}:

$$\sin\phi_{eff} = \frac{4\int \sigma d\varepsilon}{\pi\sigma_{max}\varepsilon_{max}} \tag{5.4}$$

This method of determining the phase angle offers a relatable approach for quantifying large strain energy dissipation, enabling connections and comparisons with the small strain data obtained from DMA tests, where the stresses and strains are both sinusoidal. Note that ϕ_{eff} reduces to the usual viscoelastic phase angle describing the phase lag between stress and strain in this limit of linear response. The effective phase angle defined in Equation 5.4 provides a generalization that allows us to operationally define a phase angle in the nonlinear regime where the stress and/or strain are not ideally sinusoidal. Figure 5.10(a) shows the evolution of the effective phase angles obtained from the first cycle of each round. For both materials ϕ_{eff} increases by 15 - 20% after the first round of testing (see Figure 5.10(b)). After 48 hours, both PSAs regain their original viscoelastic response, suggesting that back to their original ϕ_{eff}, suggesting that the changes are temporary and reversible. The values of ϕ_{eff} in Figure 5.10 are consistent with the DMA data shown in Figure 5.3 (a), which indicates that the two PSAs show general viscoelastic properties that behave similarly under both linear viscoelastic regime and large strain nonlinear regime.

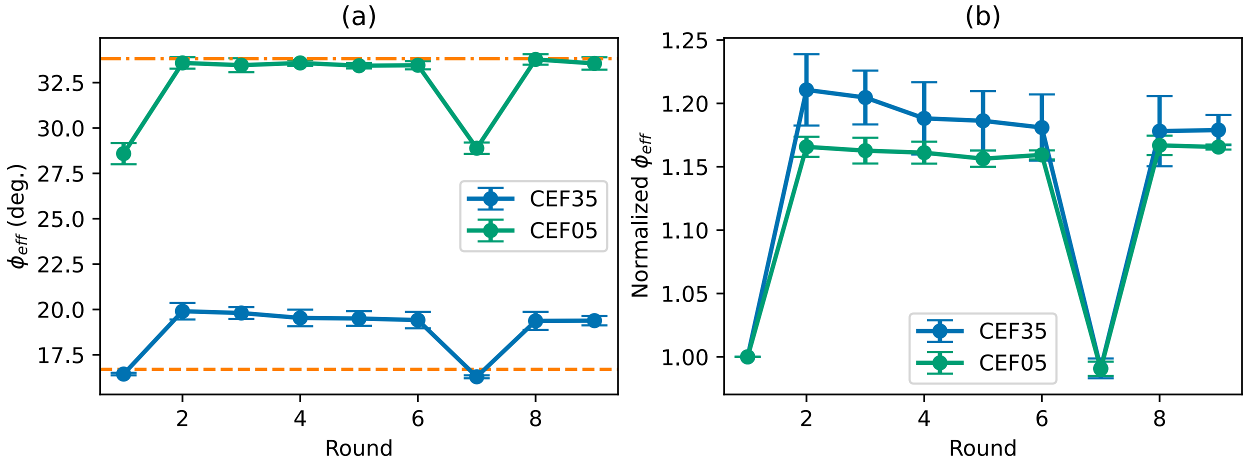

Figure 5.10: Calculated ϕ_{eff} of CEF35 and CEF05 (a) and their normalized values (b) of the first cycle in each round. The orange line in (a) shows DMA-measured value of ϕ_{eff} for CEF35 (16.7°, orange dashed lines) and for CEF05 (33.8°, orange dash-dot lines).

5.3.3 Adhesive Fatigue

5.3.3.1 Work of Adhesion

The work of adhesion can also be obtained from the measured relationship between the stress and strain during a probe tack test. Here the average stress and strain are defined as $\sigma = P/\pi a_{max}^2$ and $\varepsilon = \delta/h$ respectively, where P is the load, a_{max} is the maximum contact radius between the indenter and the surface, δ is the displacement and h is the adhesive thickness. The work of adhesion, W_{adh}, is obtained from the integral of the tack curve, and is a measure of the total energy required separate the probe from the adhesive layer [26, 27, 31]:

$$W_{adh} = \frac{1}{\pi a_{max}^2} \int P d\delta = h \int \sigma d\varepsilon \tag{5.5}$$

Figure 5.11 shows tack curves for the two samples at different strain rates, and the values of W_{adh} are included in Table 5.2. Wang *et al.* and Crosby *et al.* [26, 27, 31] discussed the shape and corresponding characteristic points of a typical tack curve, identifying the three crucial parameters (shown in Figure 5.11(c)): σ_{max}, representing the maximum tensile load where fingering/cavitation starts [28, 29, 31]; ε_f the failure strain at which the PSA completely detaches from the indenter; $\sigma_{plateau}$, the load on the shoulder at which the actual contact area starts to decrease towards a complete detachment. Among the three parameters, the first two can be readily identified from the tack curves, while $\sigma_{plateau}$ is less well-defined and depends more on an empirical observation.

The maximum stress, σ_{max} for the probe tack test is closely coupled to the modulus of the adhesive at the appropriate strain rate. In this case the relevant modulus is evaluated at a reduced frequency from the DMA master curve. This coupling explains the rate dependence of W_{adh} and the differences between the two adhesives. The magnitude of the complex modulus, $|E^*|$, increases with increasing strain rate as shown in Table 5.2, where $\sigma_{max} \approx 1.9|E^*|$ at the appropriate frequency for both samples. By normalizing W_{adh} by the product of σ_{max} and sample thickness, h, we obtain a characteristic strain, ε_c:

$$\varepsilon_c = \frac{W_{adh}}{\sigma_{max} h} \tag{5.6}$$

This characteristic strain is closely correlated with the maximum strain applied to the adhesive prior to failure, as illustrated schematically in Figure 5.11(c). We observe a gradual increase in W_{adh} and ε_c with increasing $\dot{\varepsilon}$ for both materials. CEF35 generally exhibits a higher value of ε_c than CEF05, indicating a stronger attachment to the glass surface. The evolution of the adhesive morphology during the full detachment process for the two adhesive is shown in Figure 5.12. Note that the plateau stress can be defined operationally as the stress at ε_c, removing any ambiguity in the definition of this quantity.

	CEF35					CEF05				
$\dot{\varepsilon}$ (s^{-1})	σ_{max} (kPa)	$\lvert E^*(\dot{\varepsilon})\rvert$ (kPa)	$\frac{\sigma_{max}}{\lvert E^*\rvert}$	W_{adh} (J/m^2)	ε_c	σ_{max} (kPa)	$\lvert E^*(\dot{\varepsilon})\rvert$ (kPa)	$\frac{\sigma_{max}}{\lvert E^*\rvert}$	W_{adh} (J/m^2)	ε_c
0.01	131	65.6	2.00	11.4	1.74	349	183	1.91	13.7	0.79
0.05	163	88.5	1.84	12.7	1.56	419	221	1.90	21.8	1.04
0.1	192	103	1.86	19.7	2.10	492	250	1.97	31.7	1.29
0.5	252	137	1.87	31.4	2.49	734	371	1.98	66.2	1.80
1	285	155	1.84	38.7	2.72	894	474	1.89	97.5	2.18

Table 5.2: The change of probe tack test parameters ($\lvert E^*\rvert$,W_{adh}) coupled to the maximum stress (σ_{max}) at different strain rate ($\dot{\varepsilon}$).

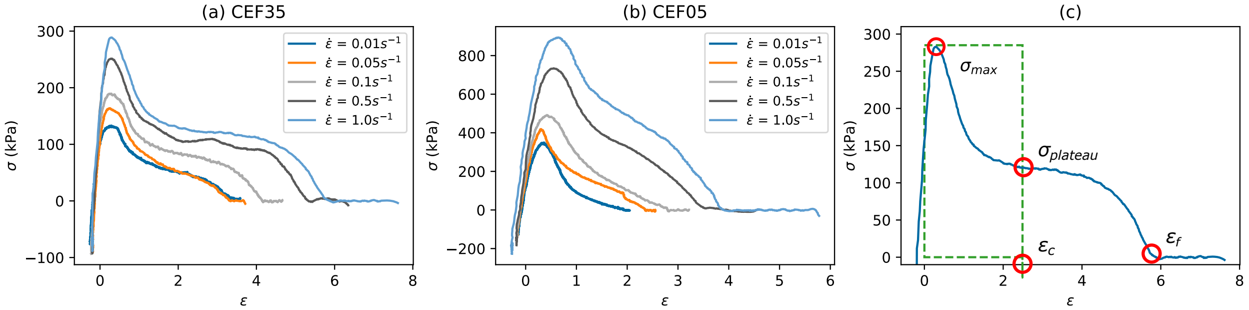

Figure 5.11: Probe tack curves of CEF35 (a) and CEF05 (b) under different strain rate. (c): A typical probe tack curve with the green dashed box highlighting the equivalent work of adhesion W_{adh} at maximum stress (σ_{max}) and characteristic strain. By definition, $\varepsilon_c = W_{adh}/(E^*h)$.

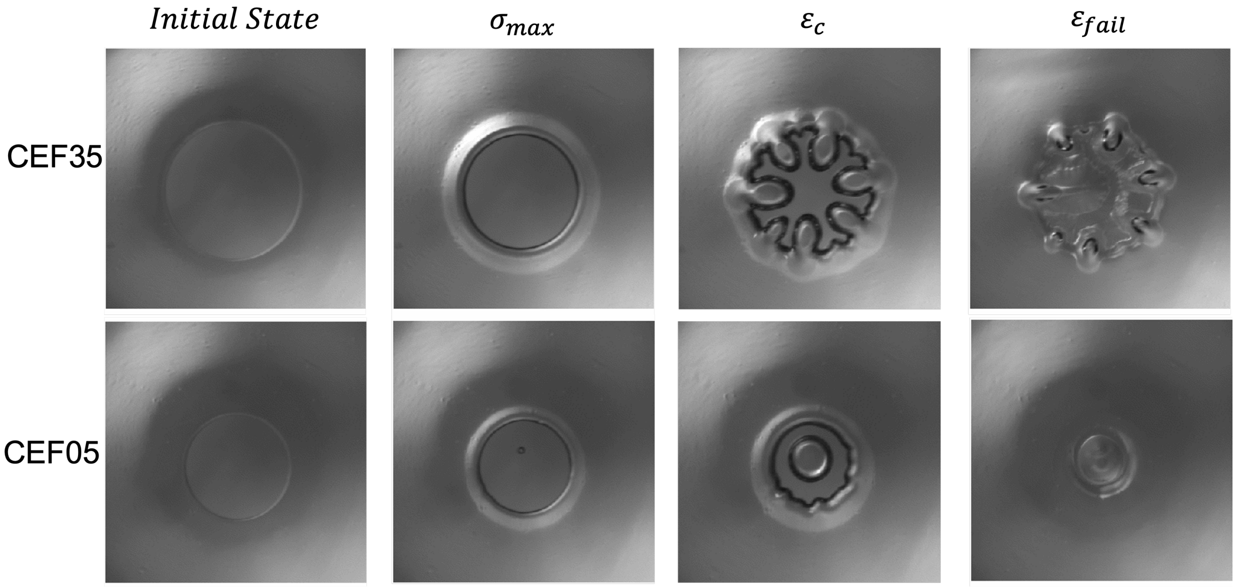

Figure 5.12: Microscope observations of a detachment for CEF35 (first row) and CEF05 (second row).

5.3.3.2 Repeated Detachment Behavior

Repeated probe tack tests are helpful for understanding and predicting the performances of PSAs under real-world applications. As in practical applications are subjected to repeated loading, which may result in fatigue and degradation in other mechanical properties of PSAs over time. In the repeated probe tests the tack behavior was investigated by performing the simple probe test repeatedly onto the same spot of the PSA surface and comparing the resultant tack curves. The result for the ten repeated probe tack tests for each adhesive are shown in Figure 5.13. The strain rate was controlled at $\dot{\varepsilon} = 0.5s^{-1}$ in these experiments.

As can be seen in Figure 5.14(a) that the values of W_{adh} attain their maximized value of $\approx 38\ J/m^2$ for CEF35 and $\approx 74\ J/m^2$ for CEF05 for the first cycle, decreaing throughout the subsequent test cycles. To help visualize the extent of decay, Figure 5.14 (b) shows values of W_{adh} for the two PSAs normalized by their first cycle values. Starting from the third repeat, the work of adhesion reaches for CEF05 reaches a plateau of about 60% of its original value. In contrast to this, the work of adhesion for the softer CEF35 adhesive continues to decrease, reaching 20% of its original value after ten cycles. The effect of the cycling on the value of σ_{max} is relatively small in both cases. The main effect of the cycling is to reduce strain at which adhesive failure occurs, with failure occurring at strains of 1.5-2 after ten cycles for both adhesives. For the softer adhesive a relatively large fraction of the initial work of adhesion corresponds to the large-strain region of the tack curve. Because this large-strain behavior is more susceptible to repeated cycling than the low-strain behavior in the vicinity of σ_{max}, the fractional decrease in adhesion during repeated cycling is larger for the softer sample.

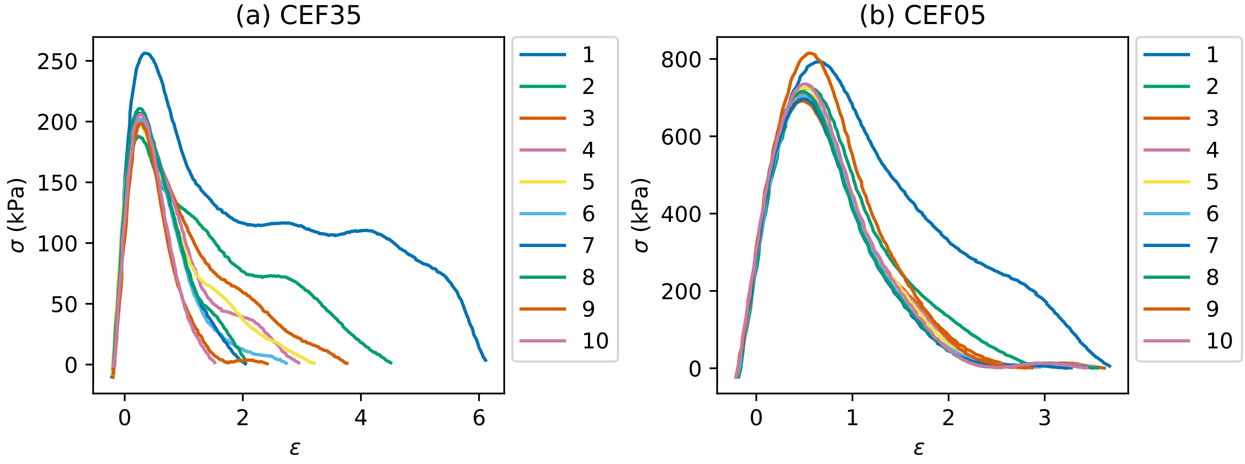

Figure 5.13: Repeated probe tack tests for CEF35 (a) and CEF05 (b) at a strain rate of 0.5 s^{-1}.

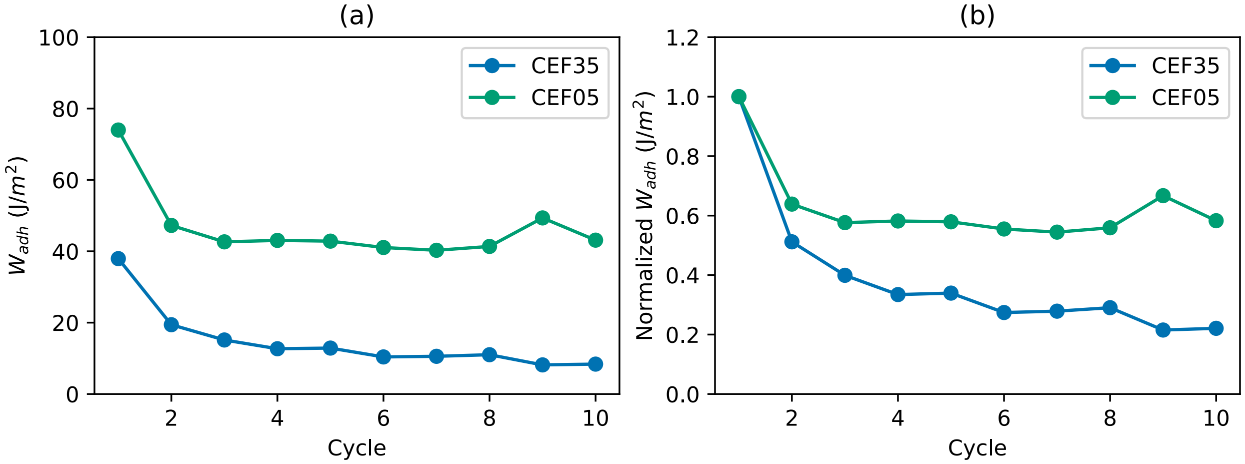

Figure 5.14: Decreasing trend of work of adhesion W_{adh} (a) and normalized W_{adh} (b) over 10 cycles of repeat in a repeated probe tack test. Tests were conducted at a strain rate of 0.5 s^{-1}.

5.3.3.3 Incremental Tack Curves

The energy dissipation condition can be characterized by collecting a series of incremental tack curves, where triangular wave oscillations with increasing strain amplitudes are applied to the sample. The result is a series of tack curves obtained from the same portion of the sample but at different maximum strains, as shown in Figure 5.15[31]. The probe is indented onto the PSA surface to reach a specific compression force, similar to a typical probe tack test, and then lifted and oscillated with increasing wave amplitudes until the indenter is completely detached from the surface. The total energy expended during the loading portion of a single cycle of oscillation is separated into a dissipative component, Γ, which represents the bulk energy dissipated, and a stored component, $\mathscr{G}$, which is available to drive detachment of the indenter from the adhesive. A schematic representation of the calculation of Γ and $\mathscr{G}$ from a single oscillation is shown in Figure5.15 (c). The dissipative component Γ is calculated by multiplying the PSA thickness (h) by the integrated area between the loading and unloading curves for a given cycle. The elastic component, $\mathscr{G}$, is calculated using the same method but utilizing the area under the unloading portion of the curve.

Figure 5.15 shows the incremental tack curves for both PSAs. In the absence of interfacial fatigue, the envelope of the full set of incremental tack curves is roughly equivalent to the the initial tack curves, shown as the dashed lines in Figure 5.15 (a, b). The incremental tack curve protocol allows us to extract dissipated and stored energy as a function of strain. These quantities are plotted in Figures 5.16 (a) and (b) for both adhesives. The dissipative component, Γ, increases monotonically with increasing strain, reaching a value equal to W_{adh} for the last tack curve, where the indenter is completely removed from the adhesive. Interfacial fatigue causes this value of W_{adh} to be less than the value obtained from non-incremental test, where the indenter is completely separated from the adhesive during the first cycle.

Our interpretation of $\mathscr{G}$ is that it represents the driving force for adhesive failure at the indenter/adhesive interface. The observed maximum in $\mathscr{G}$ shown in Figure 5.16 is an artifact arising from the fact that the actual contact area is starting to decrease for strains above some critical value. For our materials we find that this critical strain is roughly equal to the characteristic strain, ε_c, defined in Figure 5.11 and listed in table 5.2. As a result of this decreased contact area the ’true’ stress (load divided by the actual contact area) is larger than the ’engineering’ stress (load divided by maximum contact area). Using the engineering stress instead of the true stress in our definition of $\mathscr{G}$ underestimates the actual driving force for adhesive failure, giving rise to the observed maximum of $\mathscr{G}_c$ for $\mathscr{G}$. Cross plots of Γ and $\mathscr{G}$, shown for our materials in Figure 5.16 (c) are particularly instructive. For $\mathscr{G} < \mathscr{G}_{\mathrm{c}}$, $\mathscr{G} \approx \Gamma$ and the plot of Γ vs $\mathscr{G}$ is a straight line with a slope of $\approx$1. In this low-strain region of the sample, the actual indenter/adhesive contact area is fixed. We use $\mathscr{G}_c$ as a measure of the adhesive strength of the interface, so that adhesive failure begins when $\mathscr{G} \approx \mathscr{G}_c$. Because of the viscoelastic nature of the adhesives, the adhesive doesn’t immediately fail at this point. Instead, some additional extension of the adhesive occurs for larger strains, giving a value for Γ (and hence W_{adh}) at the point of failure that is approximately 3 times larger than Γ_c.

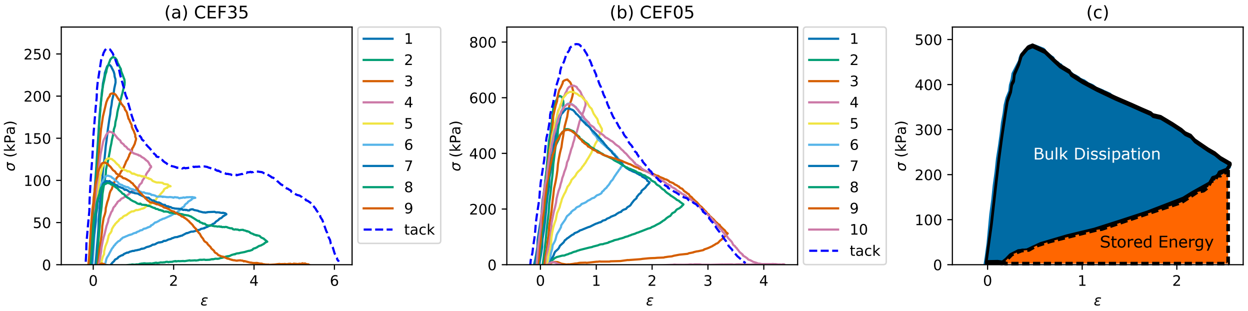

Figure 5.15: Triangular wave oscillation tack curves for CEF35 (a) and CEF05 (b) conducted at a strain rate of 0.5 s^{-1}. (c) shows the schematic illustration of the stored and dissipated energy: Dissipated energy (Γ) and Stored energy ($\mathscr{G}$), each calculated as the product of the shaded area and the sample thickness, h. The dashed lines in (a) and (b) are the full tack curves for the first cycle of the repeated tests from Figure 5.13.

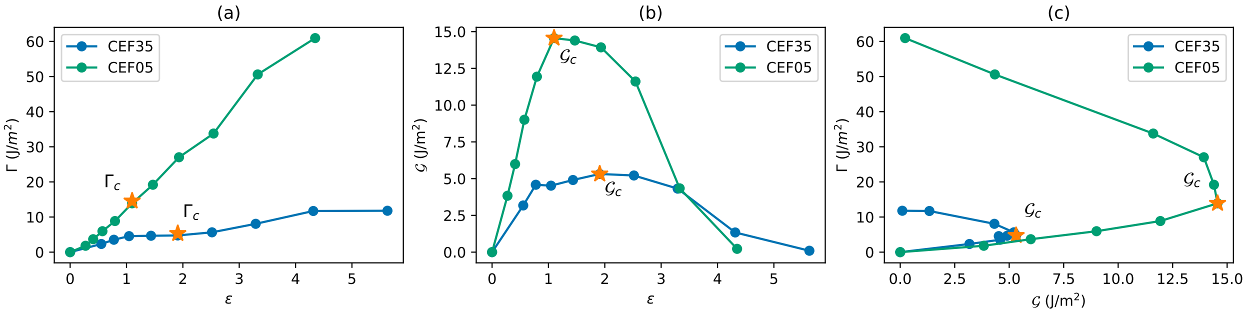

Figure 5.16: The relationship between Γ, $\mathscr{G}$ and ε. The bulk energy dissipation (Γ) increase proportionally with the strain (ε) in (a). The interfacial dissipation $\mathscr{G}$ reaches a maximum value $\mathscr{G}_c$, before it decrease due to the detachment of the adhesive surface (b). The third figure (c) shows Γ as a function of $\mathscr{G}$. The critical turning points where $\mathscr{G} \approx \mathscr{G}_c$ and $\Gamma \approx \Gamma_c$ are marked as orange stars in the plots.

5.4 Conclusion

In this study, fatigue interpretation is presented in two aspects: bulk and interfacial fatigue damage characterization, using two commercially available PSAs, 3M$^{\text{TM}}$ Contrast Enhancement Films (CEF35 and CEF05), as model systems. Both samples are lightly crosslinked acrylic PSAs, and display distinct viscoelastic property changes under pure shear fatigue damage tests and adhesive probe-tack tests. Pure shear fatigue damage tests mainly investigate energy dissipation and modulus changes over multiple loading-recovery rounds, while adhesive probe-tack tests focus on energy distribution during interfacial debonding processes, including individual and repeated detachment processes. For the pure shear fatigue cyclic test both PSAs exhibit increased dissipation and softening effects when subjected to multiple test cycles, but the properties fully recover after 48 hours of relaxation.

Adhesion tests examine energy dissipation conditions during interfacial detachment of the PSA and the surface, resembling real-life applications where PSAs fail at the adhesive/indenter interface. We have defined a characteristic strain, ε_c, which denotes the onset of contact area decrease during the debonding process. For both adhesive the maximum stress during a probe tack test was $1.9\,|E^*| \pm 0.1\,|E^*|$, where $|E^*|$ is the magnitude of the complex modulus evaluated at the appropriate frequency. Adhesive fatigue was assessed by repeating probe tack tests at the same location of the sample. The stiffer CEF05 sample was more resistant to adhesive fatigue than the softer CEF35 sample. After ten cycles the work of adhesion was reduced by 40% and 80% for the CEF05 and CEF35 samples, respectively. Additionally, W_{adh} can be further divided into bulk (Γ) and interfacial ($\mathscr{G}$) energy using the triangular wave test, where the critical stored energy $\mathscr{G}_c$ marks the onset of interfacial failure. For both PSAs, we found that the slope of Γ - $\mathscr{G}$ curve being 1 indicates an equal distribution of bulk and interfacial energy dissipation, but with a higher $\mathscr{G}_c$ for CEF05 than that CEF35. This results means that CEF05 can sustain higher energy input before the interfacial failure begins, which is consistent with the pure shear geometry bulk fatigue data.

Chapter 6

Fatigue Characterization of Triblock Copolymer-Toughened Dynamic Epoxy Network

6.1 Introduction and Background

In recent years, the integration of dynamic covalent chemistry into epoxy networks has garnered significant interest due to the self-healing properties it imparts. This advancement offers a novel approach to recycle and reprocess epoxy thermosets, enhancing their sustainability. A variety of chemistries have been employed to create dynamic networks, such as transesterification[96–98], Diels-Alder reaction[99–101], imine bonds[102–104] and disulfide bonds[105–110]. Among the numerous dynamic covalent networks applicable to epoxy resins, disulfide linkages are frequently chosen for study due to their straightforward self-healing ability upon heating, which does not require any external stimuli such as catalysts[111–113]. This self-healing ability has the potential to extend the service life of epoxy-based products while maintaining their high mechanical strength, electrical insulation and chemical resistances, which are better-suited for a wide range of applications, including adhesives, coatings, and corrosion protection. Those dynamic bonds are proved to increase the fracture toughness of samples by enhancing the bond exchange within the matrix[110].

In addition to incorporating dynamic bonds to strengthen the inherently brittle epoxy matrix, various approaches can be adapted to enhance its toughness, and one of which involves the addition of fillers, such as silica[114, 115], carbon nanotubes[116–118], or graphene[118, 119], which generally improve mechanical properties and thermal stability. Elastomeric, rubbery particles incorporated into rigid epoxy matrix are also widely adopted to help increase energy dissipation and the resistance to crack propagation [120, 121]. Rubber toughened epoxy systems are widely studied to elucidate their toughening mechanisms, such as stretching, shear band formation, crazing and crack pinning[122]. Triblock copolymer (BCP), as one of the effective rubbery additives to the epoxy systems, have been found to be particularly beneficial and versatile in enhancing the material's properties. Composed of three distinct polymer blocks covalently linked in a linear sequence, triblock copolymers exhibit complex morphologies due to the diverse properties of their individual blocks, leading to unique mechanical properties. For example, the self-assembly of BCP allows the networks to organize themselves into well defined nanostructures through fine-tuning the solubility of the polymer blocks in the solvent[16, 92, 123–129]. Kishi et al. reported the occurrence of nanoscale phase separation by incorporating acrylic BCP into epoxy systems[130], and discussed multiple methods to control the nanostructures of the copolymers[130, 131]. Factors including crosslinking density, chemical structures, curing conditions, molecular weight and block copolymer content in the matrix, have been discussed to alter the nanostructures of the copolymers into spheres, micelles, lamellar or cylinders[131–137].

For the epoxy toughening approaches mentioned above, a common method of evaluation is measuring the fracture toughness of the material. The study of fracture toughness is commonly explained using Dugdale model as a specialized cohesive zone model, which considers a cohesive zone ahead of a crack tip as the energy dissipate region. This model assumes linear elastic fracture mechanics (LEFM) for glassy materials except for the small region adjacent to the crack tip, which experiences a constant cohesive stress σ_c and leads to plastic yielding (shown in Figure 6.1 (a)). The cohesive traction results in crack opening displacement δ_t. This parameter corresponds to the mode I critical energy release rate $\mathscr{G}_{Ic}$, which is the required energy to create new surface during fracture:

$$\mathscr{G}_{Ic} = \sigma_c \delta_t = \frac{K_{Ic}^2}{E_r} \tag{6.1}$$

where σ_c is the cohesive stress, which is the amount of stress endured by the cohesive traction zone, or plastic deformation zone. The term $\mathscr{G}_{Ic}$ can also be expressed as the quotient of K_{Ic}/E_r [110, 138, 139]. The critical stress intensity factor K_{Ic} serves as a quantification of mechanical toughness, and the reduced modulus E_r, is considered in a plane strain scenario, which takes into account both the material's thickness and Poisson's ratio (v= 0.35 for glassy epoxy materials [140]):

$$E_r = \frac{E}{1 - v^2} \tag{6.2}$$

While toughness tests are adequate for evaluating the fracture behavior of an epoxy system, fatigue crack propagation tests offer a more comprehensive approach to examining the durability of the materials over an extended timescale[5, 141–144]. The effect of disulfide bond in a brittle epoxy network has been elucidated by Lewis et al. [110]that increasing concentration of disulfide bonds gradually improves the toughness due to the growing cohesive deformation zone ahead of the crack tip. Since the crack propagation speed is controlled in a fatigue test, it provides longer reaction time for disulfide bond exchange within the epoxy matrix. Therefore, fatigue tests offer a better observation technique for the examination of dynamic covalent bond activation compared to toughness tests.e for disulfide bond exchanges within the epoxy matrix. As a result, fatigue crack propagation tests present a better observation technique for examining the activation of dynamic covalent bonds compared to toughness tests.

In this study, an ABA triblock copolymer is integrated into an disulfide-containing epoxy network to enhance the toughness of the epoxy matrix. To investigate the influence of both the dynamic disulfide bond and the rubber filler, fatigue crack propagation tests were designed utilizing a flexural 3-point-bending geometry. This experimental approach enables a thorough examination of the interaction between theBCP and the epoxy network, while also shedding light on the potential improvements in material properties resulting from this incorporation.

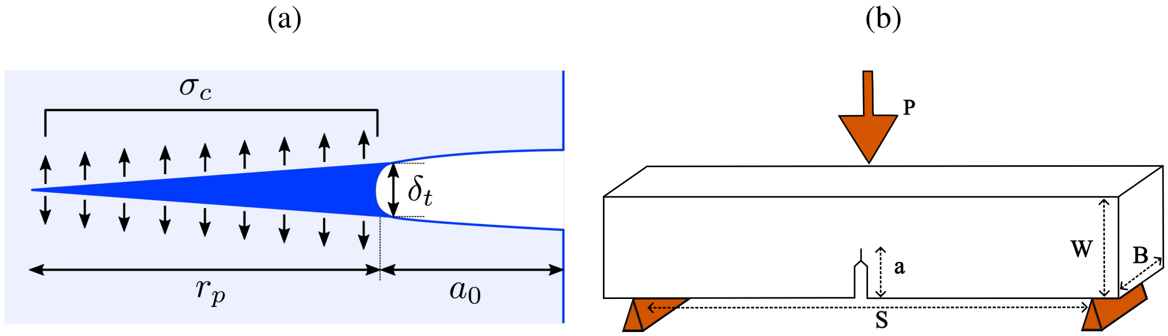

Figure 6.1: Schematic representation of the Dugdale model.(a) and illustration of a sample using single-edge-notch bending (SENB) geometry for both toughness tests and fatigue tests (b).

6.2 Materials and Methods

6.2.1 Sample Preparation

For the filler, PMMA-PnBA-PMMA triblock copolymer (BCP) LA2650 were provided by Kuraray Co. and were used as received. The total molecular wight of LA 2650 is 88,700 g/mol. The weight fraction of the endblock PMMA was 0.3 with a molecular weight of 25,000 g/mol. The midblock PnBA had a molecular weight of 116,000 g/mol. For the epoxy matrix, the bisphenol-A-based diepoxide resin, Diglycidyl ether of bisphenol A (DGEBA, Fisher Scientific), the aromatic diamine crosslinker 4,4´-Methylenebis(cyclohexylamine) (PACM, TCI Chemicals) and 4,4´-Dithiodianiline (DTDA, Oakwood Chemical) were used as received. To make the triblock copolymer–filled epoxy matrix, corresponding amount of triblock copolymer was added into the diepoxide resin (DGEBA). The mixture was heated and stirred at 150°C until the the copolymer was fully dissolved. Then the mixture was cooled down to 95°C and mixed with DTDA (melted at 95°C). Subsequently, the mixture was placed in a vacuum oven, degased in a silicone mold and cured in a Nitrogen gas (N_2) environment, precured at 110°C for 30 minutes and cured at 160°C for 8 hours. The experimental procedure is illustrated in Figure 6.2.

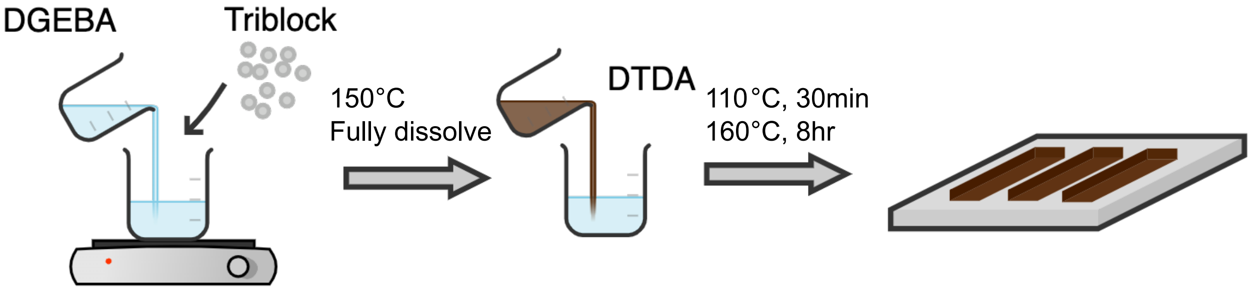

Figure 6.2: Procedure for triblock copolymer-filled epoxy matrix crosslinked with DTDA diamine crosslinker .

6.2.2 Dynamic Mechanical Analysis (DMA)

The viscoelastic behavior of the cured epoxy systems were studied using a dynamic mechanical analyzer (TA instruments RSA III Dynamic Mechanical Analyzer, New Castle, DE). Samples were prepared by cutting and polishing them into rectangular strips with dimensions of approximately $\sim$1 mm $\times$3 mm $\times$30 mm. These strips were then subjected to temperature sweep oscillatory tests in a tensile geometry, conducted over a range $-120\,^{\circ}$C to $225\,^{\circ}$C with increments of $2.5\,^{\circ}$C. The strain amplitude was 0.1% and the samples were soaked for 60 seconds before the measurement.

6.2.3 Atomic Force Microscopy (AFM)

For the atomic force microscopy image, a Bruker Dimension Icon AFM was used in PeakForce Tapping mode. Using an ACTA-W cantilever from AppNano, the deflection sensitivity was determined using a silicon wafer, and a spring constant of 42 N/m was determined by thermal tuning. Blind tip reconstruction on an RS-12M sample from Bruker was used to measure a tip radius of 8 nm. The image was acquired with a PeakForce set-point of 20 nN, a gain of 5, an amplitude of 50 nm, and an oscillation frequency of 1 kHz. These parameters provided an indentation depth of approximately 2 nm. NanoScope Analysis was used to analyze force curves and export images. To extract modulus data, the unload region of each force curve was fitted to 5-80% of the maximum force and fit to the Derjaguin-Muller-Toporov (DMT) model[145].

6.2.4 Fracture Toughness Test

The fracture toughness was characterized using ASTM D5045 standard using single-edge-notch bending (SENB) geometry. The 3-point-bending tests were performed using an ElectroForce linear motor (200 N load cell) from TA instrument with a span (S) of 40 mm. The samples were molded with a notch, and generally had a depth (W) of ∼10 mm, length (L) of 45 mm and thickness (B) between 3 to 5 mm. The span-to-depth ratio of the experimental setting is $\beta = 4$. A sharp crack was created by inserting a fresh razor blade into the molded notch and tapping it gently with a hammer. The total precrack length (a) was controlled in a range of $0.45 < \alpha < 0.55$, where the crack-to-depth ratio is given by $\alpha = a/W$. Figure 6.1(b) displays the experimental configuration. The precrack lengths were determined by subjecting the specimens under an Olympus OLS5000 3D confocal microscope. During the experiment, a load was applied to the other side of the notched side at a speed of 0.05 mm/s until fracture, with load and displacement information recorded throughout the process. All samples were tested in triplicate. The sample toughness, or critical stress intensity factor is calculated using Equation 6.3 and 6.4based on the maximum load P$_{max}$, sample dimension (B, W) and $f(\alpha)$, which is a general shape factor adjusted based on α:

$$K_{IC} = \frac{P_{max}}{BW^{1/2}} f(\alpha) \tag{6.3}$$

$$f(\alpha) = 6x^{1/2} \frac{[1.99 - \alpha(1-\alpha)(2.15 - 3.93\alpha + 2.7\alpha^2)]}{(1+2\alpha)(1-\alpha)^{3/2}} \tag{6.4}$$

6.2.5 Uniaxial Tensile Test

Uniaxial tensile tests were performed on dogbone-shaped samples, featuring cross-sectional dimensions of 3 mm by 8 mm. The samples were carefully polished to minimize the impact of surface flaws on the test results. A MTS Criterion universal testing frame, equipped with a 2.5 kN load cell, was used to conduct the tests. Throughout the testing process, the crosshead moved at a constant speed of 5 mm/min until the samples fractured.

6.2.6 Flexural Fatigue Crack Growth Test

Flexural fatigue crack growth tests were conducted on samples using the same SENB geometry as employed in the fracture toughness tests. The fatigue tests utilized identical experimental configurations and instruments to ensure consistency and comparability of the results. An oscillatory compression force was applied to the samples in a load-controlled manner at a frequency of 2 Hz. The minimum compression load is maintained at 2 N, and the maximum load is set to approximately at $P \approx \frac{1}{2}P_{max}$ according to Equation 6.3. The crack length is estimated according to the change of the specimen compliance C, which increases as the crack tip propagates. The total compliance can be split into two components: compliance of non-cracked flexural sample C_0 and the crack-induced compliance $C_c(\alpha)$. The relationship of the compliance parameters can be expressed as follows [146, 147]:

$$\frac{\delta}{P} = C = (C_0 + C_c(\alpha)) \tag{6.5}$$

where δ and P are the displacement and load respectively. The crack-to-depth ratio α can be then obtained by the expression:

$$\alpha = \frac{(C_c E' B)^{1/2}}{[C_c E' B + q_1(\beta)(C_c E' B)^{1/2} + q_2(\beta)(C_c E' B)^{1/3} + q_3(\beta)]^{1/2}} \tag{6.6}$$

where E' is the elastic modulus obtained from the tensile test. The expressions q_1, q_2 and q_3 are functions of the span-to-depth ratio β:

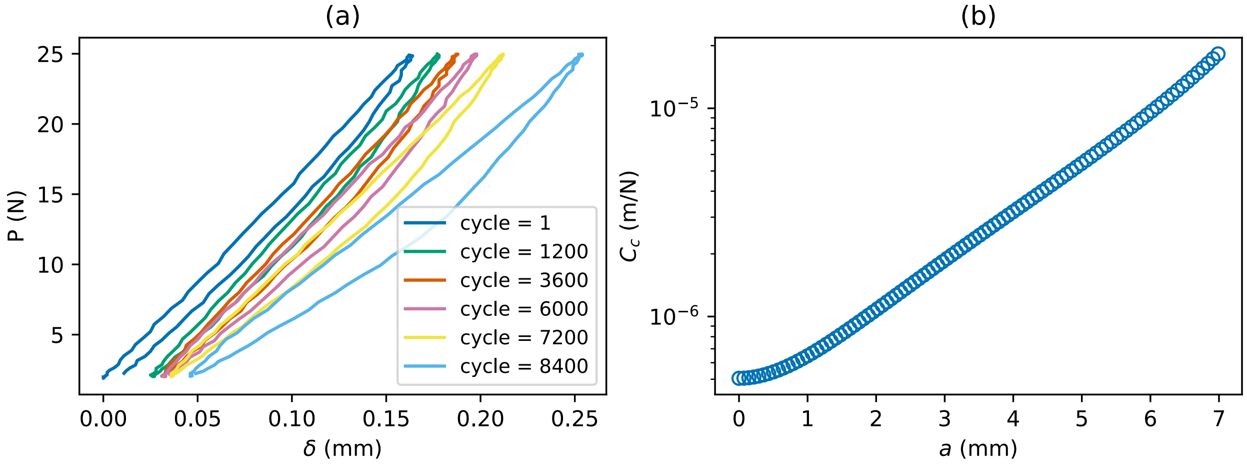

Figure 6.3: The increase in compliance during a fatigue test over 8,400 cycles (A) and the relationship between crack-induced compliance C_c and crack length (B). For a SENB sample with a sharp crack, the theoretical C_c value increases with longer crack lengths.

$$\begin{aligned} q_1(\beta) &= 0.98 + 3.77\beta \\ q_2(\beta) &= -\tfrac{9.1+2.9\beta^2}{1+0.168\beta^2} \\ q_3(\beta) &= -3.2\beta + 8.9\beta^2 \end{aligned} \tag{6.7}$$

Equation 6.6 provides the theoretical relationship between C_c and the crack length a, assuming a sample depth of W = 10 mm, which corresponds to the range of $0 < \alpha < 0.7$. As the crack becomes longer, the flexural sample will possess In actual 3-point-bending tests, α is controlled within the range of $0.45 < \alpha < 0.55$, and the critical stress intensity factor (K_{Ic}) needs to be considered, as further discussed in the "The Fatigue Failure Criterion and Fracture Toughness" section. Figure 6.3 (a) shows the compliance change during a fatigue test on 10 wt% BCP-filled epoxy matrix.The loading curve from cycle 1 to cycle 8400 shows a decreasing trend, indicating a reduction in the stiffness of the SENB sample and an increase in compliance.

6.3 Results and Discussion

6.3.1 Dynamic Mechanical Analysis (DMA)

Dynamic Mechanical Analysis (DMA) was used to investigate the thermodynamic properties of the epoxy composite. Figure 6.4 shows the temperature sweep data collected for both the unfilled DTDA epoxy matrix and the 10 wt% BCP-filled DTDA matrix. The storage modulus and glass transition temperature (T_g) of both systems as a function of temperature are shown in Figure 6.4 (a), where the unfilled epoxy matrix have a glass transition temperature at $T_g \approx 160$°C. The incorporation of rubbery filler is usually expected to decrease due to the increase of free energy introduced by the rubber chain flexibility[121]. However, in the 10 wt% BCP-filled epoxy matrix is found to have a similar T_g located at 160°C, which does not deviate from the unfilled epoxy matrix. Considering that PnBA and PMMA have T_g values of -50°C and 110°C respectively[144], both of which are lower than the T_g of the epoxy matrix (160°C), the T_g of the 10 wt% BCP-infused epoxy composite will be close to 130°C according to the Flory Fox Equation. The fact that our 10wt% BCP-filled epoxy maintains a T_g at 160°C may be attributed to an increase in crosslinks within the epoxy network. This is because the glassy PMMA segment has been reported to be partially miscible with DGEBA cured with amine-cured networks, while the middle block PnBA remains immiscible and forms nanoscale structures [130, 131, 148]. Similar results have also been reported by other researchers [144, 149]. The storage modulus $E^{'}$ is slightly lower that that of a unfilled epoxy, which is anticipated due to the inclusion of low-stiffness rubbery fillers. Figure 6.4 (b) shows the tanδ curves for the filled and unfilled system. It is shown that the loss tangent does not change by adding the block copolymer to the system, demonstrating that the incorporation of the BCP filler does not compromise the mechanical properties of the epoxy matrix.

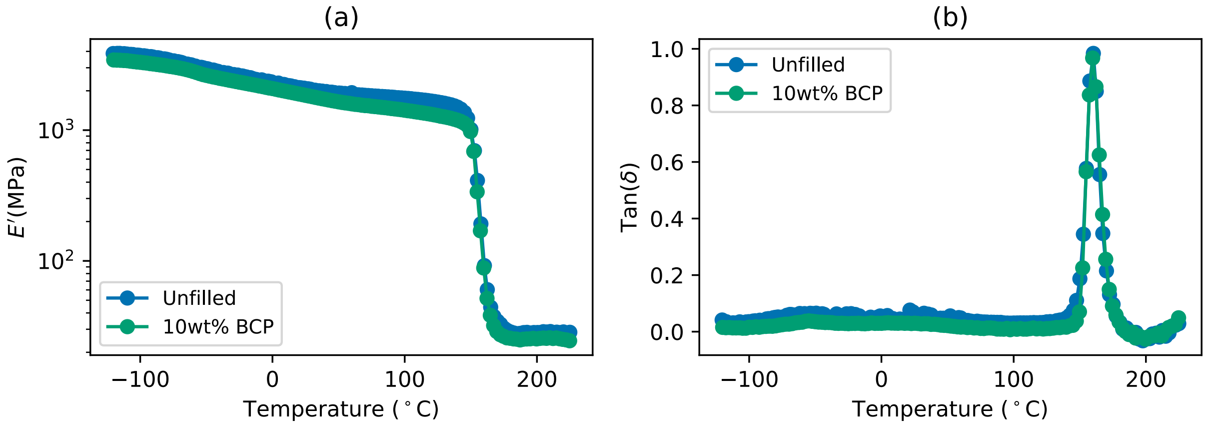

Figure 6.4: Temperature sweep curves for the unfilled DTDA epoxy matrix and 10 wt% BCP-filled DTDA matrix. The temperature dependencies of storage modulus $E^{'}$ (a) and the loss tangent $tan(\delta)$ (b).

6.3.2 Atomic Force Microscopy (AFM) Analysis

The AFM image for the morphologies of the 10wt % BCP-filled DGEBA-DTDA matrix is presented in Figure 6.5. The image reveals the phase contrast between the rubbery PnBA block and the glassy PMMA block within the triblock copolymer. Darker regions indicate the rubbery domain, while lighter areas represent the glassy matrix. Although the rubbery dark domains are relatively uniformly distributed, they are not perfectly spherical and primarily exhibit a domain size in the tens of nanometers range. This aggregation of the rubbery phase mainly results from the phase separation of the epoxy-immiscible PnBA blocks. Since the PMMA blocks are miscible with DGEBA, the addition of amine crosslinkers increases the mixture's polarity and reduces the miscibility of the PMMA segments [130, 131]. This polarity reduction prevents the phase structure of the PnBA to form a self-assembled spherical nanostructure. This phenomenon limits the potential to modify the nanoscale structure of triblock-filled amine crosslinked epoxy matrices.To address this issue, Yamada et al. explored increasing miscibility by hydrolyzing the easter group to generate carboxylic groups on the PMMA blocks of the triblock copolymer, which leads to the formation of different nanostructures including spheres, vesicles and curved lamellae [131].

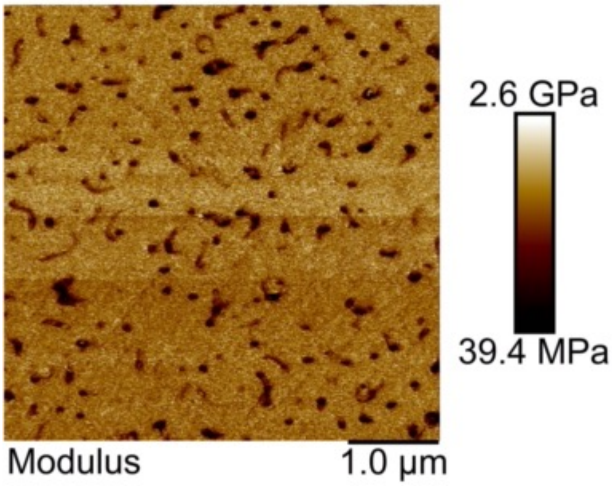

Figure 6.5: Phase-contrast AFM image of a 10 wt% BCP-filled DGEBA-DTDA epoxy matrix. The PnBA aggregated into nano-scale domains and shown as dark region.

6.3.3 Fracture Toughness and The Dugdale Model

The toughness test was conducted following ASTM D5045 using a 3-point, single-notch bending geometry shown in Figure 6.1(b). Both the unfilled epoxy and 10 wt% BCP-filled samples were tested under various temperatures from -100°C to 100°C to assess the toughening effects of triblock copolymer filler to the dynamic disulfide epoxy matrix. Figure 6.6 (a) shows the comparison of fracture toughness between the filled and unfilled epoxy system. The results show that incorporating 10 wt% BCP enhances toughness by approximately 45%, increasing the mode I critical stress intensity factor K_{Ic} from 0.8 MPa$\sqrt{m}$ to about 1.27 MPa$\sqrt{m}$ at room temperature (23°C) . Similar results had been reported by Klingler et al. [144], who observed an increase in K_{IC} from $\sim$0.68 MPa$\sqrt{m}$ to $\sim$1.28 MPa$\sqrt{m}$ upon the addition of 10 wt% BCP into the epoxy matrix. These findings are in excellent agreement with our collected data. This improvement in toughness is maintained across the wide temperature range tested, particularly in the low-temperature regime. This improvement can be attributed to the alteration of the plastic yielding zone at the crack tip, as outlined by the Dugdale model shown in Figure 6.1 (a) and Equation 6.1. Based on the schematic and Equation 6.1, a useful equation to calculate the cohesive zone size r_p is defined[139, 150]:

$$r_p = \frac{\pi E_r \delta_t}{8\sigma_c} = \frac{\pi}{8}(\frac{K_{Ic}}{\sigma_c})^2 \tag{6.8}$$

where r_p is the length of the cohesive zone in Figure 6.1 (a), which is an important observable length scale that directly relates to δ_t when discussing the fracture toughness of a material. To calculate r_p, the cohesive stress σ_c is necessary, which can be effectively substituted by the tensile yield strength σ_y[138]. In order to obtain σ_y, room temperature uniaxial tensile test was conducted for the unfilled epoxy system and the 10 wt% BCP-filled epoxy, as shown in Figure 6.6 (b). The tensile stress-strain curves indicate that the tensile elastic moduli for the two systems are nearly identical, while the ultimate tensile strength (UTS) is reduced by about 20% for the 10 wt% BCP-filled epoxy. This decrease is a typical trade-off to anticipate in rubber-toughened epoxy materials[151].

According to Equation 6.8, the fracture toughness K_{Ic} is not solely dependent on a single parameter, but rather relies on both σ_c and r_p, where σ_c determines the maximum stress that the material can withstand, whiled r_p contributes to reducing the energy dissipation per unit area during the material's fracture process. In the work of Lewis et al.[110], the estimation of r_p of an unfilled DGEBA-DTDA epoxy system is $\approx$ 25 μm and the δ_t is $\approx$ 2 μm. Although the σ_c of the 10 wt% BCP-filled epoxy is 20% lower than that of the unfilled system, its r_p is calculated to be approximately 117 μm at room temperature, which is notably 4 times longer than that of the unfilled system. The corresponding cohesive dissipation zone is further measured using a 3D confocal microscope to support this idea. As the BCP fillers are introduced into the DGEBA-DTDA dynamic epoxy system, the phase-separated PnBA blocks are covalently crosslinked with the partially miscible glassy PMMA blocks, which provides good adhesion to the matrix. When the crack proceeds through the rubbery PnBA-rich matrix, higher energy dissipation occurs to stretch and separate the rubbery nanostructures, increasing the dissipation zone size as well as the fracture toughness of the material. Similar toughening mechanism of BCP in a epoxy matrix was also

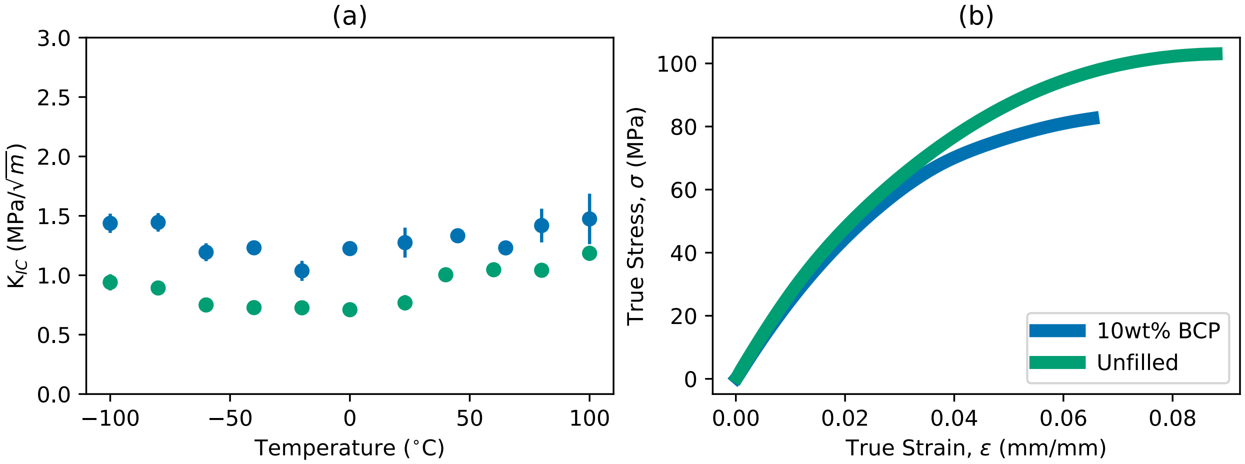

Figure 6.6: (a) Comparison of the critical stress intensity factor,K_{Ic}, between the 10 wt% BCP filled epoxy and the unfilled epoxy matrix. (b) The tensile stress-strain curves for the two systems.

introduced by other publications [144, 152]. In Figure 6.6 (a) at higher temperatures (above room temperature), however, the increase in toughness becomes less pronounced. This can be attributed to the fact that the brittle DTDA system softens and becomes more compliant, causing an increase in the crack tip opening displacement δ_t as well as K_{Ic} [110] at higher temperatures that are closer to the T_g. The increased blunting at the crack tip enlarges δ_t even without the inclusion of the rubbery filler, therefore reducing the prominence of the rubbery filler's stretching effect.

6.3.4 The Fatigue Failure Criterion

During the fatigue test, the crack length is constantly changing, and the test is load-controlled based on the material toughness (K_{Ic}). Therefore, a failure criterion must be established based on the quasi-static loading response [142]. The critical stress intensity factor, K_{IC}, can be expressed as a quasi-static deformation response and plotted as a transition curve. This curve serves as the threshold for fracture failure and represents the relationship between the applied load (P) and the corresponding precrack length (a) when the material fractures, indicating that shorter precracks require higher loads to initiate accelerated crack propagation. Figure 6.7 (b) shows the transition

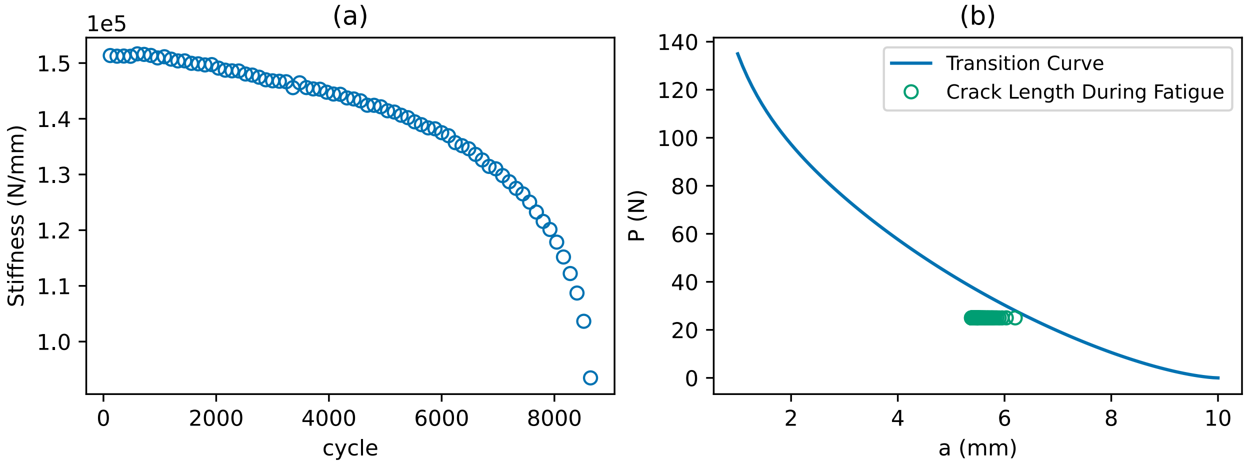

Figure 6.7: The decrease of stiffness during a fatigue test (a) and the transition curve, representing the relationship between load and crack length in a monotonic flexural fracture test, compared to the corresponding crack growth observed under a constant load that is lower than the fracture load (b). Here the transition curve represents a K_{IC} = 1.27 MPa$\sqrt{m}$ for the 10 wt% BCP-filled epoxy matrix.

curve for the 10 wt% BCP-filled matrix with a K_{IC} = 1.27 MPa$\sqrt{m}$ at room temperature, providing a boundary for the catastrophic failure of the specimen.

For the fatigue test, a load lower than the transition curve is chosen, and the crack is gradually propagated over thousands of cycles until it reaches the transition curve. It is important to note that the stiffness of the specimen decreases correspondingly over the fatigue test, as shown in Figure 6.7 (a), which leads to an increase in compliance and an extension of the crack length. By recording the change in crack length and plotting it alongside the transition curve, we can determine if the fracture transition curve can be used as the fatigue failure criterion. During the same fatigue test depicted in Figure 6.7(a), a series of crack lengths were recorded in Figure 6.7 (b) as green dots, using Equation 6.6 and 6.7. The results show that the crack length gradually propagates from a = 5.49 mm to 6.2 mm until it reaches the transition curve and causes catastrophic failure. The crack propagation trajectories were further verified by observing the length of the extended plastic dissipation zone using an Olympus OLS5000 3D confocal microscope, and the cohesive zone lengths were determined using Image J software, as shown in the “Fractography” section.

6.3.5 Fatigue Crack Propagation

The fatigue crack propagation resistance of a pre-cracked stiff material is usually characterized using two quantities: the crack propagation rate (da/dN) and the corresponding stress intensity factor range (ΔK). The relation between the two parameters usually goes through three regimes during a fatigue test, which are:

1. Region I: The threshold regime, in which the crack propagates at a very slow rate and the change in ΔK is minimal. The change in crack length is negligible below the threshold stress intensity factor value, ΔK_{th}. At this stage, fatigue crack growth is dominated by microstructural changes.

2. Region II: The stable crack growth regime, where the relationship between da/dN and ΔK can be correlated using the Paris-Erdogan Law, also known as Paris' law, which shows a linear relationship on a log-log scale:

$$\frac{da}{dN} = C(\Delta K)^m \tag{6.9}$$

The quantity of ΔK is calculated based on a slightly modified version of Equation 6.3:

$$\Delta K = \frac{P - P_{min}}{BW^{1/2}} f(\alpha) \tag{6.10}$$

where $P = \frac{1}{2}P_{max}$ and $P_{min} = 2N$, which are the load range applied onto the SENB sample during the load-controlled test. C is a fitting constant and m is the power-law index for the Paris' Law which is a material-dependent parameter.

3. Region III: The accelerated failure regime, in which the da/dN increases rapidly and ΔK approaches the fracture toughness at the corresponding crack length. During this stage, the crack grows catastrophically, causing material failure.

Typically, Region II is chosen to describe the fatigue crack propagation behaviors between different samples, as it provides a reliable linear fitting on a double logarithmic scale, making the fatigue properties quantitative and comparable. In the double logarithm scales, the crack propagation rate per cycle, da/dN, has linear proportionality to the stress intensity factor range, ΔK, with a slope of m. The calculation process related to the two values is illustrated in Figure 6.8. The values of the crack-to-depth ratio, α, are derived from the compliance change shown in Figure 6.3 (a) and calculated using Equation 6.6 and 6.7. The corresponding crack length values are then derived accordingly, given the sample depth, B, that $a = \alpha \times W$, as shown in Figure 6.8 (a). The crack growth exhibits an acceleration behavior similar to exponential acceleration. Figure 6.8 (c) shows da/dN as a function of the cycle number, derived from the local derivatives or slopes of $a$over cycles. With the calculated crack length as a function of cycle number, the values of ΔK can be obtained using Equation 6.10 and 6.4, as shown in Figure 6.8 (b). Consequently, Figure 6.8 (d) presents the combined data for Paris' Law in double logarithm scale, which clearly shows the transition from Region I to Region II. Figure 6.9 displays the fatigue crack propagation curves for the PACM, unfilled DTDA and BCP-filled DTDA samples. Table 6.1 lists the respective values obtained from the fatigue tests, including the threshold stress intensity factor, ΔK, for the onset of fatigue crack growth and the Paris' law exponent, m.

6.3.5.1 Effects of Triblock Copolymer Filler

By comparing the fatigue curves for unfilled DTDA, 3.1 wt%, 6.5 wt% and 10 wt% filled epoxy matrix, we observe an improvement in fatigue resistance as the curves shift to higher ΔK ranges with increasing BCP concentration. As the BCP concentration increases from 0 wt% to 10 wt%, the threshold value, ΔK_{th}, rises from 0.66 to 0.90, below which the crack propagation rate is neglectable and offers resistance to crack initiation. Once the crack is initiated, the crack propagation enters the Region II, where the Paris' law power law index decreases from m = 39.0 for unfilled

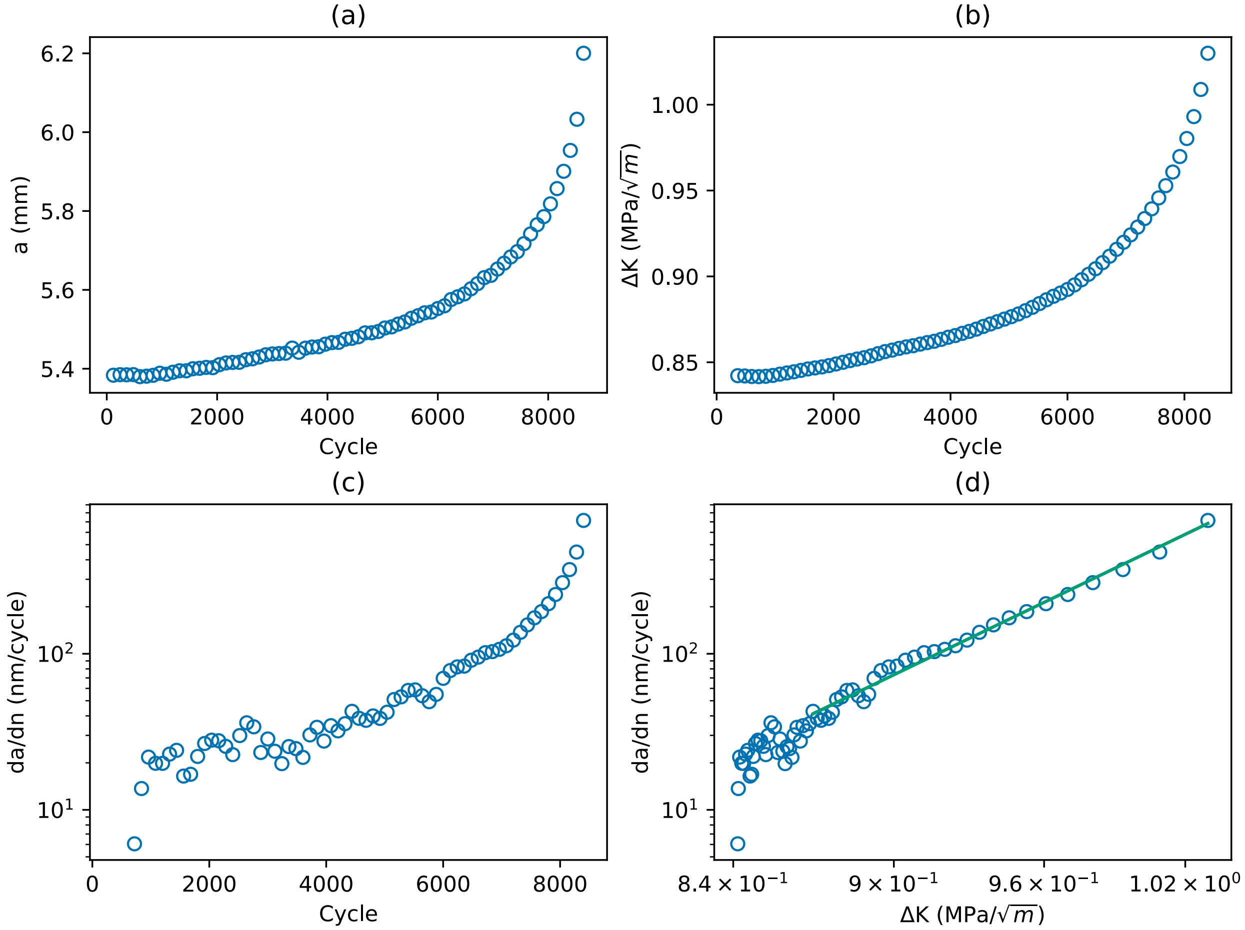

Figure 6.8: Demonstration of methods adopted for determining the crack length and ΔK. (a): Calculation of crack length change over cycles. (b): The derived ΔK values as a function of cycles using the crack length in (a). (c): Crack propagation rate determined from the local first derivative of the crack length data. (d): The combined plot of da/dN as a function of ΔK in double logarithm scale.

DTDA epoxy to m = 18.3 for 10 wt% BCP-filled epoxy as the BCP content increases. The decline of m indicates an improvement of the fatigue crack propagation, and the triblock fillers slow down the acceleration rate of the crack during the stable crack growth process. The toughening effect is most pronounced when comparing crack propagation rates on samples with different filler amounts at the same ΔK values. As shown in Figure 6.9 along a black dashed line (ΔK = 0.91 $MPa\sqrt{m}$), the crack speed drops from 850 nm/cycle to approximately 81 nm/cycle when the filler amount increase from 3.1 wt% to 10 wt%, resulting in an improvement of about an order of magnitude. When the BCP content reaches 6.5wt% or higher, their fatigue curves almost overlap with only minimal shifting to the right observed. These findings are consistent with the results reported by Klingler et al. [144] for their 10 wt% BCP-filled system. The toughening mechanism was elucidated by Klingler et al., who showed that the BCP-rich phase could induce localized plastic deformation, cavitation, bridging, fibrillation, and other effects. These filler arresting mechanisms aid in slowing down crack propagation, accompanied by the phenomena of crack pinning.

6.3.5.2 Effects of Dynamic Disulfide Bonds

In order to compare the effects of the dynamic disulfide bond, the fatigue crack propagation curves of PACM (the non-dynamic stiff crosslinker) and DTDA matrix are compared, as illustrated in Figure 6.9. The ΔK_{th} value of disulfide-containing epoxy matrix (DTDA) is observed to be higher than that of PACM, which may suggest a more mobile network due to the disulfide exchange reactions. For both unfilled systems, crack propagation is relatively fast compared to epoxies filled with triblock copolymers, making the power law index difficult to discern. The values of m are presented at our best estimate in Table 6.1, demonstrating the brittleness of the unfilled systems.

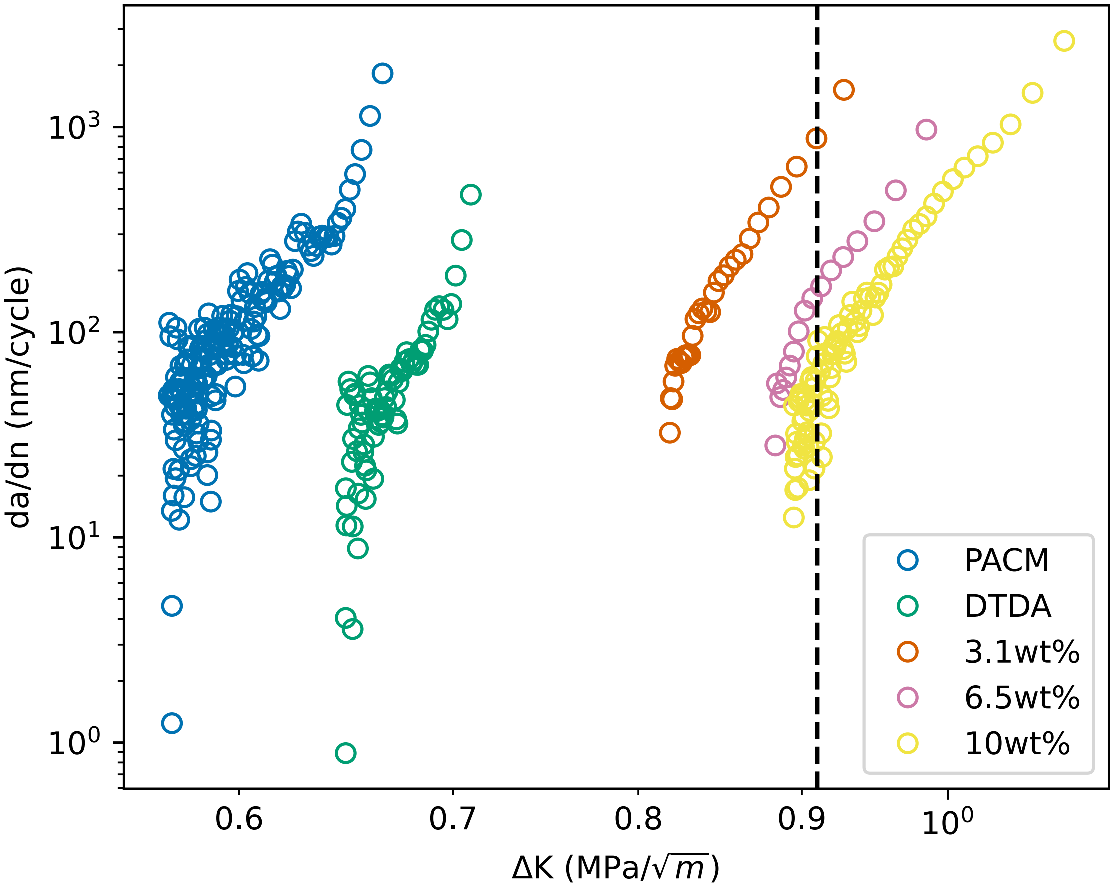

Figure 6.9: The fatigue crack propagation showing da/dN against ΔK in double logarithm scale. The samples shown here include: PACM, unfilled DTDA, 3.1 wt%, 6.5 wt% and 10wt% BCP-filled DTDA epoxy matrix. The black dashed line compares the crack growth rate of 3.1 wt%, 6.5 wt% and 10 wt% BCP-filled epoxy matrix at the same $\Delta K = 0.91\ MPa\sqrt{m}$.

Epoxy Matrix	ΔK_{th} (MPa/$\sqrt{m}$)	m
PACM	0.58	23.0
DTDA (0 wt% BCP)	0.66	39.0
3.1 wt% BCP	0.81	24.4
6.5 wt% BCP	0.90	20.9
10 wt% BCP	0.88	18.3

Table 6.1: Parameters of the unfilled and BCP-filled epoxy matrix from the fatigue crack propagation tests.

6.3.6 Fractography

Equation 6.8 defines the length of the cohesive zone in the Dugdale model, an essential length scale responsible for energy dissipation. We use a 3D laser confocal microscope for direct observation of this dissipation zone. Figure 6.10 (a) presents the side view of a fractured SENB sample. Distinct regions can be identified based on the criteria defined by Eaton et al. [139], which are the initial mold notch, razor blade insertion area and the pre-crack caused by the razor blade (shown in image from bottom to top). Ahead of the pre-crack is the sub-critical crack growth region, highlighted with yellow arrows, typically resulting from localized plastic yielding or cohesive/process zone. We can obtain dimensions from image processing, measuring the widest point of this plastic deformation region as $r_p \approx 110\ \mu m$, which aligns well with the calculated value before (117 μm). Our observation confirms the toughening effect of triblock copolymer filled epoxy matrix by correlating the increased plastic zone size derived from the toughness test with the fractography measurement.

Additionally, microscope observation offers robust support for the flexural fatigue crack propagation method in sample testing. Figure 6.10 (b) shows a broken 10 wt% BCP-filled sample after a fatigue test. Because the crack propagates much slower in this test than in a fracture test, we can observe the crack path by measuring the length of the extended yield zone. Figure 6.10 (b) reveals two crack lengths: 5.4 mm and 6.8 mm. The crack length is determined by selecting its highest point on the sample. Comparing to the calculated crack length, a, in Figure 6.8 (a), the microscope image agrees with the calculated values of the crack length, providing strong support for the legitimacy and accuracy of the fatigue test method adopted in this work.

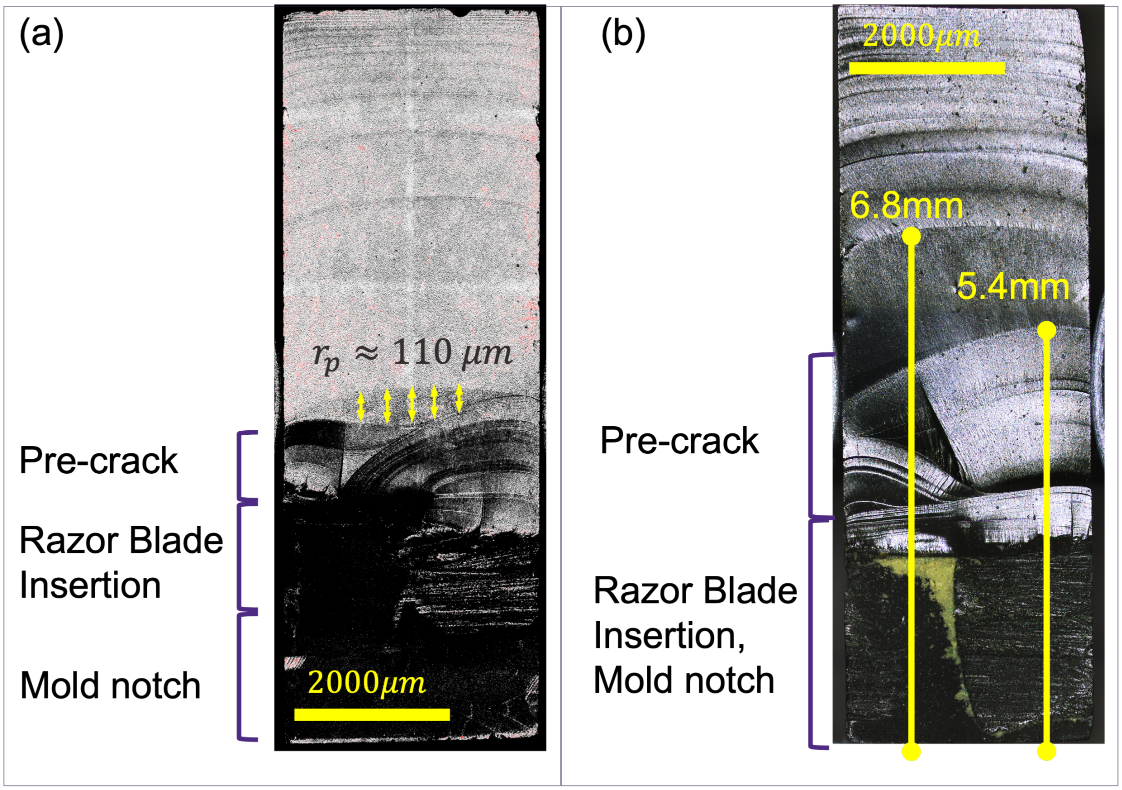

Figure 6.10: 3D confocal microscope images of: (a) 10 wt% BCP-filled epoxy sample after a 3-point-bending fracture toughness test.Yellow arrows highlight regions exhibiting localized yielding. (b) 10 wt% filled sample following the fatigue crack propagation test. The two values (5.4 mm and 6.8 mm) indicate the starting and the ending position of the crack front during the crack growth until it reaches catastrophically failure.

6.4 Conclusion

In this study, we integrated an ABA-type triblock copolymer (PMMA-PnBA-PMMA) into a dynamic disulfide epoxy matrix (DTDA) and explored the toughening effect. Using a SENB geometry, we conducted quasi-static fracture toughness tests, which showed an increase in toughness from 0.8 $MPa\sqrt{m}$ to 1.27 $MPa\sqrt{m}$ with the addition of 10 wt% block copolymer. The enhancement in toughness resulted from an increased cohesive dissipation/ plastic yielding zone, r_p, which expanded from 25 μm for an unfilled matrix to 117 μm for a 10 wt% filled system. This increase in the dissipation zone was verified through direct observation using a 3D laser confocal microscope.

Furthermore, we assessed a 3-point-bending flexural fatigue crack propagation test using the same SENB geometry to examine the fatigue resistance changes brought on by the disulfide bond and the triblock copolymer filler. We evaluated the fatigue resistance of several samples, including PACM, unfilled DTDA, and 3.1, 6.5, and 10 wt% triblock copolymer-filled DTDA. The results demonstrated that incorporating the triblock copolymer filler improved the samples' fatigue resistance by decreasing the Paris' law exponent, m, from 39.0 to 18.3. The threshold stress intensity factor, ΔK_{th}, also increased with more filler added. The presence of disulfide bonds in the DTDA samples contributed to a higher fatigue threshold compared to PACM samples, due to the disulfide bond exchange reactions. These findings further confirm the toughening mechanism proposed by Lewis et al. [110], which suggests that preferential cleavage of disulfide bond increases the ductility of the matrix, thus enhancing its toughness. In fatigue tests, the fracture event's timescale is prolonged, allowing more time for disulfide cleavage and exchange, making these effects more evident.

Chapter 7

Summary and Future Work

7.1 Summary

This thesis discussed three unique strategies for fatigue characterization, each tailored to various polymer systems with distinct mechanical properties. The polymer systems under consideration in this thesis include: rubbery elastomers, lightly crosslinked pressure sensitive adhesives and dynamic epoxy with stiff crosslinkers. Based on the applied cyclic oscillation on the materials, energy dissipation mechanisms are elucidated for comprehending the crack propagation behaviors of polymers within bulk or at interfaces.

Temperature and composition-dependent fatigue crack propagation experiments were conducted on both silicone and natural rubbers. From Chapter 3, we applied large-strain deformation to the elastomers, which enabled us to differentiate between the stored elastic energy ($\mathscr{G}$) and the total input fracture energy Γ via stress-strain correlation. Moreover, we established a strain-dependent effective phase angle, ϕ_{eff}, that corresponds to these two quantities. These energy related quantities were found to be dependent on elastomer networks, including chain structures, filler amount and crosslinking density, as well as environmental factors, such as strain amplitude and temperature. The energy dissipation behavior of natural rubber is significantly influenced by polymer compositions and strain amplitudes, mainly due to their substantial impact on strain-crystallizing behavior. On the other hand, the non-crystallizing silicone rubber behaves more like a general viscoelastic polymer network, with its energy dissipation largely tied to increases in temperature. The driving force for the crack propagation is expressed in a normalized form, $\mathscr{G}/(Eh_0)$, which represents the far-field strain influence on the fatigue crack speed, assuming a Neohookean material response. The deviation of the power law relation between the crack speed, da/dn, and

$\mathscr{G}/(Eh_0)$ for silicone rubber is correlated to the surface morphology change that arise from the crack propagation behavior, which is further discussed in Chapter 4. To quantify these crack surface morphologies, Chapter 4 attempted to examine the surface patterns through several methods, including analyzing cross-hatch angles and calculating local roughness. To understand the implication of the surface patterns, interpretations were conducted at two different length scales (mm scale and μm scale) for feature extraction. It is found that the emergence and transition from a uniformly rough surface to cross-hatch patterns is closely associated with the velocities of crack propagation. Additionally, the overall roughness, represented as the total surface area, increases with the proportion to the value of ϕ_{eff} observed in the polymer matrix.

Chapters 5 and 6 aim to expand the fatigue crack propagation experiments to other polymer systems, particularly those whose fatigue behavior is more challenging to characterize. In Chapter 5, both the bulk and interfacial fatigue behaviors of lightly crosslinked pressure sensitive adhesives are explored using pure shear tensile geometry and probe tack tests conducted through hemispherical indentation experiments. For the pure shear oscillation test, it was discovered that the bulk energy dissipation and mechanical strength of these materials can be restored after a 48-hour resting period. The adhesion tests provided more quantitative information about debonding behaviors. A characteristic strain, ε_c, was defined as a strain rate-independent parameter that denotes the onset of the actual contact area decrease during the interfacial debonding process. The triangular oscillatory indentation test further allowed for the separation of the work of adhesion, W_{adh}, into the bulk dissipation energy Γ and the restored energy, $\mathscr{G}$, which facilitated the quantification of energy distribution between the indenter and the adhesive layer up until the critical value, $\mathscr{G}_c$. Chapter 6 centers on stiff epoxy matrix, specifically analyzing the fatigue crack growth of a dynamic disulfide-containing epoxy system filled with triblock copolymers, using a flexural geometry for characterization. The flexural crack propagation fatigue experiment was proved to be both a simple and effective method for establishing a relationship between the toughness test and crack propagation process till its catastrophic failure. Consequently, this approach serves as a valuable tool in elucidating the toughening effect of both the dynamic disulfide bond and the triblock copolymer fillers, preserving its healing capabilities.

7.2 Future Work

7.2.1 Fracture Mechanics using Advanced Techniques

While the fatigue behavior of polymer materials, spanning a wide range of stiffness, can be feasibly studied through mechanical tests, it remains challenging to elucidate the complex micro-scale fracture mechanics at the process zone near the material's crack tip due to the geometric nonlinearities encountered under large strain. The application of high-accuracy imaging techniques during a mechanical fracture test, such as Digital Image Correlation (DIC), Infrared Thermography, or X-ray scattering, is necessary [1, 17, 36, 153–155]. These techniques can assist in mapping the local damage at the crack tip. In addition, machine learning techniques has been gradually adopted to further uncover hidden information that cannot be interpreted by human eyes. A potential application could involve using a large number of DIC techniques as training sets for machine learning models, thereby enabling the prediction of potential strain field maps before the fracture occurs [156, 157].

7.2.2 Fatigue Analysis of Dynamic Epoxy Systems

Chapter 6 demonstrated that the flexural fatigue setup is a powerful tool for capturing the fatigue crack growth behavior of a notched SENB sample. Future research could focus on further elucidating the activation mechanism of dynamic disulfide, as fatigue tests allow the disulfide-containing network to be active over longer time scales. In subsequent projects, a fully dynamic epoxy network could be created by crosslinking a disulfide-containing epoxy resin, bis(4-glycidyloxyphenyl) disulfide (BGPDS), with the aromatic disulfide diamine monomer, 4,4´-Dithiodianiline (DTDA) [105, 158–160]. The activity of disulfide exchanges can be further enhanced under elevated temperatures, which may significantly contribute to increasing the toughness of glassy epoxy materials.

References

[1] C. Creton, M. Ciccotti, Fracture and adhesion of soft materials: A review, Rep. Prog. Phys. 79 (4) (2016) 046601. doi:10.1088/0034-4885/79/4/046601.

[2] R. Bai, J. Yang, Z. Suo, Fatigue of hydrogels, European Journal of Mechanics - A/Solids 74 (2019) 337–370. doi:10.1016/j.euromechsol.2018.12.001.

[3] C. Creton, Pressure-Sensitive Adhesives: An Introductory Course, MRS Bulletin 28 (6) (2003) 434–439. doi:10.1557/mrs2003.124.

[4] K. Hyun, M. Wilhelm, C. O. Klein, K. S. Cho, J. G. Nam, K. H. Ahn, S. J. Lee, R. H. Ewoldt, G. H. McKinley, A review of nonlinear oscillatory shear tests: Analysis and application of large amplitude oscillatory shear (LAOS), Progress in Polymer Science 36 (12) (2011) 1697–1753. doi:10.1016/j.progpolymsci.2011.02.002.

[5] C. M. Manjunatha, A. R. A. Chandra, N. Jagannathan, Fracture and Fatigue Behavior of Polymer Nanocomposites—A Review 95 (2015) 18.

[6] S. C. Shit, P. Shah, A Review on Silicone Rubber, Natl. Acad. Sci. Lett. 36 (4) (2013) 355–365. doi:10.1007/s40009-013-0150-2.

[7] J. R. Beatty, Fatigue of Rubber, Rubber Chemistry and Technology 37 (5) (1964) 1341–1364. doi:10.5254/1.3540402.

[8] K. R. Shull, A. J. Crosby, C. M. Flanigan, Adhesion of Triblock Copolymer-Based Thermoreversible Gels and Pressure Sensitive Adhesives, MRS Online Proceedings Library 629 (1) (2011) 82. doi:10.1557/PROC-629-FF8.2.

[9] S. Sun, M. Li, A. Liu, A review on mechanical properties of pressure sensitive adhesives, International Journal of Adhesion and Adhesives 41 (2013) 98–106. doi:10.1016/j.ijadhadh.2012.10.011.

[10] W. Jo, K. Jeong, Y.-S. Park, J.-I. Lee, S. Gap Im, T.-S. Kim, Thermally stable and soft pressure-sensitive adhesive for foldable electronics, Chemical Engineering Journal 452 (2023) 139050. doi:10.1016/j.cej.2022.139050.

[11] Griffith Alan Arnold, Taylor Geoffrey Ingram, VI. The phenomena of rupture and flow in solids, Philosophical Transactions of the Royal Society of London. Series A, Containing Papers of a Mathematical or Physical Character 221 (582-593) (1921) 163–198. doi:10.1098/rsta.1921.0006.

[12] K. R. Shull, Fracture and adhesion of elastomers and gels: Large strains at small length scales, Journal of Polymer Science Part B: Polymer Physics 44 (24) (2006) 3436–3439. doi:10.1002/polb.21005.

[13] J. A. Kies, A. M. Sullivan, G. R. Irwin, Interpretation of Fracture Markings, Journal of Applied Physics 21 (1950) 716–720. doi:10.1063/1.1699739.

[14] C.-Y. Hui, T. Tang, Y.-Y. Lin, Manoj. K. Chaudhury, Failure of Elastomeric Polymers Due to Rate Dependent Bond Rupture, Langmuir 20 (14) (2004) 6052–6064. doi:10.1021/la0356607.

[15] C.-Y. Hui, J. A., S. J. Bennison, J. D. Londono, Crack blunting and the strength of soft elastic solids, Proceedings of the Royal Society of London. Series A: Mathematical, Physical and Engineering Sciences 459 (2034) (2003) 1489–1516. doi:10.1098/rspa.2002.1057.

[16] M. E. Seitz, D. Martina, T. Baumberger, V. R. Krishnan, C.-Y. Hui, K. R. Shull, Fracture and large strain behavior of self-assembled triblock copolymer gels, Soft Matter 5 (2) (2009) 447–456. doi:10.1039/B810041A.

[17] S. Mzabi, D. Berghezan, S. Roux, F. Hild, C. Creton, A critical local energy release rate criterion for fatigue fracture of elastomers, J. Polym. Sci. B Polym. Phys. 49 (21) (2011) 1518–1524. doi:10.1002/polb.22338.

[18] W. V. Mars, A. Fatemi, A literature survey on fatigue analysis approaches for rubber, International Journal of Fatigue 24 (9) (2002) 949–961. doi:10.1016/S0142-1123(02)00008-7.

[19] R. Bai, J. Yang, X. P. Morelle, C. Yang, Z. Suo, Fatigue Fracture of Self-Recovery Hydrogels, ACS Macro Lett. 7 (3) (2018) 312–317. doi:10.1021/acsmacrolett.8b00045.

[20] R. Rivlin, A. Thomas, Rupture of rubber. I. Characteristic energy for tearing, J. Polym. Sci. 10 (1953) 291–318.

[21] A. G. Thomas, Rupture of rubber. II. The strain concentration at an incision, Journal of Polymer Science 18 (88) (1955) 177–188. doi:10.1002/pol.1955.120188802.

[22] A. N. Gent, P. B. Lindley, A. G. Thomas, Cut growth and fatigue of rubbers. I. The relationship between cut growth and fatigue, Journal of Applied Polymer Science 8 (1) (1964) 455–466. doi:10.1002/app.1964.070080129.

[23] G. J. Lake, P. B. Lindley, Cut growth and fatigue of rubbers. II. Experiments on a noncrystallizing rubber, Journal of Applied Polymer Science 8 (2) (1964) 707–721. doi:10.1002/app.1964.070080212.

[24] G. J. Lake, P. B. Lindley, The mechanical fatigue limit for rubber, Journal of Applied Polymer Science 9 (4) (1965) 1233–1251. doi:10.1002/app.1965.070090405.

[25] A. N. Gent, R. P. Petrich, D. Tabor, Adhesion of viscoelastic materials to rigid substrates, Proceedings of the Royal Society of London. A. Mathematical and Physical Sciences 310 (1502) (1997) 433–448. `doi:10.1098/rspa.1969.0085`.

[26] A. J. Crosby, K. R. Shull, H. Lakrout, C. Creton, Deformation and failure modes of adhesively bonded elastic layers, Journal of Applied Physics 88 (5) (2000) 2956–2966. `doi:10.1063/1.1288017`.

[27] A. J. Crosby, K. R. Shull, Adhesive failure analysis of pressure-sensitive adhesives, Journal of Polymer Science Part B: Polymer Physics 37 (24) (1999) 3455–3472. `doi:10.1002/(SICI)1099-0488(19991215)37:24<3455::AID-POLB7>3.0.CO;2-3`.

[28] A. J. Crosby, K. R. Shull, Y. Y. Lin, C.-Y. Hui, Rheological properties and adhesive failure of thin viscoelastic layers, Journal of Rheology 46 (1) (2002) 273–294. `doi:10.1122/1.1428316`.

[29] K. R. Shull, C. M. Flanigan, A. J. Crosby, Fingering Instabilities of Confined Elastic Layers in Tension, Phys. Rev. Lett. 84 (14) (2000) 3057–3060. `doi:10.1103/PhysRevLett.84.3057`.

[30] K. R. Shull, Contact mechanics and the adhesion of soft solids, Materials Science and Engineering: R: Reports 36 (1) (2002) 1–45. `doi:10.1016/S0927-796X(01)00039-0`.

[31] Q. Wang, W. B. Griffith, M. Einsla, S. Zhang, M. L. Pacholski, K. R. Shull, Bulk and Interfacial Contributions to the Adhesion of Acrylic Emulsion-Based Pressure-Sensitive Adhesives, Macromolecules 53 (16) (2020) 6975–6983. `doi:10.1021/acs.macromol.0c01354`.

[32] R. E. Webber, K. R. Shull, Strain Dependence of the Viscoelastic Properties of Alginate Hydrogels, Macromolecules 37 (2004) 6153–6160. `doi:10.1021/ma049274n`.

[33] Q. Chen, S. Xu, M. Lu, J. Liu, K. R. Shull, Temperature-Dependent Viscoelastic Energy Dissipation and Fatigue Crack Growth in Filled Silicone Elastomers, ACS Appl. Polym. Mater. 3 (12) (2021) 6207–6217. `doi:10.1021/acsapm.1c01007`.

[34] D. G. Young, J. A. Danik, Effects of Temperature on Fatigue and Fracture, Rubber Chemistry and Technology 67 (1) (1994) 137–147. `arXiv:https://doi.org/10.5254/1.3538660`, `doi:10.5254/1.3538660`.

[35] W. V. Mars, A. Fatemi, Factors that affect the fatigue life of rubber: A literature survey, Rubber Chemistry and Technology 77 (3) (2004) 391–412.

[36] Q. Demassieux, D. Berghezan, S. Cantournet, H. Proudhon, C. Creton, Temperature and aging dependence of strain-induced crystallization and cavitation in highly crosslinked and

filled natural rubber, Journal of Polymer Science Part B: Polymer Physics 57 (12) (2019) 780–793. doi:10.1002/polb.24832.

[37] C. J. Yeh, M. Dowland, R. G. Schmidt, K. R. Shull, Fracture and thermal aging of resin-filled silicone elastomers, Journal of Polymer Science Part B: Polymer Physics 54 (2) (2016) 263–273. doi:10.1002/polb.23919.

[38] S. V. Hainsworth, An environmental scanning electron microscopy investigation of fatigue crack initiation and propagation in elastomers, Polymer Testing 26 (1) (2007) 60–70. doi:10.1016/j.polymertesting.2006.08.007.

[39] Q. Han, L. Zhang, Y. Wu, Relationship between dynamic fatigue crack propagation properties and viscoelasticity of natural rubber/silicone rubber composites.

[40] Q. Han, L. Zhang, Y. Wu, Enhanced Interfacial Compatibility and Dynamic Fatigue Crack Propagation Behavior of Natural Rubber/Silicone Rubber Composites, Ind. Eng. Chem. Res. 59 (35) (2020) 15624–15633. doi:10.1021/acs.iecr.0c03493.

[41] B. N. J. Persson, E. A. Brener, Crack propagation in viscoelastic solids, Phys. Rev. E 71 (3) (2005) 036123. doi:10.1103/PhysRevE.71.036123.

[42] Y. Morishita, K. Tsunoda, K. Urayama, Velocity transition in the crack growth dynamics of filled elastomers: Contributions of nonlinear viscoelasticity, Phys. Rev. E 93 (4) (2016) 043001. doi:10.1103/PhysRevE.93.043001.

[43] H. W. Greensmith, Rupture of rubber. IV. Tear properties of vulcanizates containing carbon black, Journal of Polymer Science 21 (98) (1956) 175–187. doi:10.1002/pol.1956.120219802.

[44] P. B. Lindley, Relation between hysteresis and the dynamic crack growth resistance of natural rubber, Int J Fract 9 (4) (1973) 449–462. doi:10.1007/BF00036325.

[45] S. Toki, I. Sics, S. Ran, L. Liu, B. S. Hsiao, S. Murakami, K. Senoo, S. Kohjiya, New Insights into Structural Development in Natural Rubber during Uniaxial Deformation by In Situ Synchrotron X-ray Diffraction, Macromolecules 35 (17) (2002) 6578–6584. doi:10.1021/ma0205921.

[46] B. Wang, H. Lu, G.-h. Kim, A damage model for the fatigue life of elastomeric materials, Mechanics of Materials 34 (8) (2002) 475–483. doi:10.1016/S0167-6636(02)00175-8.

[47] W. V. Mars, A. Fatemi, Fatigue crack nucleation and growth in filled natural rubber, Fatigue & Fracture of Engineering Materials & Structures 26 (9) (2003) 779–789. doi:10.1046/j.1460-2695.2003.00678.x.

[48] W. V. Mars, A. Fatemi, Multiaxial fatigue of rubber: Part II: Experimental observations and life predictions, Fatigue & Fracture of Engineering Materials & Structures 28 (6) (2005) 523–538. doi:10.1111/j.1460-2695.2005.00895.x.

[49] W. V. Mars, A. Fatemi, Multiaxial stress effects on fatigue behavior of filled natural rubber, International Journal of Fatigue 28 (5–6) (2006) 521–529. doi:10.1016/j.ijfatigue.2005.07.040.

[50] C.-S. Woo, W.-D. Kim, S.-H. Lee, B.-I. Choi, H.-S. Park, Fatigue life prediction of vulcanized natural rubber subjected to heat-aging, Procedia Engineering 1 (1) (2009) 9–12. doi:10.1016/j.proeng.2009.06.004.

[51] W. Luo, M. Li, Y. Huang, B. Yin, X. Hu, Effect of Temperature on the Tear Fracture and Fatigue Life of Carbon-Black-Filled Rubber, Polymers (Basel) 11 (5). doi:10.3390/polym11050768.

[52] L. Mullins, Effect of Stretching on the Properties of Rubber, Rubber Chemistry and Technology 21 (2) (1948) 281–300. doi:10.5254/1.3546914.

[53] L. Mullins, Permanent Set in Vulcanized Rubber, Rubber Chemistry and Technology 22 (4) (1949) 1036–1044. doi:10.5254/1.3543010.

[54] C. M. Roland, Network Recovery from Uniaxial Extension: II. The Origin of the Mullins Effect, Rubber Chemistry and Technology 62 (5) (1989) 880–895. doi:10.5254/1.3536281.

[55] J. Diani, M. Brieu, J. M. Vacherand, A damage directional constitutive model for Mullins effect with permanent set and induced anisotropy, European Journal of Mechanics - A/Solids 25 (3) (2006) 483–496. doi:10.1016/j.euromechsol.2005.09.011.

[56] R. E. Webber, C. Creton, H. R. Brown, J. P. Gong, Large Strain Hysteresis and Mullins Effect of Tough Double-Network Hydrogels, Macromolecules 40 (8) (2007) 2919–2927. doi:10.1021/ma062924y.

[57] G. Scetta, N. Selles, P. Heuillet, M. Ciccotti, C. Creton, Cyclic fatigue failure of TPU using a crack propagation approach, Polymer Testing 97 (2021) 107140. doi:10.1016/j.polymertesting.2021.107140.

[58] G. Scetta, Fatigue cracking of Thermoplastic Elastomers, Ph.D. thesis, École supérieure de physique et de chimie industrielles de la Ville de Paris (2020).

[59] A. R. Payne, The dynamic properties of carbon black-loaded natural rubber vulcanizates. Part I, Journal of Applied Polymer Science 6 (19) (1962) 57–63. doi:10.1002/app.1962.070061906.

[60] Y. Merckel, J. Diani, M. Brieu, D. Berghezan, Experimental characterization and modelling of the cyclic softening of carbon-black filled rubbers, Materials Science and Engineering: A 528 (29) (2011) 8651–8659. doi:10.1016/j.msea.2011.08.023.

[61] W.-C. Lin, K. R. Shull, C.-Y. Hui, Y.-Y. Lin, Contact Measurement of Internal Fluid Flow within Poly(n-isopryl acrylamide) Gels, J. Chem. Phys. 127 (2007) 094906. doi:10.1063/1.2771167.

[62] X. Zhao, Multi-scale multi-mechanism design of tough hydrogels: Building dissipation into stretchy networks, Soft Matter 10 (5) (2014) 672–687. doi:10.1039/C3SM52272E.

[63] G. Scetta, J. Ju, N. Selles, P. Heuillet, M. Ciccotti, C. Creton, Strain induced strengthening of soft thermoplastic polyurethanes under cyclic deformation, Journal of Polymer Science 59 (8) (2021) 685–696. doi:10.1002/pol.20210060.

[64] K. R. Shull, C. Creton, Deformation behavior of thin, compliant layers under tensile loading conditions, Journal of Polymer Science Part B: Polymer Physics 42 (22) (2004) 4023–4043. doi:10.1002/polb.20258.

[65] A. N. Gent, C. T. R. Pulford, Micromechanics of fracture in elastomers, J Mater Sci 19 (11) (1984) 3612–3619. doi:10.1007/BF00552273.

[66] Y. Tanaka, K. Fukao, Y. Miyamoto, K. Sekimoto, Discontinuous crack fronts of three-dimensional fractures, Europhys. Lett. 43 (6) (1998) 664–670. doi:10.1209/epl/i1998-00565-4.

[67] T. Baumberger, C. Caroli, D. Martina, O. Ronsin, Magic Angles and Cross-Hatching Instability in Hydrogel Fracture, Phys. Rev. Lett. 100 (17) (2008) 178303. doi:10.1103/PhysRevLett.100.178303.

[68] O. Ronsin, C. Caroli, T. Baumberger, Crack front échelon instability in mixed mode fracture of a strongly nonlinear elastic solid, EPL 105 (3) (2014) 34001. doi:10.1209/0295-5075/105/34001.

[69] I. Kolvin, G. Cohen, J. Fineberg, Topological defects govern crack front motion and facet formation on broken surfaces, Nature Materials 17 (2) (2018) 140–144. doi:10.1038/nmat5008.

[70] A. Vasudevan, L. Ponson, A. Karma, J.-B. Leblond, Configurational stability of a crack propagating in a material with mode-dependent fracture energy – Part II: Drift of fracture facets in mixed-mode I+II+III, Journal of the Mechanics and Physics of Solids 137 (2020) 103894. doi:10.1016/j.jmps.2020.103894.

[71] Y. Fukahori, E. H. Andrews, Fracture surface roughness in highly deformable polymers, J Mater Sci 13 (4) (1978) 777–785. doi:10.1007/BF00570512.

[72] V. R. Krishnan, C. Y. Hui, R. Long, Finite Strain Crack Tip Fields in Soft Incompressible Elastic Solids, Langmuir 24 (24) (2008) 14245–14253. doi:10.1021/la802795e.

[73] U. F. Ghumman, Q. Chen, V. E. D'Angelo, M. Clark, J. Chen, K. R. Shull, W. Chen, Crack Surface Analysis of Elastomers Using Transfer Learning, ACS Appl. Mater. Interfacesdoi:10.1021/acsami.2c19309.

[74] H. W. Greensmith, A. G. Thomas, Rupture of rubber. III. Determination of tear properties, Journal of Polymer Science 18 (88) (1955) 189–200. doi:10.1002/pol.1955.120188803.

[75] I. Kolvin, G. Cohen, J. Fineberg, Crack Front Dynamics: The Interplay of Singular Geometry and Crack Instabilities, Phys. Rev. Lett. 114 (17) (2015) 175501. doi:10.1103/PhysRevLett.114.175501.

[76] M. Wang, M. Adda-Bedia, J. M. Kolinski, J. Fineberg, How hidden 3D structure within crack fronts reveals energy balance, Journal of the Mechanics and Physics of Solids 161 (2022) 104795. doi:10.1016/j.jmps.2022.104795.

[77] Y. Zhao, X. Zhao, B. Wang, A speech enhancement method based on sparse reconstruction of power spectral density, Computers & Electrical Engineering 40 (4) (2014) 1080–1089. doi:10.1016/j.compeleceng.2013.12.007.

[78] L. Zhou, J. Gan, X. Liu, L. Xu, W. Lu, Speckle-noise-reduction method of projecting interferometry fringes based on power spectrum density, Appl. Opt., AO 51 (29) (2012) 6974–6978. doi:10.1364/AO.51.006974.

[79] P. Dash, P. Mallick, H. Rath, A. Tripathi, J. Prakash, D. K. Avasthi, S. Mazumder, S. Varma, P. V. Satyam, N. C. Mishra, Surface roughness and power spectral density study of SHI irradiated ultra-thin gold films, Applied Surface Science 256 (2) (2009) 558–561. doi:10.1016/j.apsusc.2009.08.046.

[80] Y. Gong, S. T. Misture, P. Gao, N. P. Mellott, Surface Roughness Measurements Using Power Spectrum Density Analysis with Enhanced Spatial Correlation Length, J. Phys. Chem. C 120 (39) (2016) 22358–22364. doi:10.1021/acs.jpcc.6b06635.

[81] Z. Esfahani, E. Rahimi, M. Sarvghad, A. Rafsanjani-Abbasi, A. Davoodi, Correlation between the histogram and power spectral density analysis of AFM and SKPFM images in an AA7023/AA5083 FSW joint, Journal of Alloys and Compounds 744 (2018) 174–181. doi:10.1016/j.jallcom.2018.02.106.

[82] T. Jacobs, T. Junge, L. Pastewka, Quantitative characterization of surface topography using spectral analysis, Surf. Topogr.: Metrol. Prop. 5 (1) (2017) 013001. arXiv:1607.03040, doi:10.1088/2051-672X/aa51f8.

[83] B. N. J. Persson, O. Albohr, G. Heinrich, H. Ueba, Crack propagation in rubber-like materials, J. Phys.: Condens. Matter 17 (44) (2005) R1071–R1142. doi:10.1088/0953-8984/17/44/R01.

[84] S. Mapari, S. Mestry, S. T. Mhaske, Developments in pressure-sensitive adhesives: A review, Polym. Bull. 78 (7) (2021) 4075–4108. doi:10.1007/s00289-020-03305-1.

[85] G. Desroches, Y. Wang, J. Kubiak, R. Macfarlane, Crosslinking of Pressure-Sensitive Adhesives with Polymer-Grafted Nanoparticles, ACS Appl. Mater. Interfaces 14 (7) (2022) 9579–9586. doi:10.1021/acsami.1c22997.

[86] J. A. Williams, J. J. Kauzlarich, Application of the bulk properties of a silicone PSA to peeling, International Journal of Adhesion and Adhesives 28 (4) (2008) 192–198. doi:10.1016/j.ijadhadh.2007.06.007.

[87] J. Renvoise, D. Burlot, G. Marin, C. Derail, Peeling of PSAs on Viscoelastic Substrates: A Failure Criterion, The Journal of Adhesion 83 (4) (2007) 403–416. doi:10.1080/00218460701282554.

[88] J.-H. Lee, K.-M. Kim, H.-J. Kim, Y. Kim, Ultraviolet-patterned acrylic pressure-sensitive adhesives for flexible displays, Polymer 237 (2021) 124324. doi:10.1016/j.polymer.2021.124324.

[89] A. L. Dobson, N. J. Bongiardina, C. N. Bowman, Combined Dynamic Network and Filler Interface Approach for Improved Adhesion and Toughness in Pressure-Sensitive Adhesives, ACS Appl. Polym. Mater. 2 (3) (2020) 1053–1060. doi:10.1021/acsapm.9b00992.

[90] H. Yang, W. Zhang, R. D. Moffitt, T. C. Ward, D. A. Dillard, Multi-layer in-situ for evaluation of dynamic mechanical properties of pressure sensitive adhesives, International Journal of Adhesion and Adhesives 27 (7) (2007) 536–546. doi:10.1016/j.ijadhadh.2006.09.014.

[91] W.-C. Lin, K. J. Otim, J. L. Lenhart, P. J. Cole, K. R. Shull, Indentation fracture of silicone gels, Journal of Materials Research 24 (3) (2009) 957–965. doi:10.1557/jmr.2009.0128.

[92] C. M. Flanigan, A. J. Crosby, K. R. Shull, Structural Development and Adhesion of Acrylic ABA Triblock Copolymer Gels, Macromolecules 32 (21) (1999) 7251–7262. doi:10.1021/ma990873h.

[93] M. M. Abdel Wahab, Fatigue in Adhesively Bonded Joints: A Review, ISRN Materials Science 2012 (2012) 1–25. doi:10.5402/2012/746308.

[94] P. Zuo, A. P. Vassilopoulos, Review of fatigue of bulk structural adhesives and thick adhesive joints, International Materials Reviews 66 (5) (2021) 313–338. doi:10.1080/09506608.2020.1845110.

[95] A. J. Silvaroli, T. R. Heyl, Z. Qiang, J. M. Beebe, D. Ahn, S. Mangold, K. R. Shull, M. Wang, Tough, Transparent, Photocurable Hybrid Elastomers, ACS Appl. Mater. Interfaces 12 (39) (2020) 44125–44136. doi:10.1021/acsami.0c11643.

[96] L. Lu, J. Pan, G. Li, Recyclable high-performance epoxy based on transesterification reaction, Journal of Materials Chemistry A 5 (40) (2017) 21505–21513. doi:10.1039/C7TA06397K.

[97] F. I. Altuna, C. E. Hoppe, R. J. J. Williams, Epoxy vitrimers with a covalently bonded tertiary amine as catalyst of the transesterification reaction, European Polymer Journal 113 (2019) 297–304. doi:10.1016/j.eurpolymj.2019.01.045.

[98] J.-H. Chen, J.-H. Lu, X.-L. Pu, L. Chen, Y.-Z. Wang, Recyclable, malleable and intrinsically flame-retardant epoxy resin with catalytic transesterification, Chemosphere 294 (2022) 133778. doi:10.1016/j.chemosphere.2022.133778.

[99] N. Bai, K. Saito, G. P. Simon, Synthesis of a diamine cross-linker containing Diels–Alder adducts to produce self-healing thermosetting epoxy polymer from a widely used epoxy monomer, Polymer Chemistry 4 (3) (2013) 724–730. doi:10.1039/C2PY20611K.

[100] X. Kuang, G. Liu, X. Dong, X. Liu, J. Xu, D. Wang, Facile fabrication of fast recyclable and multiple self-healing epoxy materials through diels-alder adduct cross-linker, Journal of Polymer Science Part A: Polymer Chemistry 53 (18) (2015) 2094–2103. doi:10.1002/pola.27655.

[101] D. H. Turkenburg, H. R. Fischer, Diels-Alder based, thermo-reversible cross-linked epoxies for use in self-healing composites, Polymer 79 (2015) 187–194. doi:10.1016/j.polymer.2015.10.031.

[102] S. Zhao, M. M. Abu-Omar, Recyclable and Malleable Epoxy Thermoset Bearing Aromatic Imine Bonds, Macromolecules 51 (23) (2018) 9816–9824. doi:10.1021/acs.macromol.8b01976.

[103] Q. Yu, X. Peng, Y. Wang, H. Geng, A. Xu, X. Zhang, W. Xu, D. Ye, Vanillin-based degradable epoxy vitrimers: Reprocessability and mechanical properties study, European Polymer Journal 117 (2019) 55–63. doi:10.1016/j.eurpolymj.2019.04.053.

[104] M. A. Rashid, S. Zhu, Q. Jiang, Y. Wei, W. Liu, Developing Easy Processable, Recyclable, and Self-Healable Biobased Epoxy Resin through Dynamic Covalent Imine Bonds, ACS Appl. Polym. Mater. 5 (1) (2023) 279–289. doi:10.1021/acsapm.2c01501.

[105] J. Canadell, H. Goossens, B. Klumperman, Self-Healing Materials Based on Disulfide Links, Macromolecules 44 (8) (2011) 2536–2541. doi:10.1021/ma2001492.

[106] M. Pepels, I. Filot, B. Klumperman, H. Goossens, Self-healing systems based on disulfide–thiol exchange reactions, Polym. Chem. 4 (18) (2013) 4955–4965. doi:10.1039/C3PY00087G.

[107] A. Takahashi, T. Ohishi, R. Goseki, H. Otsuka, Degradable epoxy resins prepared from diepoxide monomer with dynamic covalent disulfide linkage, Polymer 82 (2016) 319–326. doi:10.1016/j.polymer.2015.11.057.

[108] A. R. de Luzuriaga, J. M. Matxain, F. Ruipérez, R. Martin, J. M. Asua, G. Cabañero, I. Odriozola, Transient mechanochromism in epoxy vitrimer composites containing aromatic disulfide crosslinks, J. Mater. Chem. C 4 (26) (2016) 6220–6223. doi:10.1039/C6TC02383E.

[109] B. Li, G. Zhu, Y. Hao, T. Ren, An investigation on the performance of epoxy vitrimers based on disulfide bond, Journal of Applied Polymer Science 139 (5) (2022) 51589. doi:10.1002/app.51589.

[110] B. Lewis, J. M. Dennis, K. R. Shull, Effects of Dynamic Disulfide Bonds on Mechanical Behavior in Glassy Epoxy Thermosets, ACS Appl. Polym. Mater. 5 (4) (2023) 2583–2595. doi:10.1021/acsapm.2c02194.

[111] F. Ji, X. Liu, D. Sheng, Y. Yang, Epoxy-vitrimer composites based on exchangeable aromatic disulfide bonds: Reprocessibility, adhesive, multi-shape memory effect, Polymer 197 (2020) 122514. doi:10.1016/j.polymer.2020.122514.

[112] I. Azcune, I. Odriozola, Aromatic disulfide crosslinks in polymer systems: Self-healing, reprocessability, recyclability and more, European Polymer Journal 84 (2016) 147–160. doi:10.1016/j.eurpolymj.2016.09.023.

[113] S. Nevejans, N. Ballard, J. I. Miranda, B. Reck, J. M. Asua, The underlying mechanisms for self-healing of poly(disulfide)s, Phys. Chem. Chem. Phys. 18 (39) (2016) 27577–27583. doi:10.1039/C6CP04028D.

[114] Y. L. Liang, R. A. Pearson, Toughening mechanisms in epoxy–silica nanocomposites (ESNs), Polymer 50 (20) (2009) 4895–4905. doi:10.1016/j.polymer.2009.08.014.

[115] H. Zhang, L.-C. Tang, Z. Zhang, K. Friedrich, S. Sprenger, Fracture behaviours of in situ silica nanoparticle-filled epoxy at different temperatures, Polymer 49 (17) (2008) 3816–3825. doi:10.1016/j.polymer.2008.06.040.

[116] L. Liu, H. D. Wagner, Rubbery and glassy epoxy resins reinforced with carbon nanotubes, Composites Science and Technology 65 (11) (2005) 1861–1868. doi:10.1016/j.compscitech.2005.04.002.

[117] I. Rafique, A. Kausar, Z. Anwar, B. Muhammad, Exploration of Epoxy Resins, Hardening Systems, and Epoxy/Carbon Nanotube Composite Designed for High Performance Materials: A Review, Polymer-Plastics Technology and Engineering 55 (3) (2016) 312–333. doi:10.1080/03602559.2015.1070874.

[118] N. Shirodkar, S. Cheng, G. D. Seidel, Enhancement of Mode I fracture toughness properties of epoxy reinforced with graphene nanoplatelets and carbon nanotubes, Composites Part B: Engineering 224 (2021) 109177. doi:10.1016/j.compositesb.2021.109177.

[119] L.-C. Tang, Y.-J. Wan, D. Yan, Y.-B. Pei, L. Zhao, Y.-B. Li, L.-B. Wu, J.-X. Jiang, G.-Q. Lai, The effect of graphene dispersion on the mechanical properties of graphene/epoxy composites, Carbon 60 (2013) 16–27. doi:10.1016/j.carbon.2013.03.050.

[120] A. Kausar, Rubber toughened epoxy-based nanocomposite: A promising pathway toward advanced materials, Journal of Macromolecular Science, Part A 57 (7) (2020) 499–511. doi:10.1080/10601325.2020.1730190.

[121] R. Bagheri, B. T. Marouf, R. A. Pearson, Rubber-Toughened Epoxies: A Critical Review, Polymer Reviews 49 (3) (2009) 201–225. doi:10.1080/15583720903048227.

[122] A. C. Garg, Y.-W. Mai, Failure mechanisms in toughened epoxy resins—A review, Composites Science and Technology 31 (3) (1988) 179–223. doi:10.1016/0266-3538(88)90009-7.

[123] P. L. Drzal, K. R. Shull, Origins of Mechanical Strength and Elasticity in Thermally Reversible, Acrylic Triblock Copolymer Gels, Macromolecules 36 (6) (2003) 2000–2008. doi:10.1021/ma021255v.

[124] M. Guvendiren, K. R. Shull, Self-assembly of acrylic triblock hydrogels by vapor-phase solvent exchange, Soft Matter 3 (5) (2007) 619–626. doi:10.1039/B615412C.

[125] M. E. Seitz, W. R. Burghardt, K. T. Faber, K. R. Shull, Self-Assembly and Stress Relaxation in Acrylic Triblock Copolymer Gels, Macromolecules 40 (4) (2007) 1218–1226. doi:10.1021/ma061993+.

[126] M. E. Seitz, W. R. Burghardt, K. R. Shull, Micelle Morphology and Mechanical Response of Triblock Gels, Macromolecules 42 (22) (2009) 9133–9140. doi:10.1021/ma901448x.

[127] M. Zabet, S. Mishra, R. Boy, K. B. Walters, A. K. Naskar, S. Kundu, Temperature-dependent self-assembly and rheological behavior of a thermoreversible pmma–PnBA–PMMA triblock copolymer gel, Journal of Polymer Science Part B: Polymer Physics 55 (11) (2017) 877–887. doi:10.1002/polb.24336.

[128] S. Mishra, R. M. Badani Prado, S. Zhang, T. E. Lacy, X. Gu, S. Kundu, Mechanical Properties and Failure Behavior of Physically Assembled Triblock Copolymer Gels with Varying Midblock Length, Journal of Polymer Science Part B: Polymer Physics 57 (15) (2019) 1014–1026. doi:10.1002/polb.24860.

[129] S. Mishra, R. M. Badani Prado, S. Kundu, Concentration-Dependent Mechanical Behavior of Physically Assembled Triblock Copolymer Gels, ACS Appl. Polym. Mater. 2 (12) (2020) 5388–5397. doi:10.1021/acsapm.0c00583.

[130] H. Kishi, Y. Kunimitsu, J. Imade, S. Oshita, Y. Morishita, M. Asada, Nano-phase structures and mechanical properties of epoxy/acryl triblock copolymer alloys, Polymer 52 (3) (2011) 760–768. doi:10.1016/j.polymer.2010.12.025.

[131] K. Yamada, H. Kishi, Control of nanostructures in epoxy/acrylic block copolymer blends by the in situ generation of functional groups, Polym J 49 (8) (2017) 617–623. doi:10.1038/pj.2017.26.

[132] M. A. Hillmyer, P. M. Lipic, D. A. Hajduk, K. Almdal, F. S. Bates, Self-Assembly and Polymerization of Epoxy Resin-Amphiphilic Block Copolymer Nanocomposites, J. Am. Chem. Soc. 119 (11) (1997) 2749–2750. doi:10.1021/ja963622m.

[133] P. M. Lipic, F. S. Bates, M. A. Hillmyer, Nanostructured Thermosets from Self-Assembled Amphiphilic Block Copolymer/Epoxy Resin Mixtures, J. Am. Chem. Soc. 120 (35) (1998) 8963–8970. doi:10.1021/ja981544s.

[134] J. D. Liu, Z. J. Thompson, H.-J. Sue, F. S. Bates, M. A. Hillmyer, M. Dettloff, G. Jacob, N. Verghese, H. Pham, Toughening of Epoxies with Block Copolymer Micelles of Wormlike Morphology, Macromolecules 43 (17) (2010) 7238–7243. doi:10.1021/ma902471g.

[135] H. E. Romeo, I. A. Zucchi, M. Rico, C. E. Hoppe, R. J. J. Williams, From Spherical Micelles to Hexagonally Packed Cylinders: The Cure Cycle Determines Nanostructures Generated in Block Copolymer/Epoxy Blends, Macromolecules 46 (12) (2013) 4854–4861. doi:10.1021/ma400778s.

[136] H. Kishi, Y. Kunimitsu, Y. Nakashima, T. Abe, J. Imade, S. Oshita, Y. Morishita, M. Asada, Control of nanostructures generated in epoxy matrices blended with PMMA-b-PnBA-b-PMMA triblock copolymers, Express Polym. Lett. 9 (1) (2015) 23–35. doi:10.3144/expresspolymlett.2015.4.

[137] H. Kishi, Y. Kunimitsu, Y. Nakashima, J. Imade, S. Oshita, Y. Morishita, M. Asada, Relationship between the mechanical properties of epoxy/PMMA-b-PnBA-b-PMMA block copolymer blends and their three-dimensional nanostructures, Express Polym. Lett. 11 (10) (2017) 765–777. doi:10.3144/expresspolymlett.2017.74.

[138] C. T. Sun, Z. H. Jin, Chapter 9 - Cohesive Zone Model, in: C. T. S. H. Jin (Ed.), Fracture Mechanics, Academic Press, Boston, 2012, pp. 227–246.

[139] M. D. Eaton, L. C. Brinson, K. R. Shull, Temperature dependent fracture behavior in model epoxy networks with nanoscale heterogeneity, Polymer 221 (2021) 123560. doi:10.1016/j.polymer.2021.123560.

[140] A. Smith, S. J. Wilkinson, W. N. Reynolds, The elastic constants of some epoxy resins, J Mater Sci 9 (4) (1974) 547–550. doi:10.1007/BF02387527.

[141] S. A. Sutton, Fatigue crack propagation in an epoxy polymer, Engineering Fracture Mechanics 6 (3) (1974) 587–595. doi:10.1016/0013-7944(74)90015-0.

[142] S. V. Kolluru, E. F. O'Neil, J. S. Popovics, S. P. Shah, Crack Propagation in Flexural Fatigue of Concrete, Journal of Engineering Mechanics 126 (9) (2000) 891–898. doi:10.1061/(ASCE)0733-9399(2000)126:9(891).

[143] M. H. Kothmann, R. Zeiler, A. Rios de Anda, A. Brückner, V. Altstädt, Fatigue crack propagation behaviour of epoxy resins modified with silica-nanoparticles, Polymer 60 (2015) 157–163. doi:10.1016/j.polymer.2015.01.036.

[144] A. Klingler, B. Wetzel, Fatigue crack propagation in triblock copolymer toughened epoxy nanocomposites, Polymer Engineering & Science 57 (6) (2017) 579–587. doi:10.1002/pen.24558.

[145] B. V. Derjaguin, V. M. Muller, Y. P. Toporov, Effect of contact deformations on the adhesion of particles, Journal of Colloid and Interface Science 53 (2) (1975) 314–326. doi:10.1016/0021-9797(75)90018-1.

[146] A. Bakker, Compatible Compliance and Stress Intensity Expressions for the Standard Three-Point Bend Specimen, Fatigue & Fracture of Engineering Materials & Structures 13 (2) (1990) 145–154. doi:10.1111/j.1460-2695.1990.tb00586.x.

[147] G. V. Guinea, J. Y. Pastor, J. Planas, M. Elices, Stress Intensity factor, compliance and CMOD for a General Three-Point-Bend Beam, International Journal of Fracture 89 (2) (1998) 103–116. doi:10.1023/A:1007498132504.

[148] S. Ritzenthaler, E. Girard-Reydet, J. P. Pascault, Influence of epoxy hardener on miscibility of blends of poly(methyl methacrylate) and epoxy networks, Polymer 41 (16) (2000) 6375–6386. doi:10.1016/S0032-3861(99)00817-4.

[149] M. T. Bashar, U. Sundararaj, P. Mertiny, Morphology and mechanical properties of nanostructured acrylic tri-block-copolymer modified epoxy, Polymer Engineering & Science 54 (5) (2014) 1047–1055. doi:10.1002/pen.23648.

[150] J. G. Williams, Applications of linear fracture mechanics, in: Failure in Polymers, Advances in Polymer Science, Springer, Berlin, Heidelberg, 1978, pp. 67–120. doi:10.1007/3-540-08829-6_2.

[151] S. R. Mousavi, S. Estaji, M. Raouf Javidi, A. Paydayesh, H. A. Khonakdar, M. Arjmand, E. Rostami, S. H. Jafari, Toughening of epoxy resin systems using core–shell rubber particles: A literature review, J Mater Sci 56 (33) (2021) 18345–18367. doi:10.1007/s10853-021-06329-8.

[152] A. Klingler, A. Bajpai, B. Wetzel, The effect of block copolymer and core-shell rubber hybrid toughening on morphology and fracture of epoxy-based fibre reinforced composites, Engineering Fracture Mechanics 203 (2018) 81–101. doi:10.1016/j.engfracmech.2018.06.044.

[153] N. Ogasawara, M. Shiratori, Application of infrared thermography to fracture mechanics, in: Thermosense XIX: An International Conference on Thermal Sensing and Imaging Diagnostic Applications, Vol. 3056, SPIE, 1997, pp. 201–213. doi:10.1117/12.271644.

[154] H. Zhang, A. K. Scholz, Y. Merckel, M. Brieu, D. Berghezan, E. J. Kramer, C. Creton, Strain induced nanocavitation and crystallization in natural rubber probed by real time small and wide angle X-ray scattering, J. Polym. Sci. Part B: Polym. Phys. 51 (15) (2013) 1125–1138. doi:10.1002/polb.23313.

[155] J. B. Le Cam, Energy storage due to strain-induced crystallization in natural rubber: The physical origin of the mechanical hysteresis, Polymer 127 (2017) 166–173. doi:10.1016/j.polymer.2017.08.059.

[156] J. Chen, Y. Liu, Fatigue modeling using neural networks: A comprehensive review, Fatigue & Fracture of Engineering Materials & Structures 45 (4) (2022) 945–979. doi:10.1111/ffe.13640.

[157] W. Muhammad, A. P. Brahme, O. Ibragimova, J. Kang, K. Inal, A machine learning framework to predict local strain distribution and the evolution of plastic anisotropy & fracture in additively manufactured alloys, International Journal of Plasticity 136 (2021) 102867. doi:10.1016/j.ijplas.2020.102867.

[158] F. Zhou, Z. Guo, W. Wang, X. Lei, B. Zhang, H. Zhang, Q. Zhang, Preparation of self-healing, recyclable epoxy resins and low-electrical resistance composites based on double-disulfide bond exchange, Composites Science and Technology 167 (2018) 79–85. doi:10.1016/j.compscitech.2018.07.041.

[159] H. Si, L. Zhou, Y. Wu, L. Song, M. Kang, X. Zhao, M. Chen, Rapidly reprocessable, degradable epoxy vitrimer and recyclable carbon fiber reinforced thermoset composites relied on high contents of exchangeable aromatic disulfide crosslinks, Composites Part B: Engineering 199 (2020) 108278. doi:10.1016/j.compositesb.2020.108278.

[160] H.-Y. Tsai, Y. Nakamura, T. Fujita, M. Naito, Strengthening epoxy adhesives at elevated temperatures based on dynamic disulfide bonds, Materials Advances 1 (9) (2020) 3182–3188. doi:10.1039/D0MA00714E.

[161] J. H. Flynn, L. A. Wall, A quick, direct method for the determination of activation energy from thermogravimetric data, Journal of Polymer Science Part B: Polymer Letters 4 (5) (1966) 323–328. doi:10.1002/pol.1966.110040504.

Chapter 8

Appendices

A Temperature-Dependent Viscoelastic Energy Dissipation and Fatigue Crack Growth in Filled Silicone Elastomers

A.1 Material Properties

A.1.1 Thermogravimetric Analysis

Using thermogravimetric analysis (TGA), the degradation kinetics can be obtained by using the Flynn & Walls method[161]. The temperature-dependent mass data for a silicone rubber sample (SR-F37-C0.8) and a natural rubber sample (NR-F30) in air and in nitrogen are shown in Figure 8.1. By defining a certain point of weight loss during the constant heating rate TGA experiment, a relation between the heating rate and temperature of the point of weight loss exists and the degradation activation energy E_a can be calculated:

$$E_a = \left(-\frac{R}{b}\right)\frac{d\ln\beta}{d(1/T)} \tag{8.1}$$

Here, R is the gas constant (8.314 J/mol K), b is a fitting constant, β is the heating rate (°C·min^{-1}), T is the temperature where the point of weight loss happens (K). According to Equation 8.1, if there are more than three measurements using different heating rates on the material, a linear relation between $\ln\beta$ and $1/T$ can be found to calculate the activation energy E_a. Figure 8.2 (a) and (b) show the linear relation between $\ln\beta$ and $1/T$ at a weight loss of 15%.

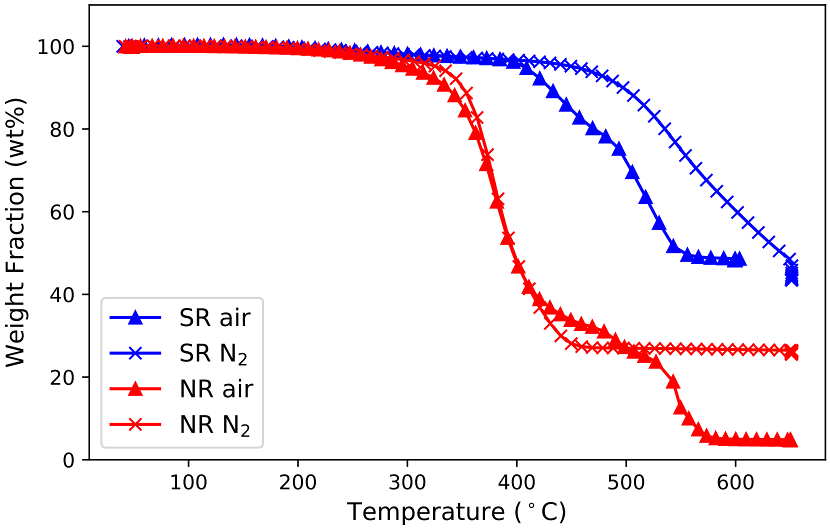

Figure 8.1: TGA results for the silicone rubber (SR-F37-C0.8) and natural rubber (NR-F30) samples at heating rate of $10\,^{\circ}\mathrm{C{\cdot}min^{-1}}$.

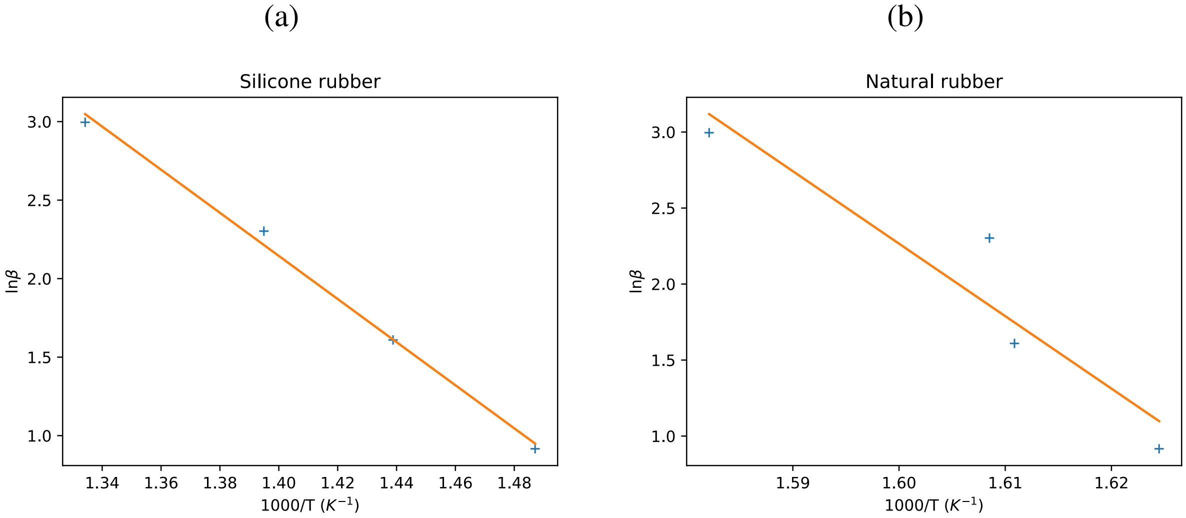
(a)

(b)

Figure 8.2: $\ln\beta$ as a function of $^1/_T$ for SR-F37-C0.8 (a) and NR-F30 (b) at a weight loss of 15%.

Table 8.1: VFT parameters for the SR and NR samples, obtained from the DMA experiments.

	B (K)	T_∞ (°C)
NR	2600	-122
SR	2250	-170

A.1.2 Dynamic Mechanical Analysis

The dynamic mechanical analysis (DMA) data for both elastomer samples for which temperature-dependent data were obtained are shown in Figure 8.3. The complex modulus E^* is used to express both the storage and loss modulus through the equation $E^* = E' + iE''$. The loss tangent, $\tan\delta$ is given as $\tan\delta = E''/E'$. All properties are plotted as a function of the reduced frequency, fa_T, where f is the frequency of the experiment and a_T is a temperature-dependent shift factor obtained by shifting data horizontally along the frequency axis. Both elastomer samples provide clear master curves for $|E^*|$. We define a rheological glass transition temperature, T_g, as the temperature at which $\tan\delta$ is maximized for a frequency of 1 Hz. We obtain $T_g = -110\,°\mathrm{C}$ for the SR sample and $T_g = -50\,°\mathrm{C}$ for the NR sample. These temperatures are used as the reference temperature for which a_T = 1. The values of shift factors are listed in Table 8.2and 8.3.

For each temperature, the shift factors and their corresponding temperatures can be fit using the Vogel-Fulcher-Tammann (VFT) relation (Figure 8.3 (c), (f)):

$$\ln(a_T) = -\frac{B}{T_{ref} - T_\infty} + \frac{B}{T - T_\infty} \tag{8.2}$$

Values of B and T_∞ for each of the polymers are listed in Table 8.1.

Table 8.2: Shift factors for DMA time-temperature superposition of SR.

Temperatures (°C)	-120	-115	-110	-105	-100	-95	-90
a_T	500	18	1	0.04	2.5×10^{-3}	2×10^{-4}	3×10^{-5}

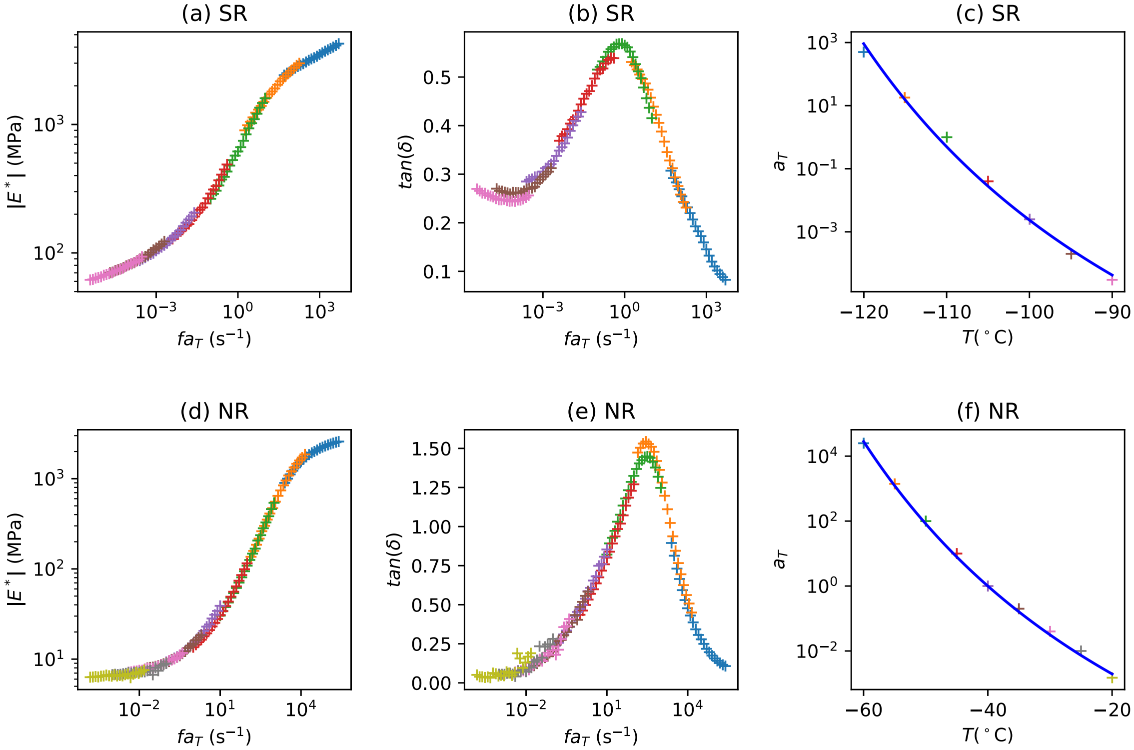

Figure 8.3: Dynamic mechanical analysis data for silicone rubber (SR-F37-C0.8, a-c) and natural rubber (NR-F30, d-f). Solid lines in (c) and (f) represent fits to the VFT equation (Equation 8.2), using the parameters listed in Table 8.1.

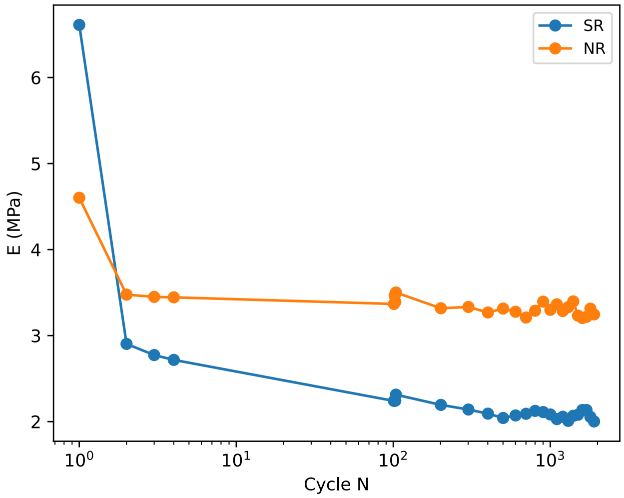

Figure 8.4: Evolution of the modulus of an unnotched silicone rubber SR-F37-C0.8 (SR) and natural rubber NR-F30(NR) sample at 40°C for a strain amplitude, ε, of 0.5.

Table 8.3: Shift factors for DMA time-temperature superposition of NR.

Temperatures (°C)	-60	-55	-50	-45	-40	-35	-30	-25	-20
a_T	2.5×10^4	1300	100	10	1	0.2	0.04	0.01	2×10^{-3}

A.2 Evolution of Modulus During the 2000 Pre-cycles of Unnotched Samples

The dependence of the modulus on the cycle number during the pre-cycle step is shown in Figure 8.4, which shows the change of modulus during the first 2000 cycles for the deformation of an unnotched sample at a strain amplitude of 0.5. Note that the modulus reaches a stable value after several hundred cycles.

A.3 Fatigue Crack Surface

More figures of the crack surface is shown here. In all the samples, the crack propagation direction is from right to left. Only one set of NR surface morphology is shown as the rest of them have similar appearance, and no obvious change is observed when the temperature changes.

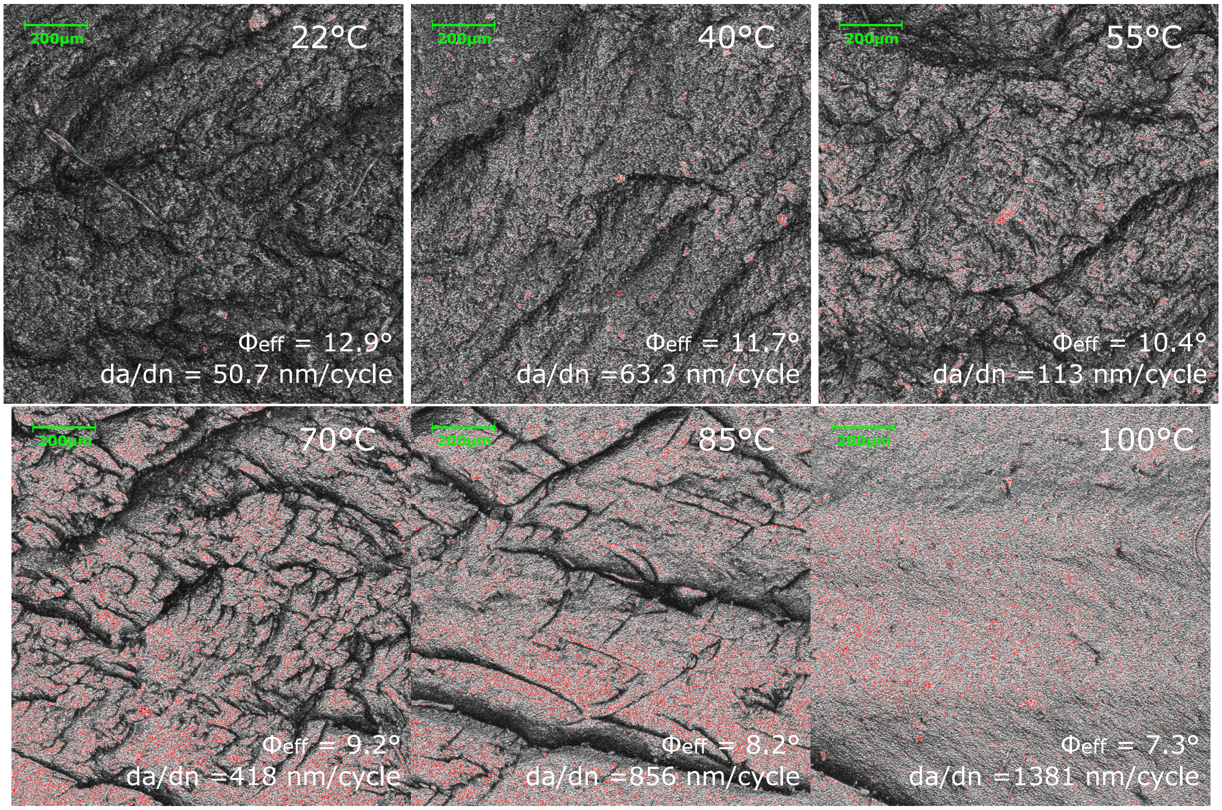

Figure 8.5: Fatigue crack surfaces for SR at strain $\varepsilon = 0.45$. The fatigue experiments are conducted at 22 °C, 40 °C, 55 °C, 70 °C, 85 °C and 100 °C, as indicated. The crack propagation direction is from right to left.

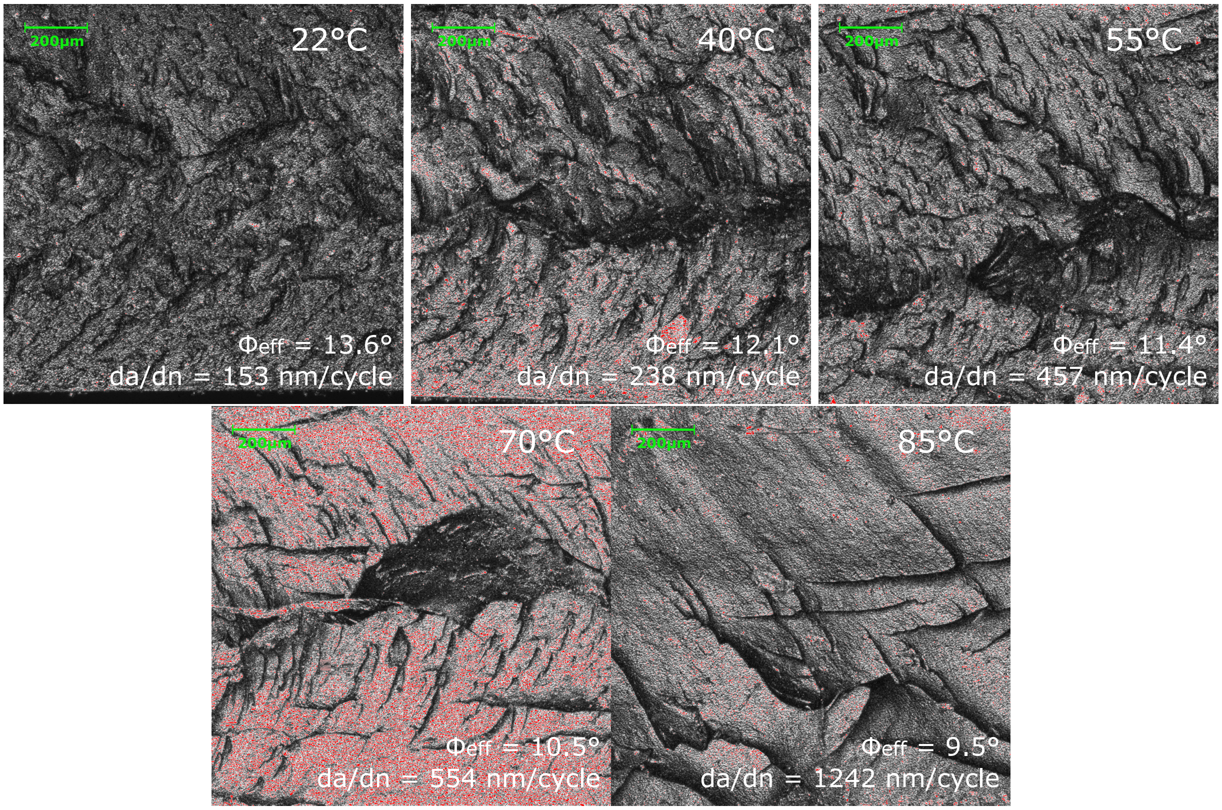

Figure 8.6: Fatigue crack surfaces for SR at strain $\varepsilon = 0.6$. The fatigue experiments are conducted at 22 °C, 40 °C, 55 °C, 70 °C and 85 °C, as indicated.

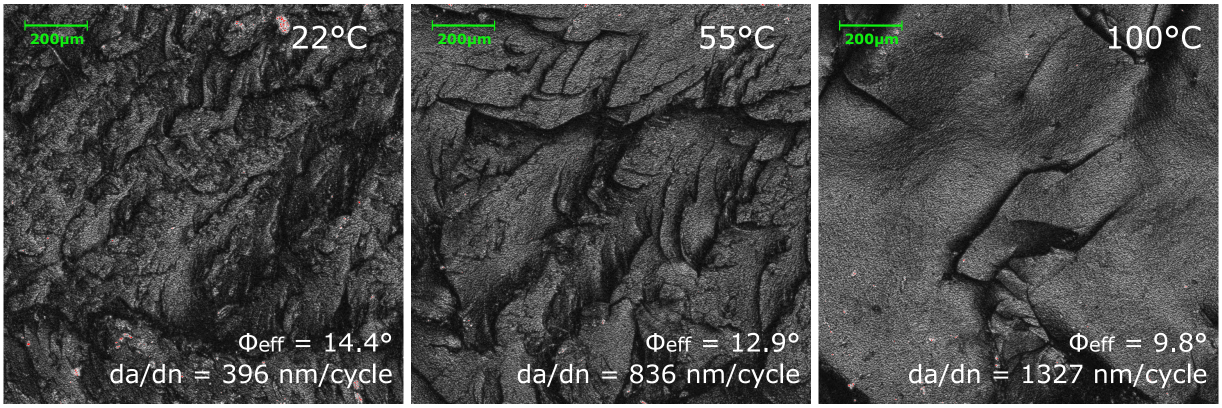

Figure 8.7: Fatigue crack surfaces for SR at strain $\varepsilon = 0.8$. The fatigue experiments are conducted at 22 °C, 55 °C and 100 °C, as indicated. The crack propagation direction is from right to left.

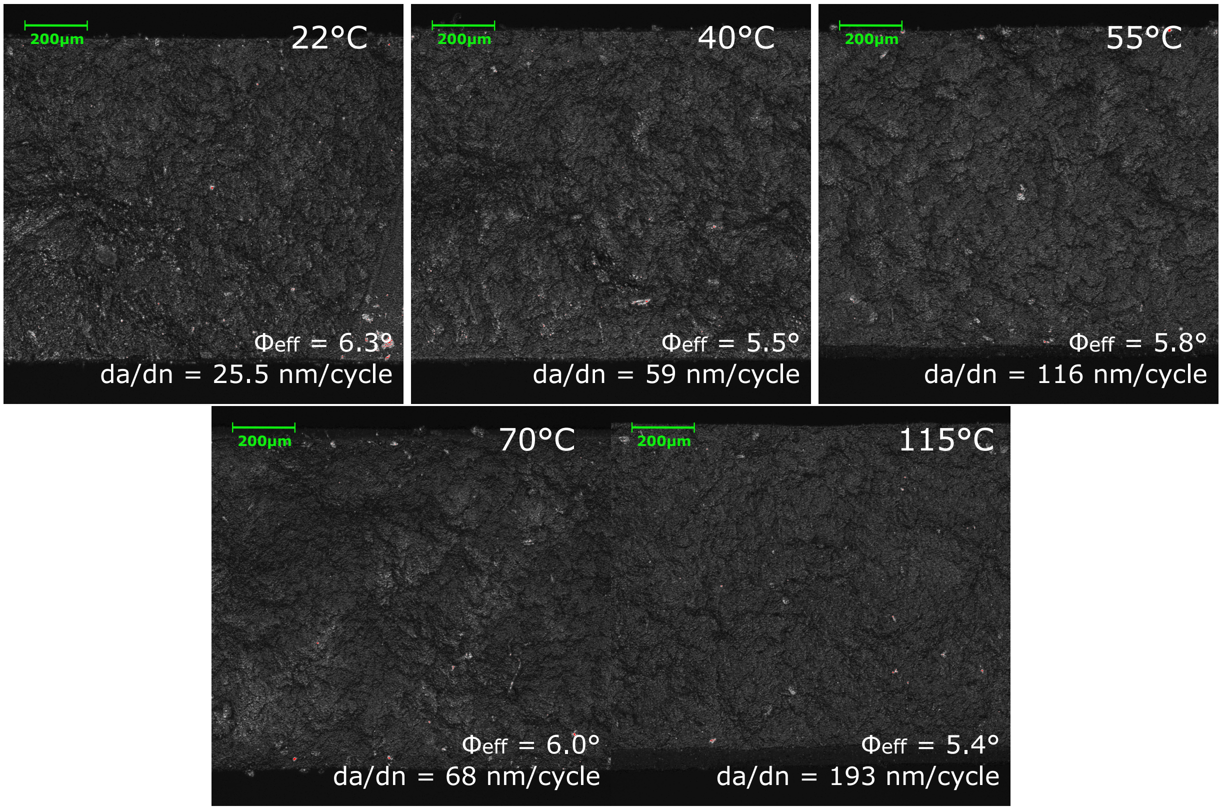

Figure 8.8: Fatigue crack surfaces for NR at strain $\varepsilon = 0.6$. The fatigue experiments are conducted under 22 °C, 40 °C, 55 °C, 70 °C and 115 °C, as indicated. The crack propagation direction is from right to left.

B Interpretation of Bulk and Adhesive Fatigue Damage in Pressure-Sensitive Adhesives

B.1 Multi-round Repeated Detachment Behavior

In order to study the resilience of interfacial strength over time, a series of repeated detachment tests were conducted using the same repeated probe test protocol. In each cycle, ten probe-tack tests were performed at the same location on the surface. With the indenter strain rate maintained at 0.5 s^{-1} , the adhesives were allowed a relaxation period of 30 minutes. In the final two cycles,

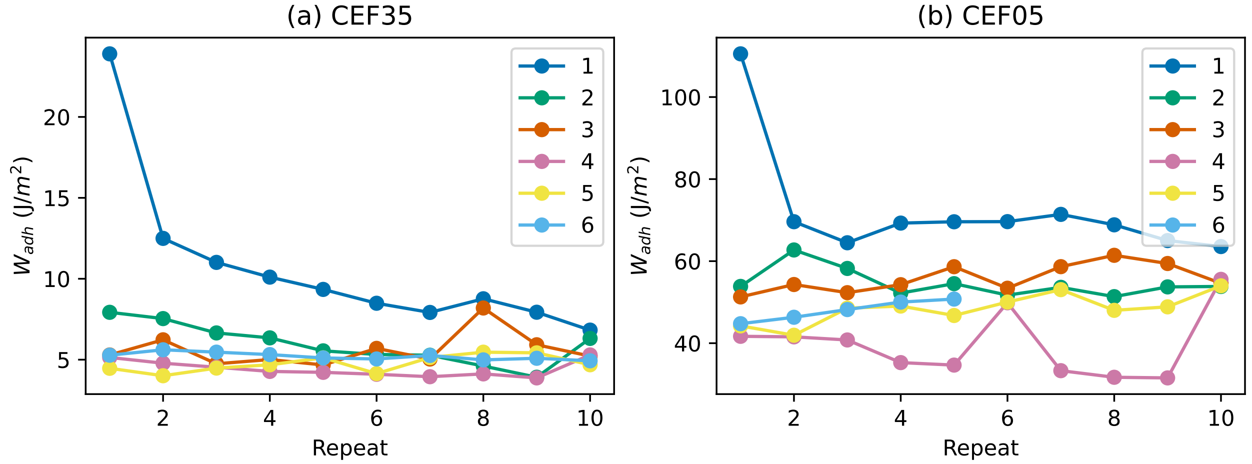

Figure 8.9: The change of $W_{adh}$of CEF35 (a) and CEF05 (b) during a multi-round repeated probe tack test.

the samples were left to relax overnight to observe any potential long-term adhesion recovery. The corresponding change of W_{adh} curves are depicted in Figure 8.9. It was found that the adhesive strength progressively decreased until reaching a stable plateau. Notably, no recovery was observed even over the extended period of relaxation, indicating a persistent reduction in adhesion strength.

B.2 Multi-round Incremental Oscillation Behavior

To probe the fatigue response encompassing both the bulk and interfacial contributions of the adhesives, we executed a series of incremental oscillation tests. These tests were structured in multiple rounds, with each test round consisted of a triangular waveform designed to systematically increase the strain level. After each round, the samples were given a 30-minute rest for the initial three rounds, followed by an overnight rest to examine long-term adhesive strength recovery in subsequent rounds. Figure 8.10 and 8.11 display the multi-round fatigue data for CEF35 and CEF05 respectively. The work of adhesion, W_{adh}, across the multiple rounds was subdivided into the dissipative energy component, Γ, and the stored energy, $\mathcal{G}$. Similar to our discussion in the main text, the observed maximum, $\mathcal{G}_c$, signifies the critical value for the decrease of contact area,

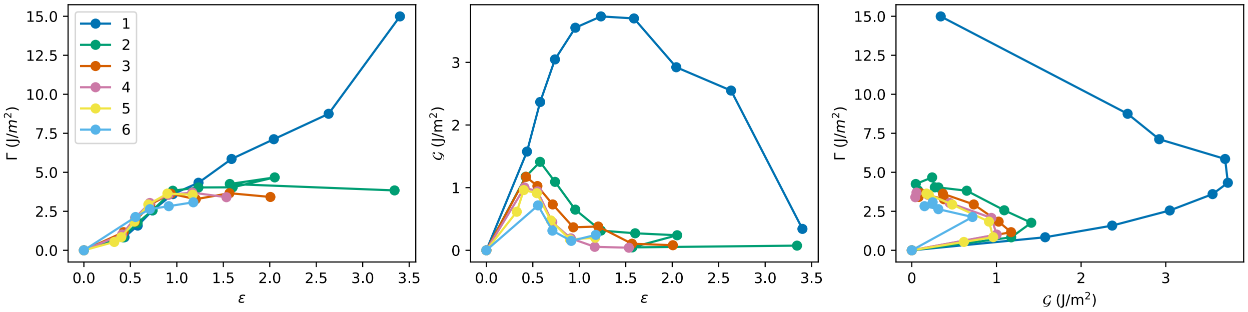

Figure 8.10: The relationship between Γ, $\mathscr{G}$ and ε for CEF35 over six rounds of triangular wave tests. (a) The bulk energy dissipation Γ as a function of strain over 6 rounds of test. (b) The stored energy $\mathscr{G}$ as a function of strain. (c) The comparison of multi-round Γ and $\mathscr{G}$.

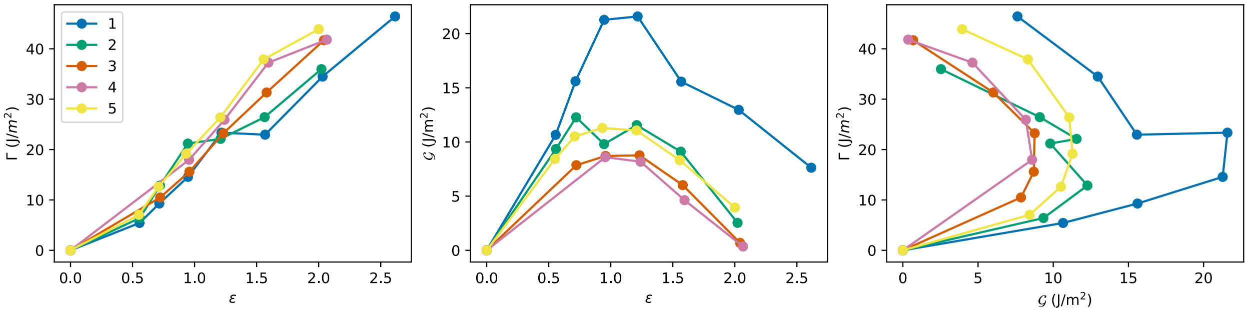

Figure 8.11: The relationship between Γ, $\mathscr{G}$ and ε for CEF05 over five rounds of triangular wave tests.

marking the initiation point of interfacial failure. The data of CEF35 shown in Figure 8.10 (a) reveals constant softening effect across multiple rounds. The maximum Γ stabilized at approximately 5 J/m^2, which consists with the value of W_{adh} in the last two rounds of test in Figure 8.9 (a). This permanent decrease of Γ might indicate irreversible bulk damage, resulting in a reduced capacity for bulk energy dissipation in later rounds. The values of $\mathscr{G}_c$ also decreased to around 1 J/m^2, suggesting an permanent interfacial damage induced by fatigue. For CEF05 samples, less bulk damage is observed, as seen in Figure 8.11 (a) , where the increment of Γ remains unaffected by multiple rounds. The $\mathscr{G}$ values over multiple rounds decreased and showed small amount of recovery between round 4 and 5 as shown in Figure 8.11 (b). Both adhesive samples demonstrate that the accumulation of adhesive fatigue is irreversible.